Thorsten Schumm

TECHNISCHE UNIVERSITÄT WIEN
Vienna University of Technology

Diplomarbeit

Towards a 3D optical lattice potential inside an optical high-finesse cavity

ausgeführt am
Atominstitut
der Technischen Universität Wien

unter der Anleitung von

Univ.Prof. Dipl.-Phys. Dr.rer.nat. Thorsten Schumm

durch

Lorenz Hruby
Rothboeckstr. 8
5282 Ranshofen am Inn

October 25, 2013

Lorenz Hruby

Abstract

In recent years, our cavity coupled ultra-cold ^{87}Rb cloud experiment was used to investigate the Dicke phase transition in a 2D checkerboard lattice. In a next step, an optical lattice potential in the third dimension is being added, which increases the requirements on the stability of the probe laser and creates the need for a stabilization tool of the lattice laser.
A new type of carbon-fiber based transfer cavity with active temperature stabilization, high mechanical stability and low thermal expansion used for the Pound-Drever-Hall laser lock of the probe laser is presented.
By using the low coefficient of thermal expansion of unidirectional carbon fiber tubes and by suppressing the thermal expansion of aluminum and glues used in the cavity assembly along the optical axis of the cavity, a very low coefficient of thermal expansion of $\alpha_T = 1.7 \times 10^{-6}$ K^{-1} of the assembled cavity was reached.
The remaining coefficient of thermal expansion was used to tune the cavity resonance by heating and convection cooling. Using a Toptica DLpro 780 diode laser, the cavity was locked to a wavemeter as an absolute frequency reference with a very slow feedback loop to the cavity heater reacting on a timescale of minutes. As a result of this very slow reference lock, the transfer cavity locked probe laser showed stable single mode operation over the course of several weeks of operation. A standard deviation of 1.8 MHz from the set point wavelength was observed in a 16 h measurement, while frequency deviations stayed below 10 MHz at all times.
The transfer cavity with a Finesse of 2×10^3 and a linewidth of 4×10^2 kHz was used to narrow down the relative linewidth of the probe laser to a few tens of kilohertz.
The design presented was also used in a second cavity to stabilize the lattice laser and to consequently reduce heating of the atoms.

Kurzfassung

In den letzten Jahren wurden der Dicke-Phasenübergang in einem 2D Schachbrett-Gitterpotential in unserem "Cavity"-gekoppelten ultrakalten ^{87}Rb-Gasexperiment untersucht. In einem weiteren Schritt wird nun ein optisches Gitterpotential in der dritten Dimension hinzugefügt, welches die Anforderungen an die Stabilität des "Probe"-Lasers erhöht und die Frage nach einer Möglichkeit der Stabilisierung des Gitterlasers aufwirft.
Ein neuer Typ einer karbonfaserbasierten "Trasfer-Cavity" mit aktiver Temperaturstabilisierung, einer hohen mechanischen Stabilität und einer geringen Wärmeausdehnung wird vorgestellt.
Durch Ausnutzung des geringen Wärmeausdehnungskoeffizienten von unidirektional aufgebauten Karbonfaserrohren und der Unterdrückung der Wärmeausdehnung des verbauten Aluminiums und Klebstoffs entlang der optischen Achse der "Cavity" wurde ein sehr geringer Wärmeausdehnungskoeffizient der zusammengebauten "Cavity" von $\alpha_T = 1.7 \times 10^{-6}$ K^{-1} erreicht.
Der verbliebene Wärmeausdehnungskoeffizient wurde zum Durchstimmen der "Cavity"-Resonanz durch Erhitzen und Konvektionskühlen genutzt. Unter Verwendung eines Toptica DLpro 780 Diodenlasers wurde die "Cavity" an ein Wavemeter als absolute Frequenzreferenz gekoppelt, wobei die sehr träge Rückkopplung auf das "Cavity"-Heizelement auf einer Zeitskala von Minuten reagiert. Als Resultat dieser sehr trägen Rückkopplung lief der Transfer-"Cavity" gekoppelte "Probe"-Laser stabil einmodigen während mehrwöchigen Betriebs. In einer 16 h Langzeitmessung betrug die Standardabweichung von der eingestellten Laserfrequenz 1.8 MHz, wobei die Frequenzabweichungen stets kleiner als 10 MHz blieben.
Die Transfer-"Cavity" mit einer Finesse von 2×10^3 und einer Linienbreite von 4×10^2 kHz wurde zur Reduktion der relativen Linienbreite des "Probe"-Lasers auf einige Zehn Kilohertz verwendet.
Das vorgestellte Design wurde auch in einer zweiten "Cavity" zur Stabilisierung des Gitterlasers sowie zur einhergehenden Reduktion der Heizrate der Atome genutzt.

CONTENTS

1. Introduction 1

2. Cavity design 3
2.1 Design of the cavity 4
2.1.1 Cavity stability condition 4
2.1.2 Mechanical assembly of the cavity 5
2.1.3 Characteristic cavity parameters 9
2.1.4 Higher order transverse cavity modes 14
2.1.5 Cavity incoupling and mode matching 15
2.2 Thermal properties of the cavity 18
2.2.1 Materials and design 18
2.2.2 Sensitivity to length and temperature change 20
2.3 Mechanical properties of the cavity 22

3. Cavity lock characteristics 24
3.1 Laser fluctuations and noise 24
3.1.1 Amplitude/intensity fluctuations 24
3.1.2 Polarization fluctuations 26
3.1.3 Phase/frequency fluctuations 27
3.2 Temperature lock 29
3.2.1 Heating wire 29
3.2.2 Cavity temperature controller (CTC) 31
3.2.3 CTC electronics 33
3.2.4 Long term frequency stability 37
3.2.5 Discussion 37
3.3 Pound-Drever-Hall lock 38
3.4 Measurement setup 41
3.4.1 Optical setup 42
3.4.2 Electronic setup 44
3.5 Laser lock characterization and laser linewidth 45
3.5.1 PDH error signal 48
3.5.2 Cavity transmission signal 48

3.5.3 Spectral noise density 52
3.5.4 Laser beat note 57
3.5.5 Discussion 59

4. Implementation of the cavity in the current experiment setup . . . 61

5. Conclusion and outlook 63

Appendices 66

A. General theory on optical cavities 67
A.1 The light field in the cavity 67
A.2 Maximum power and Finesse 71
A.3 Transmitted, reflected and cavity light field 71
A.4 Axial cavity mode frequencies 74
A.5 Cavity ring-down time 75

B. Wave analysis of beams and cavities 78
B.1 Gaussian beams 78
B.2 Hermite - Gaussian beams 83
B.3 Laguerre - Gaussian beams 84

C. Pound-Drever-Hall laser lock 85

1. INTRODUCTION

Nearly two decades ago, the breakthrough in the realization of a Bose-Einstein condensate [1, 2] paved the way towards a new kind of tool to investigate the fundamental laws of quantum mechanics, BEC-based quantum simulators. In our experiment, a cigar shaped cloud of ultra-cold ^{87}Rb atoms is overlapped with the light field of an optical high Finesse cavity to increase the light-matter interaction [3]. In recent experiments [4, 5] the cloud was pumped by a laser transverse to the optical axis of the cavity. The laser was far detuned from atomic resonance but close to a cavity resonance. The cloud scatters photons into the cavity and above a critical pump power, the atoms self-organize in the checkerboard-shaped optical potential created by the pump beam and the cavity light field. Via long-range atom-atom interactions, the atoms self-organize in tubes on either the even or odd sites of the checkerboard pattern, so that the competition between kinetic and potential energy leads to a Dicke phase transition [6, 7].

Now we extend this work by bringing yet another energy scale into play, the on-site interaction energy. The tubes of self-organized atoms are cut into single lattice sites, where on-site interaction is important. While the checkerboard lattice was based on a 2D optical potential, the new optical lattice introduces a potential in the third dimension. Stable lasers of narrow linewidth play a crucial role in these experiments as a tool to prepare, manipulate and probe the atomic cloud. The introduction of a lattice potential in our setup increases the requirements on the stability of both the probe laser and the laser used to generate the lattice potential. Lasers can be narrowed down and stabilized with respect to each other with the help of high finesse optical cavities. Until now cavities in our experiment were limited by thermal drifts which lead to frequent un-locking of the probe laser during measurements. Newly designed cavities used to reduce the sensitivity to these thermal drifts, to narrow down the laser which creates the lattice potential and accordingly, to reduce heating on the atoms, were needed as a crucial tool to successfully realize a 3D optical lattice potential in the system.

We report on the development, characterization and implementation of a

new temperature tuned transfer cavity and the corresponding electronic regulation into our quantum simulator setup. The probe laser at a wavelength of $780 - 785$ nm and a second laser at a wavelength of 830 nm, which is far detuned from atomic resonance, are both locked to the transfer cavity. The transfer cavity is locked to a wavemeter as a frequency reference via the transmission of the probe laser, while the high Finesse science cavity is locked to the 830 nm laser. By introducing this locking chain, the probe laser and the 830 nm laser are both stabilized to an absolute frequency and with respect to each other and can be both resonant with the science cavity at the same time. The transfer cavity therefore transfers the stability of one laser to the other.

The new transfer cavity is designed to combine high mechanical and thermal stability by using a carbon fiber tube as the mirror spacer. The cavity mirrors are mounted in such a way as to minimize thermal expansion of the cavity along the optical axis. The remaining thermal expansion is used to tune the resonance frequency of the cavity by heating and convectional cooling the system with the help of temperature control electronics, while previous generations of transfer cavities featured a piezo-electric tube for this purpose, which is prone to electric noise. The design developed for the transfer cavity was re-used in a second cavity to stabilize the lattice laser.

This work is split into three sections. Chapter 2 reports on the mechanical design of the new transfer cavity and explains the specific materials used as well as the detailed assembly of the system. It presents the characteristic properties of the cavity with a particular focus on the thermal and mechanical stability. In chapter 3, the laser lock is explained and characterized. Various noise present in the system is investigated and frequency noise of the locked laser is discussed in detail. Chapter 4 reports on the implementation of the new transfer cavity in the existing experiment and chapter 5 finally concludes.

A general theoretical description on optical cavities, laser beams and the Pound-Drever-Hall laser lock [8] is appended, where most of the theory used is derived and summarized in a self-consistent manner. The reader new to the field of optical cavities may find the appendix helpful to quickly gain insight into the basic underlying theory needed and to understand and link the equations used.

2. CAVITY DESIGN

The frequency stability of a cavity based laser lock is mainly determined by two factors, the regulation quality of the laser lock and the mechanical and thermal stability of the optical cavity. In this chapter we want to introduce a new design approach for the third generation transfer cavity used in our experiment with high mechanical stability and low thermal expansion. While the first generation transfer cavity was built from aluminum, the second generation was based on a carbon fiber (CFK) tube as suggested in [9]. The third generation transfer cavity will follow a similar approach which is also based on a CFK tube.

The excellent mechanical and thermal properties make CFK a good candidate for a cavity spacer material, which was successfully tested in the second generation transfer cavity. In the third generation, we want to improve the design to minimize the thermal expansion and maximize the mechanical stability of the cavity. While both the first and second generation transfer cavity featured a piezo electric tube to stabilize the length and accordingly, the resonance frequency of the cavity, the third generation is actively temperature controlled to do so. The mechanical designs and many physical properties of the third generation transfer cavity resemble those of the first and second generation, as they were all designed as iterative upgrades with respect to each other, placed in the same optical setup in the experiment.

In the following, we first want to report on the general design and assembly of the new transfer cavity. A more detailed description of the materials used and the thermal and mechanical properties is presented in the second half of this chapter. Before focusing on these details, we want to present a compact theoretical framework which is used to describe the core properties of the optical cavities used. We will calculate the theoretical properties of the third generation transfer cavity and compare them with measurements. Experimental results of the first and second generation cavities are also shown for comparison. The measured properties of the three cavities are expected to be approximately comparable, as they have roughly the same length and feature mirrors coated in the same batch, although of different radii of curvature.

Throughout this work, the first generation transfer cavity will be labeled as C_1, the second generation as C_2 and the third generation as C_3. All three generations of transfer cavities were built of two identical mirrors. We assume them to be lossless, the theory presented in this chapter is adapted to these specifics. A more general and more detailed review on the theory of cavities and light fields in resonators is given in appendix A and B.

2.1 Design of the cavity

"[In a general sense, an optical cavity] is a group of mirrors aligned in such a way that the beam of light is reflected in a closed path, such that after one round trip it interferes perfectly with the incident wave" [10]. In the simplest case a cavity consist of two mirrors facing each other, which are aligned on an optical axis. The incident light beam gets exactly retro-reflected and bounces back and forth between the mirrors. This geometry is called linear cavity. All cavities used in this work are of this simplest type, therefore other designs will be neglected, for more information see e.g. [10, 9].

2.1.1 Cavity stability condition

Depending on the geometry and position of the cavity mirrors, one distinguishes between stable and unstable optical cavities, where in this context stability refers to the capability of the cavity to successfully trap light. Before designing a (stable) optical cavity, one should check the so-called cavity stability condition. An overview on the theoretical description of this property is given in [11] and the cavity stability condition

$$0 \leq g_1 g_2 \leq 1 \tag{2.1}$$

for stable cavities is derived, where $g_{1/2}$ are the so called mirror parameters [10] given by

$$g_{1/2} = 1 - \frac{L}{R^c_{1/2}} \tag{2.2}$$

where $R^c_{1/2}$ is the radius of curvature of mirror 1/2, respectively. The first and second generation cavities feature mirrors of $R^c_1 = R^c_2 = 250$ mm, while the third generation transfer cavity features mirrors of curvature $R^c_1 = R^c_2 = 500$ mm. A graphical analysis of the stability of all three transfer cavities is shown in figure 2.1. All three cavities are stable cavities.

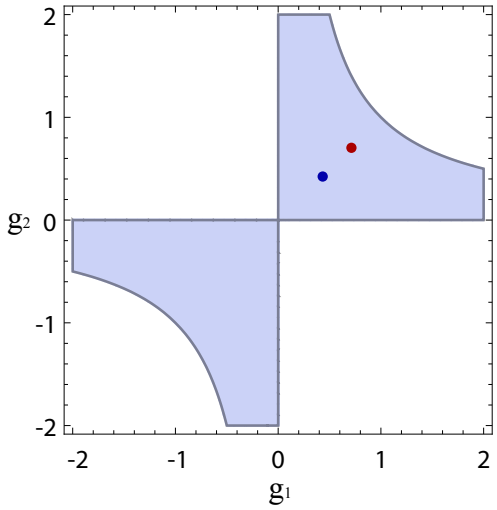

Fig. 2.1: The cavity stability plot is shown. The blue dot represents the first and second generation transfer cavities, while the red dot represents the third generation. All three cavities are positioned well in the stable region which is given by the shaded area.

2.1.2 Mechanical assembly of the cavity

The mechanical design approach taken is based on former versions of transfer cavities used in the experiment. The new third generation transfer cavity should replace the second generation variant with as little adjustments as possible on the laser table, hence the physical dimensions were largely predefined. A CAD-rendering of the third generation transfer cavity is shown in figure 2.3.

Mirrors: The mirrors used were high reflectivity coated concave spherical mirrors with a focal length of $f = -R^c/2 = -250$ mm, see table 2.1. They were positioned 144.7 mm apart from each other, the result is a crossover between a confocal and near-planar stable cavity. For an overview on the different types of stable cavities see e.g. [9].

Radius $R^c_{1/2}$	500 mm
Diameter	12.7 mm
Intensity reflectivity	99.88 %
Reflection coating	780 nm (0°)

Tab. 2.1: Cavity mirrors: Laser Optic L-05962, Batch 22040p1

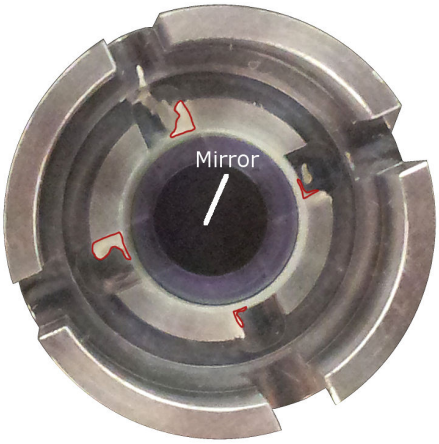

Fig. 2.2: Assembly of the mirror to the mirror mount, the position and design of the glue is shown in red.

Mechanical design: The cavity is built from a CFK spacer tube which holds the mirrors at a fixed distance with respect to each other. Since it is difficult to manufacture complex physical shapes from CFK, we chose to build the mirror mounts from aluminum. A mirror mount with the mirror glued in is shown in figure 2.2. The mounts were subsequently glued to the CFK spacer tube. The design was made such that the glue and the aluminum mirror mounts do not introduce thermal expansion issues, see section 2.2.
The CFK-tube is wrapped in brass shells, which add weight and feature good thermal conductivity. The shells are screwed together with feather washers to avoid mechanical stress which could lead to enhanced transverse beam modes. A heating wire is wrapped around large parts of the cavity to ensure homogenous heating. The assembled model of the cavity on a cavity mount is shown in figure 2.4.

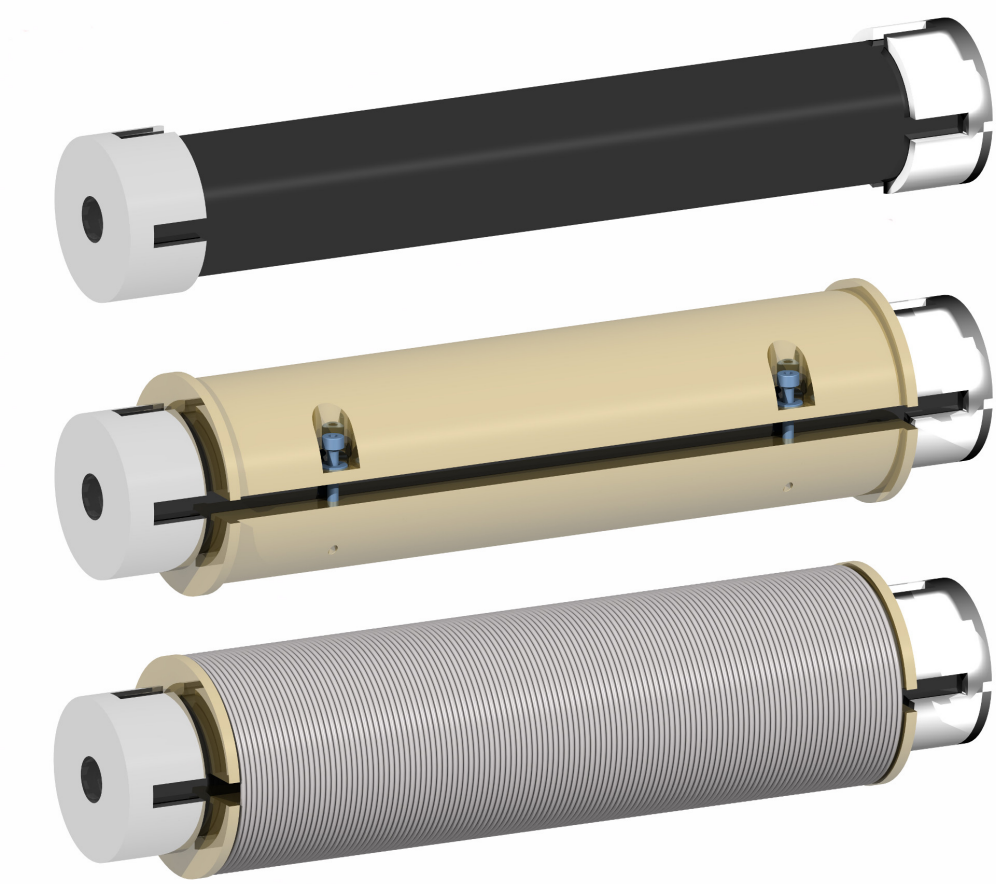

Fig. 2.3: CAD-rendering of the third generation transfer cavity (top), with the brass shells added (middle) and with the heating wire wrapped around the brass shells (bottom) is shown. The shells are screwed together with M2 screws and feather washers to avoid mechanical stress.

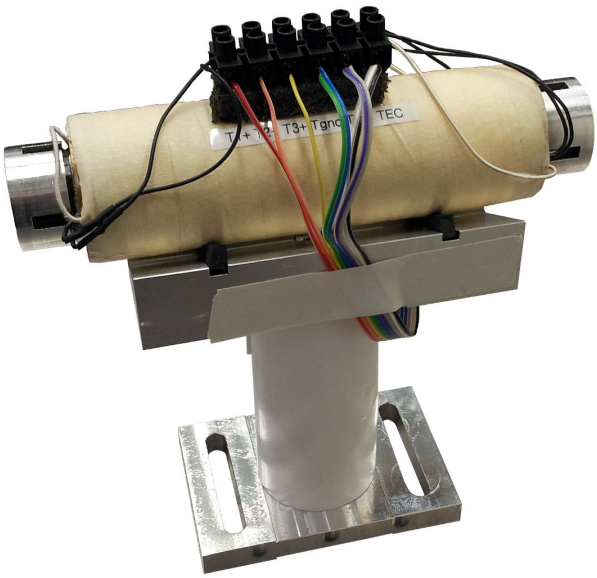

Fig. 2.4: The assembled cavity including the mount is shown. The heating wire around the cavity is wrapped in paper tape for reasons of mechanical protection, the cavity is placed on a V-shaped aluminum mount with Sorbothane shock absorbers in between, the mount rests on a Teflon post. The electric components are first connected to a luster terminal on top of the cavity and in the following, to a Sub-D9 plug on the backside of the mount (not shown).

2.1.3 Characteristic cavity parameters

If and only if the wavelength of the incident beam is an integer multiple of twice the optical length of the cavity, constructive interference inside the cavity will occur, in all other cases the beam will be damped by destructive interference. Accordingly, if we shine a laser with power P_{in} onto the cavity, the power P_t transmitted through and the power P_r reflected by the cavity will show a periodic behavior

$$P_t = \frac{1}{\left(1 + (2F/\pi)^2 \sin^2(\pi \frac{\widetilde{\nu}}{\Delta\nu_{ax}})\right)} P_{in} \tag{2.3}$$

$$P_r = \frac{(2F/\pi)^2 \sin^2(\pi \frac{\widetilde{\nu}}{\Delta\nu_{ax}})}{\left(1 + (2F/\pi)^2 \sin^2(\pi \frac{\widetilde{\nu}}{\Delta\nu_{ax}})\right)} P_{in} \tag{2.4}$$

where F is the Finesse of the cavity, which we will describe in more detail later, and $\widetilde{\nu}$ is the frequency of the laser relative to a cavity resonance. We will write most formulas in terms of $\widetilde{\nu} = \nu - \nu_c$ for readability. The periodicity results from constructive interference of the light field inside the cavity and it is a phase dependent quantity, see appendix A. The period of (2.3) and (2.4) is the so called **free spectral range** (FSR) and given by

$$\Delta\nu_{ax} = \frac{c}{2L} = 1036 \text{ MHz } (C_3) \tag{2.5}$$

where $c = c_0/n$ is the speed of light in air (index of refraction of air at room temperature $n \approx 1.00029$) and L is the length of the cavity. The length of the third generation transfer cavity is derived from the length of the second generation transfer cavity of $L = 144.7$ mm. The length of the first generation transfer cavity is also about 150 mm. We can measure the FSR by applying sidebands of known frequencies to the laser and scanning the laser over at least two cavity resonances. The cavity transmission will be peaked at resonance and also at the sideband frequencies, where the relative height of the transmission peaks is given by the beam power in the carrier and in the sidebands. The spacing between two carrier peaks corresponds to the FSR. The FSR measurement of C_1 is exemplary shown in figure 2.5. From a calibration of the scanning time to the known laser sideband frequencies, we obtain the FSR

$$\begin{aligned} C_1 &: \ \Delta\nu_{ax} = 960(2)\text{MHz} \\ C_2 &: \ \Delta\nu_{ax} = 998(1)\text{MHz} \\ C_3 &: \ \Delta\nu_{ax} = 1057(7)\text{MHz} \end{aligned} \tag{2.6}$$

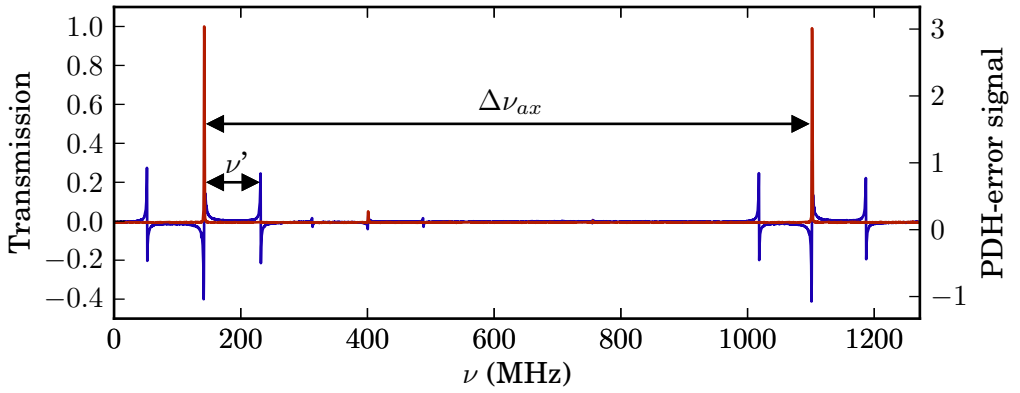

Fig. 2.5: The power transmitted through C_1 is shown in red. The blue signal corresponds to the PDH-error signal which will be discussed in section 3.3. The sidebands ν' of the laser in the transmission signal are quite small, we therefore calibrate the frequency axis to the PDH-error signal resonances (see section 3.3 which occur at the same frequencies. The largest transmission peaks correspond to the TEM_{00} modes, while a higher order transverse mode with smaller amplitude is visible, this behavior is discussed in section 2.1.4. All signals are normalized to their maximum value.

The data of (2.6) is an average of three measurements. One known source of error in this measurement are non-linearities in the frequency scan of the laser. The scan is performed by applying a saw-tooth voltage to the piezo-controlled laser grating which tunes the laser frequency. At the maxima and minima of the sawtooth, the piezo, which has a maximum scanning frequency of about 1 kHz, will show a non-linear behavior which broadens the signal at these positions. This can lead to an over-estimate of the FSR. Great care was taken to avoid this behavior.

The **Finesse** F introduced before is a measure for "the quality of a cavity" [10] or "the resolving power" [9]. It is, for all three generations of transfer cavities, given by

$$F = \frac{\pi\sqrt{R}}{1-R} = 2616 \tag{2.7}$$

where R is the mirror intensity reflectivity. $R = 99.88\ \%$ is the same for all mirrors of the three transfer cavities. Close to a resonance, we can expand

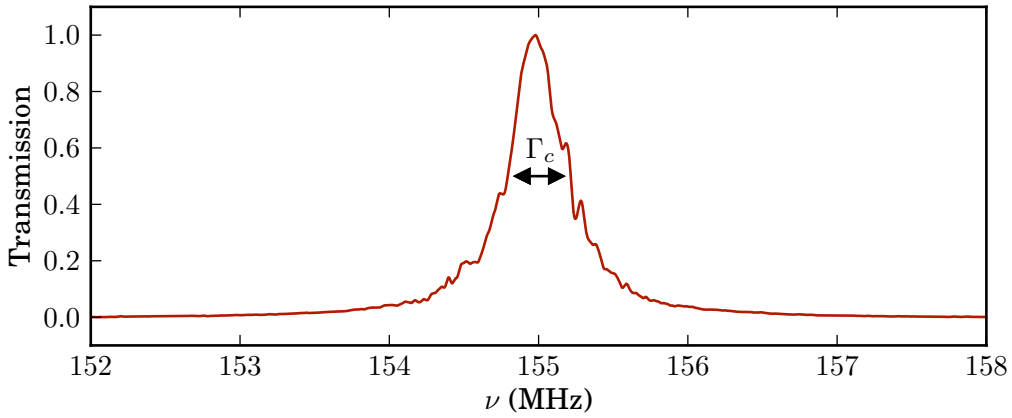

Fig. 2.6: The power transmitted through C_1 is shown in red. By calibrating the x-axis on the known laser sideband frequencies (not shown) we obtain the cavity linewidth Γ_c. All signals are normalized to their maximum value.

(2.3) and obtain a Lorentzian cavity transmission lineshape

$$P_t = \frac{1}{\left[1 + \left(\frac{\widetilde{\nu}}{\Gamma_c/2}\right)^2\right]} P_{in} \tag{2.8}$$

where Γ_c is the **linewidth of the cavity**, i.e. the full width at half maximum of the cavity resonance, which is in a good approximation given by

$$\Gamma_c \approx \frac{\Delta\nu_{ax}}{F} = 396 \text{ kHz } (C_3) \tag{2.9}$$

We can again measure the cavity linewidth Γ_c from a frequency scan over the cavity resonance, where the frequency axis is calibrated to laser sidebands of known frequencies, see figure 2.6. The resulting Lorentzian transmission curve given by (2.8) contains the cavity linewidth Γ_c, but the cavity transmission signal is convoluted with the laser emission spectrum which has a certain linewidth Γ_l itself. Assuming a Gaussian lineshape for the laser emission spectrum which is dominated by technical noise and a Lorentzian frequency spectrum for the cavity transmission, we can fit a Voigt-function to the data of the scan. From [12] we can approximate the linewidth with a precision of 2×10^{-4} to

$$\overline{\Gamma} \approx 0.5346\Gamma_c + \sqrt{0.2166\Gamma_c^2 + \Gamma_l^2} = 425 \text{ kHz} \tag{2.10}$$

where $\Gamma_c \approx 400$ kHz and $\Gamma_l \approx 100$ kHz on a timescale of 5 μs [13]. The final accuracy in (2.10) is much lower than the quoted 2×10^{-4} and is limited by

the uncertainties in the laser linewidth and cavity linewidth. From a fit of a Voigt profile to the data of the resonance scan, where we extract the width of the Lorentzian component which is associated to the cavity linewidth, we obtain

$$\begin{aligned} C_1 &: \ \Gamma_c = 424(24) \text{ kHz} \\ C_2 &: \ \Gamma_c = 443(20) \text{ kHz} \\ C_3 &: \ \Gamma_c = 418(57) \text{ kHz} \end{aligned} \tag{2.11}$$

in good agreement with our estimate. The data (2.11) was averaged over seven measurements. The linewidth measurement of C_1 is exemplary shown in figure 2.6. The laser linewidth of $\Gamma_l \approx 100$ kHz from [13] strongly depends on the measurement time and is an average quantity for the laser model used. Due to these huge uncertainties we will neglect the finite laser linewidth and assume that (2.11) represents solely the cavity linewidth Γ_c. This approach seems justified if we compare the measured results of the cavity linewidth (2.11) with the theoretical prediction (2.9), which deviate by less than 10 % with respect to each other. Using (2.9) we calculate the **Finesse** from the measured frequencies (2.11) and (2.6) to

$$\begin{aligned} C_1 &: \ F = 2274(130) \\ C_2 &: \ F = 2176(98) \\ C_3 &: \ F = 2355(343) \end{aligned} \tag{2.12}$$

and by inverting (2.7) we obtain the **mirror intensity reflectivities**

$$\begin{aligned} C_1 &: \ R = 99.86(1) \ \% \\ C_2 &: \ R = 99.86(1) \ \% \\ C_3 &: \ R = 99.86(2) \ \% \end{aligned} \tag{2.13}$$

The measured Finesse agree fair enough with the theoretical calculation, the intensity mirror reflectivities are close to the specified $R = 99.86(1)$ %.

The cavity **ring-down time** measures the timescale on which the cavity reacts to changes in the power of the incoming beam. On timescales shorter than the ring-down time, fluctuations in the power of the transmitted and the cavity field are low pass filtered and accordingly correlated. The ring

down time is given by

$$\tau_c = \frac{1}{2\pi\Gamma_c} = 0.42\ \mu\text{s}\ (C_3) \tag{2.14}$$

and the cavity **cut-off frequency**

$$\nu_c = \frac{1}{\tau_c} = 2.4\ \text{MHz}\ (C_3) \tag{2.15}$$

which represents a threshold above which intensity fluctuations are correlated. From the measurement results of the cavity linewidths (2.11) we calculate the measured ring-down times to

$$\begin{aligned} C_1 &: \ \tau_c = 0.38(2)\ \mu\text{s} \\ C_2 &: \ \tau_c = 0.36(2)\ \mu\text{s} \\ C_3 &: \ \tau_c = 0.38(6)\ \mu\text{s} \end{aligned} \tag{2.16}$$

and we obtain measured cut-off frequencies of

$$\begin{aligned} C_1 &: \ \nu_c = 2.7(2)\ \text{MHz} \\ C_2 &: \ \nu_c = 2.8(2)\ \text{MHz} \\ C_3 &: \ \nu_c = 2.8(2)\ \text{MHz} \end{aligned} \tag{2.17}$$

A direct ring-down measurement would determine the cavity linewidth Γ_c independently of the laser linewidth Γ_l, but it increases the complexity of the measurement setup. We see that the cut-off frequencies are on the order of several MHz, therefore a direct ring-down measurement requires fast beam on/off switching and a fast photo diode to detect the transmission signal which should both react on the order of < 100 ns. An attempt of a ring-down measurement failed due to the effective photo diode bandwidth of about 1 MHz, where the diode showed a reliable linear behavior, and the inaccurate switch-off process which was done by first locking and then quickly unlocking the laser. The ring-down measurement of C_2 is exemplary shown in figure 2.7, the resulting ring down time of $\tau_c = 1.11\ \mu$s from an exponential fit is largely overestimated.

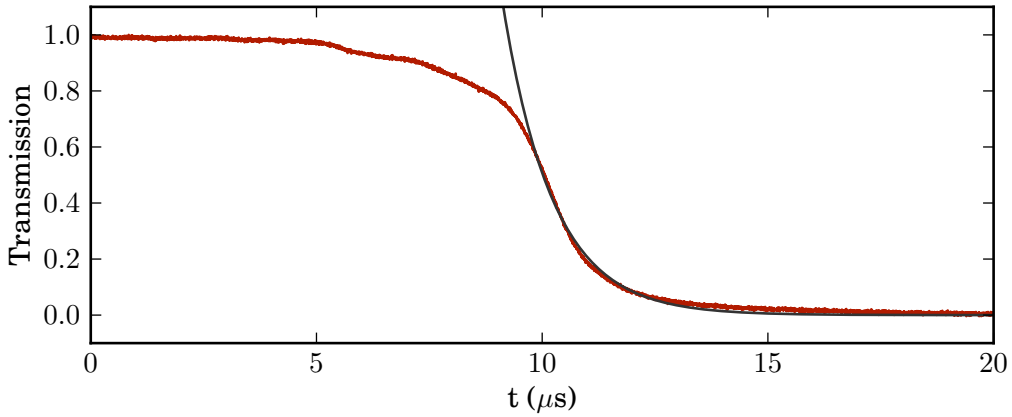

Fig. 2.7: Ring-down measurement of C_2, the signal tail is fitted with (A.36). The cavity transmission signal is normalized to the maximum transmission. The measurement was limited by the effective photo diode bandwidth of about 1 MHz and the inaccurate switch-off process.

2.1.4 Higher order transverse cavity modes

In addition to the axial field modes, which are separated by the free spectral range, a cavity also supports different transverse field modes, see appendix B. Each transverse field mode has a different phase relation. This leads to different resonance frequencies of these modes in the cavity. Depending on the mirror geometry, we distinguish between Hermite - Gaussian and Laguerre - Gaussian field modes. In practice the Hermite - Gaussian field modes dominate and we can neglect the Laguerre - Gaussian field modes. In the cavity design, we try to avoid an overlap between the transverse and the axial field modes. As the amplitude of the transverse field modes in a well coupled cavity decrease rapidly with the mode number, we only need to take into account a frequency range of one or two FSR. The frequencies with respect to a cavity resonance of the transverse field modes are then given by [10]

$$\Delta\nu_{nm} = \frac{(n+m+1)\cos^{-1}(\pm\sqrt{g_1 g_2})c}{2\pi L} \tag{2.18}$$

where the sub index corresponds to the nm-th Hermite polynomial. The transverse mode frequency spacing then is

$$\Delta\nu_{tr} = \frac{c}{2\pi L}\cos^{-1}(\pm\sqrt{g_1 g_2}) = 257 \text{ MHz } (C_3) \tag{2.19}$$

The fourth-order transverse field mode is located at 1029 MHz above the cavity resonance, which is still 7 MHz or $16 \times \Gamma_c$ from the next axial field

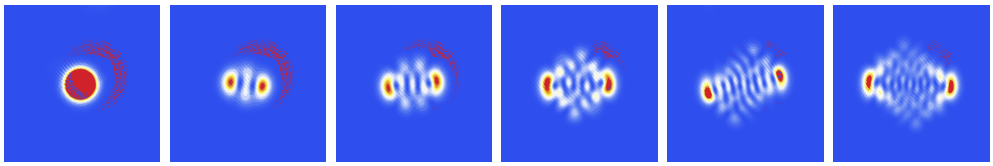

(a) TEM_{00} *(b)* TEM_{02} *(c)* TEM_{04} *(d)* high TEM mode *(e)* high TEM mode *(f)* high TEM mode

Fig. 2.8: Transverse electric field modes (TEM_{nm}) captured with a camera when coupling into the cavity. The higher order transverse modes result from a misalignment of the beam with respect to the cavity. The transverse modes of TEM_{03} upwards are a superposition of several modes, which are a result of the wide laser frequency scan over several cavity modes during the alignment. The halo present on the pictures is an artifact of the camera.

mode at 1036 MHz. We do therefore have no critical mode overlap in the third generation transfer cavity. For the purpose of building a cavity based lock, we try to suppress higher order field modes as much as possible. This is done by carefully mode matching the laser beam which is coupled into the cavity to the cavity. Some measured higher order modes are exemplary shown in figure 2.8.

2.1.5 Cavity incoupling and mode matching

When coupling into an optical cavity, we scan the laser emission frequency over at least one FSR and monitor the transmission through the cavity with a camera. We can improve the coupling by reducing the power in higher transverse modes. In practice this means a reduction of the number of transmission maxima or equally, going from high TEM_{nm} to lower ones, which is equal to going from right to left in figure 2.8. Once a good coupling is reached and most of the power is in the TEM_{00} fundamental mode, we scan the laser over one FSR and send the transmitted light onto a photo diode. This way, we can optimize the coupling through the cavity and reduce the power in the higher order transverse modes further. The quality of coupling reached is indicated by the higher order mode suppression, which gives the factor of power in the largest higher order transverse mode compared to the power in the fundamental mode.

To investigate the coupling of light into the cavity, we need some more theory on the spatial behavior of laser beams. A laser beam inside an optical

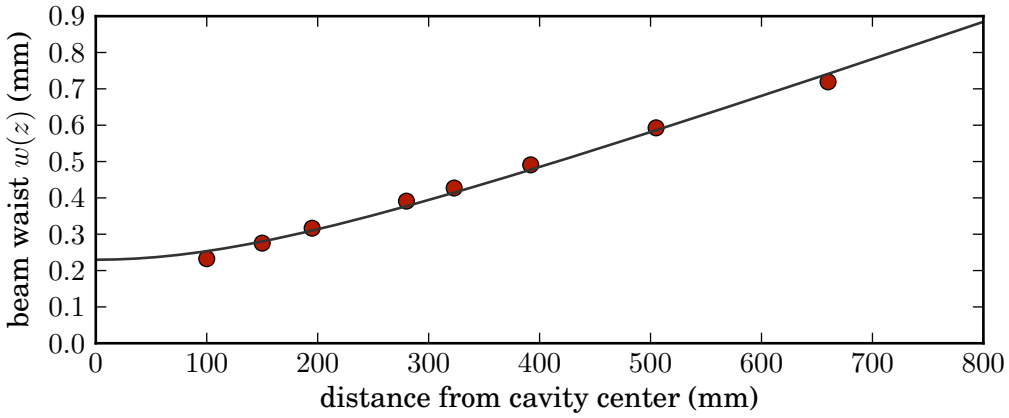

Fig. 2.9: The beam waist at varying distances from the center of the third generation transfer cavity is shown. We obtained a waist of $w_0 = 230$ mm and a Rayleigh range of $z_0 = 215$ mm from a fit of a Gaussian beam to the field distribution measured by a Point Gray camera.

cavity is well described by a Gaussian beam, see appendix B. We now introduce the beam waist w which is half of the beam diameter. In our symmetric cavity, the beam has a minimal waist w_0 at the center of the cavity which is given by [11]

$$w_0 = \sqrt{\frac{\lambda}{L}\sqrt{\frac{(R_1^c - L)(R_2^c - L)(R_1^c + R_2^c - L)}{(R_1^c + R_2^c - 2L)^2}}} = 209\ \mu\text{m}\ (C_3) \tag{2.20}$$

The waist $w(z)$ at a position z from the center given by

$$w(z) = w_0\sqrt{1 + \left(\frac{z}{z_0}\right)^2} \tag{2.21}$$

where we introduced the Rayleigh length

$$z_0 = \frac{\pi w_0^2}{\lambda} = 176\ \text{mm}\ (C_3) \tag{2.22}$$

with λ being the wavelength of the laser. The Rayleigh length is often thought of as the limit between the non-linear Gaussian expansion and the linear expansion in the asymptotic limit. We determine the beam waist w_0 at the center of the cavity by measuring the beam which is coupled out of the cavity, see figure 2.9, and fitting (2.21) to it. We obtain a waist of $w_0 = 230\ \mu$m and a Rayleigh range of $z_0 = 215$ mm.

To achieve optimal mode matching, we have to hit the cavity with a beam of the right size and angle. The so called far field divergence angle of the cavity field is given by

$$\theta \approx \frac{\lambda}{\pi w_0} = 0.068\ ^\circ\ (C_3) \tag{2.23}$$

and from the measurement we obtain 0.1 °. In the following, we want to show the experimental measures taken to optimize the mode matching of the laser beam to the cavity.

The beam directed at the cavity was first coupled out of an optical fiber with a Thorlabs LT110P-B outcoupling lens with a focal length of $f = 6.24$ mm. The outcoupled beam had a waist of 0.61 mm, we would have therefore needed a cavity coupling lens of $f \approx 500$ mm positioned at about 500 mm from the cavity center, as can be deducted from figure 2.9. To be able to exchange the third generation transfer cavity with the second generation in the experiment, we have to keep the cavity coupling lens of $f = 300$ mm. Accordingly, we would need a beam waist of about 0.4 mm to keep the $f = 300$ mm coupling lens at the current position of about 300 mm from the cavity center and to achieve a good mode match. By knowing that a $f = 6.24$ mm fiber outcoupler yields a beam waist of 0.61 mm, we can calculate the focal length of an outcoupler which would yield a beam waist of 0.4 mm and obtain a desirable focal length of $f = 4.09$ mm, which was not available. We therefore used a Thorlabs LT230P-B outcoupling lens with a focal length of $f = 4.5$ mm. By tuning the outcoupling lens slightly out of focus, we were able to achieve a good mode match.

After optimizing the input coupling into the cavity, we could suppress the power in the higher transverse modes compared to the fundamental mode by a factor of > 250. The position of the beam was about 2 mm off from the center on both cavity mirrors after repeated optimization. This did not affect the higher mode suppression noticeable.

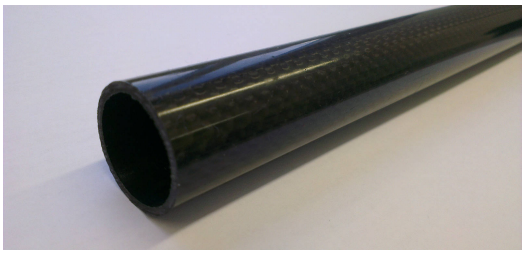

Fig. 2.10: The CFK tube used in uni-directional configuration is shown. The tube is wrapped in woven carbon fiber.

2.2 Thermal properties of the cavity

We now want to focus on the thermal properties of the cavity. Our goal was to build a frequency stable, temperature tuned cavity. To achieve the desired tune ability of a few FSR for a change in temperature of a few Kelvin and to decouple the cavity from environmental temperature changes, we designed the cavity in such a way as to minimize thermal expansion. This was done by choosing materials with a low coefficient of thermal expansion as well as an elaborate mechanical design to cancel or suppress the remaining thermal expansion. In this section we want to present the design approach taken and show the results obtained.

2.2.1 Materials and design

The heart of the cavity is a carbon fiber spacer tube which separates the cavity mirrors. Carbon fibers have a very low coefficient of thermal expansion (CTE) along the direction of the fiber of $\alpha_T = -(0.1 - 1) \times 10^{-6}$ K^{-1} at room temperature, which varies slightly depending on the exact mixture of the composite fiber materials used [14]. In contrast to most other materials, CFK slightly shrinks when heated. Perpendicular to the direction of the fiber, the CTE of CFK is about $\alpha_T = (10 - 20) \times 10^{-6}$ K^{-1} [15]. There exist many different types of CFK composites on the market, where one of the most common ones consists of woven carbon fiber which mixes the CTE in the direction of the fiber and perpendicular to it. To minimize the CTE, we chose a CFK tube which was built of uni-directional CFK, where the carbon fibers lie in parallel with respect to each other. The carbon fibers are cast in epoxy or similar glue and wrapped by woven CFK, see figure 2.10. Due to the stiffness of the carbon fibers in the direction of the fiber, we assume that the mechanical and accordingly, the thermal properties of the uni-directional CFK largely transfer to the complete structure.

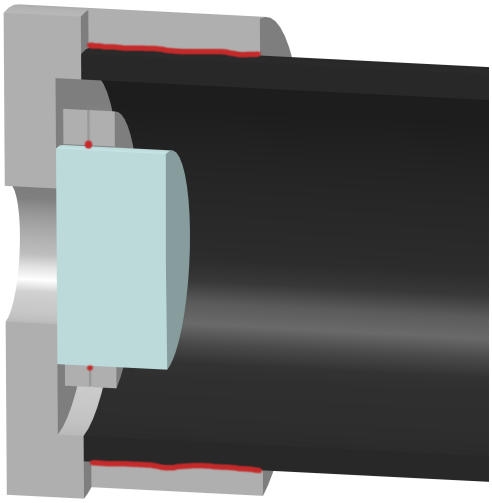

Fig. 2.11: Rendering of the assembly of the mirror to the mirror mount and subsequently to the CFK-cavity spacer tube. The position and design of the glue is shown in red.

If we compare the CTE of CFK to the CTE of aluminum of $\alpha_T = (22 - 24) \times 10^{-6}$ K^{-1} and commonly used glues like epoxy with $\alpha_T = (50 - 80) \times 10^{-6}$ K^{-1}, we see that CFK is by far less temperature sensitive. Due to this huge difference in the CTE, 150 mm of CFK tube, 7 mm of aluminum or 2 mm of glue show roughly the same thermal expansion. The three materials are used in approximately these quantities in our transfer cavity, it is therefore crucial to minimize the effect of the aluminum and the glue on the total thermal expansion of the system, as they would largely diminish the positive effect of the CFK on the CTE of the complete system.

We see that we can improve the most in the CTE of the glue, as it is by far the largest. We chose to use MasterBond EP21TCHT-1 to glue the mirrors to the mirror mounts, which has a very low CTE for a glue with $\alpha_T = (18 - 20) \times 10^{-6}$ K^{-1} [16]. In addition, we try to keep the thermal expansion of aluminum and glue along the cavity axis close to zero. This is done by gluing the mirrors to the aluminum mounts in the radial direction using small dots of glue. Any thermal expansion of the glue should therefore only apply a negligible stress on the mirrors without moving them in the axial direction as it can only expand in the radial direction. The thermal expansion of 1 mm of MasterBond EP21TCHT-1 glue when heated by 10°C

is only

$$\Delta L = L_0 \alpha_T \Delta T \approx 200 \text{ nm} \tag{2.24}$$

The mirrors are glued to the aluminum mounts in such a way that the aluminum expands in both directions. While the mirrors are pushed inwards when the aluminum expands, the mounts are pushed outwards. If the gluing position is chosen carefully at the height of the end of the CFK tube, these expansions should exactly cancel, see figures 2.2 and 2.11.

The mirror mounts are also glued in the radial direction to the CFK tube. Here standard two component epoxy glue with a CTE of about $\alpha_T = (50 - 80) \times 10^{-6}$ K^{-1} was used and applied in 10 mm stripes. Where glued together, the stiff CFK should hinder the thermal expansion of the soft aluminum. We therefore glued the aluminum mirror mounts up to the end of the CFK-tube, which together with the central gluing position of the mirrors should eliminate the thermal expansion of the aluminum all together. The assembly of mirror, mirror mount, CFK-spacer tube and the gluing positions are shown in figures 2.2 and 2.11.

2.2.2 Sensitivity to length and temperature change

To evaluate the effectiveness of the cavity design presented in section 2.2, we need to link changes in the resonance frequency of the cavity to length changes and subsequently, to temperature changes. From (2.3) and (2.5) we see that the positions of the resonances mainly depend on the length of the cavity. It is therefore useful to introduce the sensitivity of a cavity resonance to length change, S_L. It can be derived from the principle that a resonance in the cavity occurs when the wavelength of the field is an integer multiple of the round trip length of the light in the cavity 2 L.

$$\begin{aligned} N\lambda &= 2L \\ -N\frac{c}{\nu_c^2}\delta\nu_c &= 2\delta L \\ -\frac{2L\nu_c}{c}\frac{c}{\nu_c^2}\delta\nu_c &= 2\delta L \\ S_L := \frac{\delta\nu_c}{\delta L} &= -\frac{\nu_c}{L} \end{aligned} \tag{2.25}$$

By integrating (2.25), we can compute the frequency change with respect to the length change, see (2.26).

$$\int_{\nu_c}^{\nu_c+\Delta\nu_c} \frac{1}{\nu'} d\nu' = -\int_{L_0}^{L_0+\Delta L} \frac{1}{L'} dL'$$

$$\Delta\nu_c = -\frac{\nu_c}{L_0+\Delta L}\Delta L \approx -\frac{\nu_c}{L_0}\Delta L = S_L \Delta L \tag{2.26}$$

Assuming linear thermal expansion of the cavity with a CTE of α_T we get the axial expansion of the cavity

$$L(T) = L_0(1+\alpha_T T) \tag{2.27}$$

We can now derive the thermal frequency sensitivity S_T of the optical cavity from (2.26)

$$\Delta\nu_c = -\frac{\nu_c}{1+\alpha_T\Delta T}\alpha_T\Delta T \approx -\nu_c\alpha_T\Delta T \tag{2.28}$$

For most materials, α_T is on the order of 10^{-6} K^{-1}, we can therefore approximate $1+\alpha_T\Delta T \approx 1$. We obtain the sensitivity of a cavity to temperature changes

$$S_T := \frac{\delta\nu_c}{\delta T} \approx -\nu_c\alpha_T \tag{2.29}$$

From a measurement of $\Delta\nu_c$ and ΔT we obtain the coefficient of thermal expansion

$$\alpha_T \approx -\frac{1}{\nu_c}\frac{\Delta\nu_c}{\Delta T} \tag{2.30}$$

We measure a frequency change of about one free spectral range when the temperature changes by 1.6 K for the third generation transfer cavity when hit with a 780 nm laser. We therefore obtain a coefficient of thermal expansion of $\alpha_T = 1.7\times10^{-6}$ K^{-1}. This value is larger than what we would expect of pure CFK, but more then ten times small than the CTE of aluminum and the MasterBond glue, and about 40 times smaller then the CTE of epoxy. We therefore conclude that the thermal expansion of the glues and the aluminum in the axial direction has been largely suppressed. The residual CTE is desirable, as we need some sensitivity to temperature changes to be able to thermally tune the cavity resonance frequency on the order of a few FSR.

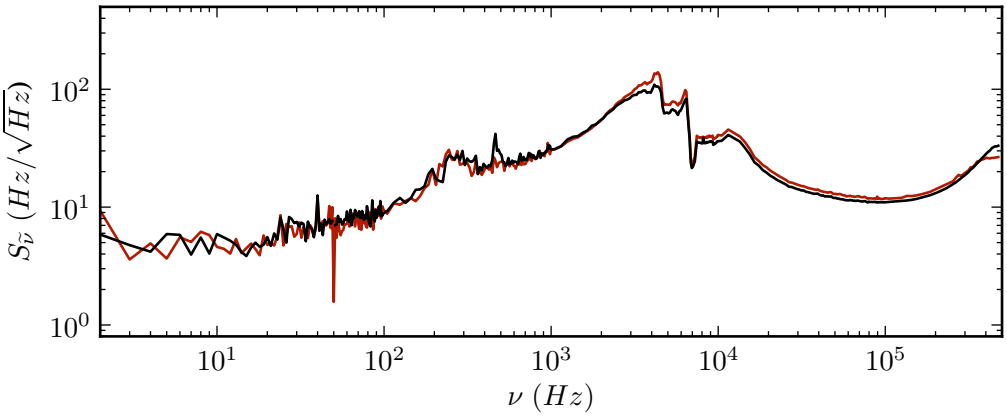

Fig. 2.12: The noise spectral density of the third generation transfer cavity is shown, a background measurement with the laser switched off was subtracted. An average of 31 measurements is shown. The measurement with the aluminum post is shown in red, while the measurement with the Teflon post is shown in black. We see a clear reduction in the noise spectral density over the whole frequency range, the small enhancement at 500 kHz results from a non-optimally adjusted laser current feedback loop close to the lock bandwidth of about 800 kHz.

In day to day operation, the largest source of thermal noise on the cavity is airflow. To suppress airflow and to add thermal isolation, we put a wooden housing on top of the cavity. The wooden box largely suppresses fast temperature changes from convection. This improves the thermal stability of the system a lot and largely eliminates the influence of people moving in the room. In addition, the cavity is encased by brass shells which serve as a thermal reservoir and are therefore equivalent to a thermal low pass. The CFK tube and the brass shells were connected together with thermal compound.

2.3 Mechanical properties of the cavity

Carbon fibers are very stiff in the direction of the fiber with an ultimate tensile stress of about 4000 N/mm^2, while the mechanical properties perpendicular to the fiber direction are largely determined by the type of carbon fiber composite (CFK) used. They show in general a much lower ultimate tensile stress. We already saw a similar behavior when we investigated the thermal properties of the cavity. To achieve the largest ultimate stress in the axial direction, we again want a CFK tube made from an uni-directional fiber assembly. If we compare the ultimate stress of CFK to the ultimate stress

of aluminum, we see that CFK is much stiffer. Aluminum has an ultimate tensile stress of about 45 N/mm^2 (pure) to (300-700) N/mm^2 (alloy). This stiffness makes CFK an ideal material to protect the cavity against mechanical deformation like acoustic or vibrational oscillations.

The cavity mount was designed to reduce the coupling of mechanical vibrations from the optical table to the cavity. To do so, the CFK-spacer tube was first encased by brass shells. This adds weight to the cavity and together with Sorbothane shock absorbers positioned between the cavity and the cavity mount, functions as a mass-spring system, which serves as a low pass filter for vibrational excitations. The cavity was placed on a 40 mm diameter Teflon post which is a bad acoustic conductor. The Teflon post damps vibrations which couple to the cavity from the optical table, the effect is shown in figure 2.12. We could lessen the spectral noise density in the ten kilohertz range by roughly 25% by switching from an aluminum post to a Teflon post, as well as noise around 250 Hz. The evaluation of the spectral noise density shown here will be explained in chapter 3, it is directly correlated to mechanical noise.

The wooden box placed around the cavity further decouples the system from the environment. It adds acoustic damping to the system with a combination of dense and heavy MDF-wood on the outside and a light foam lining on the inside. The whole system was positioned on an actively stabilized optical table with a resonance frequency of about 1 Hz. The table decouples the cavity from the ground floor, but vibrations coupled from the air to the table as well as vibrations generated on the table will not be damped.

Both spectra in figure 2.12 show a significant amount of mechanical noise in the acoustic region around 4 kHz, which was damped by the Teflon post but is still present.

3. CAVITY LOCK CHARACTERISTICS

A free running laser always shows a finite amount of frequency instability. This instability can be separated into various frequency regions which have to be treated quite differently. A rough but practical approach is to separate slow changes in the emission wavelength, which usually occur on a timescale of several seconds to days, from fast frequency changes, which usually occur on a timescale of < 1 s. While slow frequency changes affect the long term stability of the laser, fast changes affect the short term stability and determine the linewidth of the laser.
To improve the long term stability of the laser, we can stabilize it to a frequency reference like a spectroscopy cell, a wavemeter, a GPS-signal, a frequency comb, etc., which has a stable frequency resonance on a large timescale.
In a similar manner, we can improve the short term stability and narrow down the linewidth of the laser by actively stabilizing the laser to a frequency reference that is more stable than the laser, like an optical cavity.

This stabilization of a laser onto a frequency reference is called *locking* and is a standard procedure to produce a frequency stable laser, for more information see e.g. [9, 10].

3.1 Laser fluctuations and noise

A laser system shows various types of noise. In this section, we want to look at intensity, polarization and frequency fluctuations. These types of fluctuations are quite different in nature and will be discussed in detail in the following sections.

3.1.1 Amplitude/intensity fluctuations

Fluctuations in the amplitude of the field emitted by the laser $E(r, z)$ will cause intensity fluctuations $\rightarrow I(r, z) \propto |E(r, z)|^2$. These fluctuations are caused by various sources like fast current or temperature fluctuations, mechanical oscillations or a change in the dominant transverse emission field

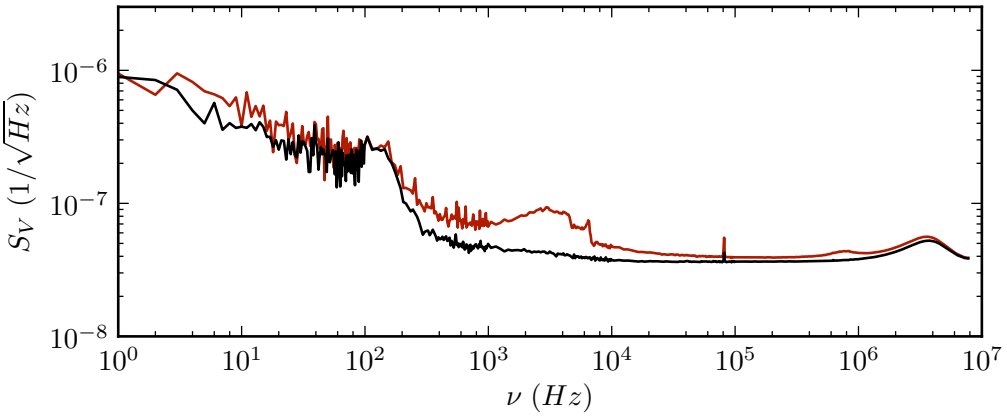

(a) Normalized raw intensity spectrum of the laser (red) and the background (black).

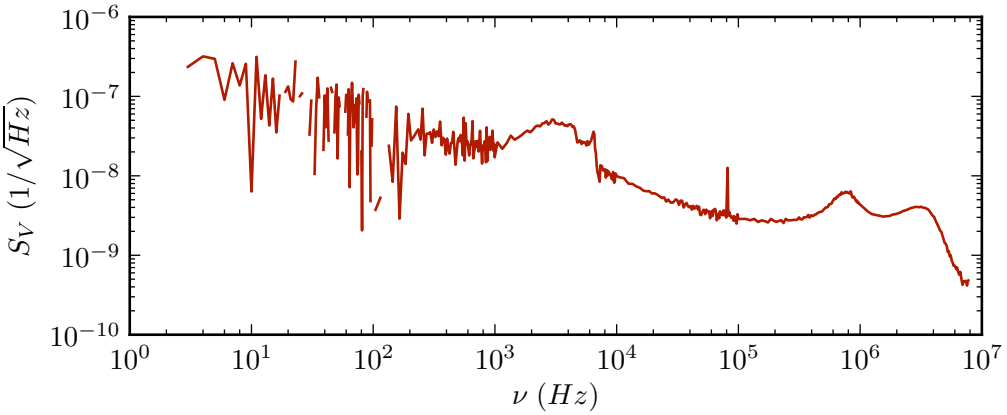

(b) Normalized intensity spectrum of the laser, the background was subtracted.

Fig. 3.1: The normalized intensity noise spectrum of the laser locked to the first generation transfer cavity averaged over ten measurements is shown. The signal was normalized to the mean intensity. We see enhanced intensity noise between 3 - 4 kHz and at 82 kHz. The noise at 800 kHz results from the bandwidth of the lock laser current feedback loop, while the enhancement at 3 MHz corresponds to the DC-photo diode bandwidth which is specified up to a maximum of 10 MHz.

mode.

It is possible to strongly suppress amplitude fluctuations of a laser by an active temperature control, a vibration-damped optical table and by operation at a single longitudinal mode. These measures are commonly used and very effective. They have been implemented in our laser setup and suppress amplitude fluctuations to 10^{-7} standard deviation normalized to the mean intensity, while the maximum deviation is 10^{-3}. In stable single mode operation, amplitude fluctuations happen on the order of fractions of a second, while long term drifts are usually quite small. Most measured long term drifts in intensity arise from beam alignment drifts and consecutive decreasing coupling efficiencies through various optical elements.

Intensity fluctuations can be measured directly with a photo diode, the output voltage V_{el} is directly proportional to the photo current I_{el} which is directly proportional to the beam power P and intensity $I(r, z)$

$$V_{el} \propto I_{el} \propto P \propto I(r, z) \propto |E(r, z)|^2 \tag{3.1}$$

The output voltage can be measured with high temporal resolution by an oscilloscope. The normalized raw spectrum of the intensity noise and a background measurement with the photo diode covered are shown in figure 3.1a. We see that the features in the intensity spectrum above 100 Hz indeed result from the laser intensity noise, as they are not present in the background. The background measurement is shown as a reference of the behavior of the photo diode. The normalized intensity spectrum with subtracted background is shown in figure 3.1b. We see enhanced intensity noise in the region of 3 - 4 kHz.

3.1.2 Polarization fluctuations

Our laser system contains polarization sensitive elements like polarizing beam splitters and waveplates. These elements transform changes in polarization into intensity changes. One source of error are optical fibers which transform mechanical and temperature variations into polarization variations. It is possible to strongly suppress these variations by using polarization maintaining fibers, where the axis of polarization has to be aligned along one of the two polarization maintaining fiber axes. Therefore circular polarization components have to be canceled. This was done by placing a $\lambda/2$ and a $\lambda/4$ waveplate in front of the fiber and adjusting the axis of polarization accordingly. The ratio of circular to linear polarization was measured with a

Schaefter + Kirchhoff SK010PA polarization analyzer and a circular polarization suppression of 99.5% was achieved.

The resulting beam had a stable axis of polarization and the influence of polarization changes in the optical setup could be accounted for by careful adjustments. The residual drifts were small in amplitude and slow in frequency and were therefore neglected in our measurements.

3.1.3 Phase/frequency fluctuations

Phase fluctuations $\Delta\Phi$ and frequency fluctuations $\Delta\nu$ are linked by

$$\Delta\nu := \frac{1}{2\pi}\frac{d(\Delta\Phi)}{dt} \tag{3.2}$$

We will usually talk about frequency fluctuations when characterizing the laser and the cavity as they are a more convenient quantity to work with. "Both the short-term frequency jitter and the long-term frequency drift of a laser oscillator usually result primarily from mechanical vibrations and noise, thermal expansion, and other effects that tend to chance the length L of the laser cavity." [9]

The very limit on the laser frequency linewidth is given by the *Schawlow-Townes formula*, where the linewidth is only limited by quantum noise fluctuations resulting from the spontaneous emission from the lasing atoms. The original form of the Schawlow-Townew formula [17] was later on modified to give the correct linewidth for lasing operation above the lasing threshold [18]. The modified form of the Schawlow-Townew formula reads

$$\Gamma_l = \frac{2\pi h\nu\Gamma_c^2}{P_l} \tag{3.3}$$

Here Γ_l is the laser emission linewidth (full width at half-maximum), ν is the photon frequency, Γ_c is the cavity linewidth and P_l is the output power of the laser. The Schawlow-Townes limit "[...] can be observed with great difficulty only on the very best and most highly stabilized laser oscillators." [9] For the laser used [13] the Schawlow-Townes limit equates to 1 - 10 μHz for a laser output power of 10-100 mW. Accordingly, the system built certainly operates above the Schawlow-Townes limit, we are not limited by quantum fluctuations but by fluctuations from mechanical vibrations and thermal expansion.

We now want to focus on short-term frequency jitter as we can compensate for long term drifts by locking our system to an absolute frequency reference, in our case a HighFinesse WS/7 wavemeter [19]. In accordance to the central limit theorem we assume a Gaussian distribution for the mechanical vibrations and thermal noise amplitudes, the sources of short-term frequency fluctuations.

In accordance to [18], we assume the phase and frequency of the laser to be

$$\nu(t) := \frac{d\Phi}{dt} = G(t)\cos(\Phi + 2\pi\nu_0 t) \tag{3.4}$$

where ν_0 is the frequency of the laser, $\Phi + 2\pi\nu_0 t$ is the total phase and $G(t)$ is a random variable linearly proportional to the input noise source. The noise and subsequently $G(t)$ is assumed to be approximately white and Gaussian distributed. From [18] we further see that this type of noise results in a Lorentzian line broadening of the laser resonance with

$$G(\nu) = \frac{G_{max}}{1 + \left(\frac{\nu-\nu_0}{\Gamma_l/2}\right)^2} \tag{3.5}$$

In general, we would expect this Lorentzian frequency distribution for a laser limited by quantum noise [20, 21], while under certain conditions of low-pass filtered input noise the laser will have a Gaussian line shape [20]. In the experiment, the laser is usually limited by technical noise which yields a Gaussian frequency distribution.

A more intuitive definition which combines amplitude, phase and frequency fluctuations is given in [22]

$$E(t) = [E_0 + \varepsilon(t)]\sin[2\pi\nu t + \Phi(t)] \tag{3.6}$$

where $\varepsilon(t)$ accounts for amplitude fluctuations and $\Phi(t)$ accounts for phase fluctuations. Frequency fluctuations are given by

$$\nu(t) = \nu + \frac{1}{2\pi}\dot{\Phi}(t) \tag{3.7}$$

where we again assume the frequency noise to be approximately white and Gaussian distributed.

3.2 Temperature lock

We want to compensate for very slow drifts of the laser emission wavelength on a timescale of minutes and more by locking it to an absolute frequency reference. Our reference is a HighFinesse WS/7 wavemeter with an absolute accuracy of 60 MHz [19]. The wavemeter outputs a PID error signal of -4 V to 4 V based on the frequency offset of the laser from a set frequency. We feed this error signal to a home built cavity temperature controller (CTC) which is connected to the heating wires wrapped around the cavity. To control the temperature of the cavity, the heating wire and radiative cooling were used. The wire was wrapped around the brass shells of the cavity to achieve a uniform temperature distribution.

3.2.1 Heating wire

To determine the material and the dimensions of the heating wire, several factors had to be taken into account:

- maximum supply voltage of the power supply: 9 V or 15 V, selectable
- maximum supply current: ≈1 A, limited by the power amplifier of the CTC and the power supply
- wire length: very long wires increase the complexity of manufacturing the heater, a maximum of 100 m is therefore reasonable
- wire diameter: very thin wires easily break while thick wires are hard to wind, a diameter of 0.2-1 mm seems therefore reasonable
- wire material: only few materials are commonly used for wires which include copper, aluminum, constantan or Manganin
- wire isolation: for winding the wire without creating short circuits, a good isolation is required. Commonly used isolation include coatings (danger of scratch damage), plastics (thick) and silk (rare).

In the following derivation, a supply voltage of 15 V was assumed. 9 V supply voltage operation is also possible, but this will decrease the available output power by 50 %. The power amplifier of the CTC was realized by a Darlington transistor. The minimum collector-emitter voltage is 1.2V, while an additional transistor of the same type was used for power switching. This

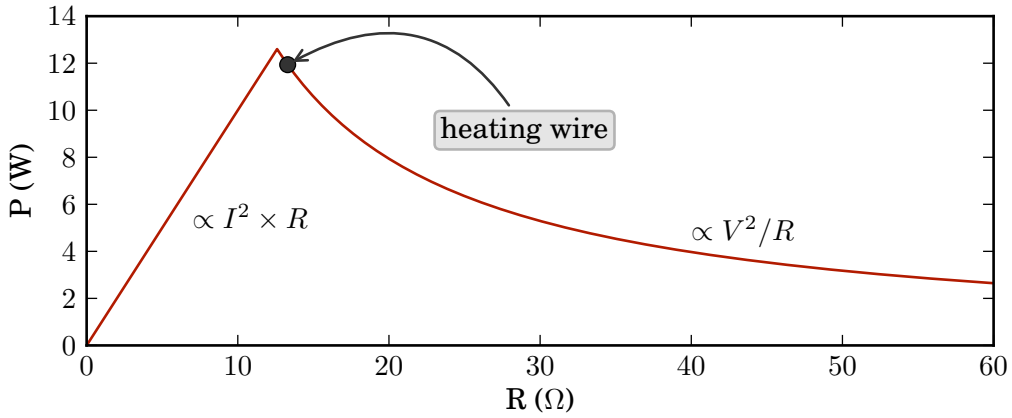

Fig. 3.2: The maximum heating power shows a maximum for a resistance of $R_c = 12.6\ \Omega$. The maximum heating power for the cavity heating wire with $R = 13.3\ \Omega$ of $P = 11.9$ W is shown.

decreases the maximum available output voltage to 12.6V. Theoretically, the maximum heating power therefore is

$$P_{max} = V_{max} \times I_{max} = 12.6\ (\mathrm{V}) \times 1\ (\mathrm{A}) = 12.6\ (\mathrm{W}) \tag{3.8}$$

In reality, the maximum current and accordingly, the maximum heating power are determined by a careful impedance matching of the resistance of the heating wire to the CTC shown in (3.9) and figure 3.2.

$$\begin{aligned} P = I^2 \times R \qquad &\text{with} \qquad I < 1\ (\mathrm{A}) \\ V = R \times I \qquad &\text{with} \qquad V < 12.6\ (\mathrm{V}) \end{aligned} \tag{3.9}$$

To illustrate the meaning of (3.9), let us assume that the heater tries to supply the maximum possible power at a certain wire resistance, with the maximum current always at $I = 1$ A (the power amplifier in the CTC is built from a transistor which behaves as a current source, therefore these assumptions are justified). Then the power $P = I^2 \times R$ scales linearly with R for small resistances, and so does the voltage drop on the resistor, $V = R \times I$. At a certain critical resistance R_c the voltage drop reaches the maximum supply voltage of 12.6 V, where R_c is simply given by Ohm's law

$$R_c = \frac{V_{max}}{I_{max}} = 12.6\ \Omega \tag{3.10}$$

If we increase the resistance further, the voltage drop on the resistor would be larger than the supply voltage, which is unphysical. While the supply

voltage will stay at the maximum level of 12.6 V, the CTC will supply less current so that

$$R \times I = V_{max} \tag{3.11}$$

is always fulfilled. Therefore for a resistance R above R_c we expect the heating power P to behave as $1/R$ given by

$$P = \frac{V_{max}^2}{R} \tag{3.12}$$

This behavior is shown in figure 3.2. The wire used was a 1 mm diameter Manganin wire ($\rho = 0.533\ \Omega/m$, specified) with silk isolation. Manganin is an alloy of copper, manganese and nickel. The wire was wrapped around the brass shells of the cavity in two counter propagating layers to cancel any arising magnetic fields. The calculated length of the wire is 30 m with a measured total resistance of $R = 13.3\ \Omega$. We therefore reach a theoretical maximum heating power of 11.9 W, see figure 3.2, which is close to the maximum possible heating power of 12.6 W. In the end, we want to mainly ensure that the wire and the amplifier impedance are properly matched. If this was not the case, most of the power would be lost on the amplifier, which would need additional cooling, while only little power would be left to temperature control the cavity.

3.2.2 Cavity temperature controller (CTC)

We now want to take a closer look at the electronic design and the temperature regulation of the CTC, a view from the front is shown in figure 3.3. The main purpose of the CTC was to supply the heating wire with power, to show the current cavity temperature and to include safety features to prevent overheating of the cavity or the power amplifier in the CTC. The temperature measurement was done with three PT1000 thermo elements which are positioned in the cavity as shown in figure 3.4. The temperatures are shown on a 4x16 LCD, powered by an Arduino micro controller.

The safety features include a software based interlock which triggers if one of the three temperatures sensors measures a temperature of $T > 35°C$, and a bi-metal switch on the power transistor which cuts the power supply if the temperature on the transistor exceeds 100°C.

The temperature regulation was done via the software of a HighFinesse WS/7 wavemeter with built in digital PID regulator, where only the PI regulator was used. Depending on the difference of the measured laser wavelength

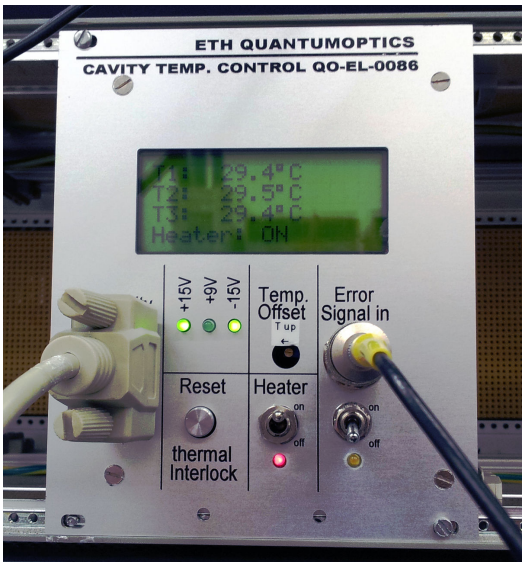

Fig. 3.3: The cavity temperature controller is shown, placed in a 19 inch rack.

to a certain nominal wavelength, the output signal ranges from -4096 mV to +4096 mV and is fed to the CTC, which amplifies the signal and outputs it to the heating wire. To be able to heat and cool the cavity with a single heating source, the reference temperature has to be higher than room temperature. This was achieved by adding an adjustable offset voltage to the PI signal in the CTC which heats the cavity to 26-28°C without a PI signal present, i.e. $V_{PI} = 0$ V, while the offset temperature can be freely chosen between room temperature and the interlock shut-off temperature. The circuit which pre-amplifies the input signal and adds the offset voltage in shown in figure 3.5.

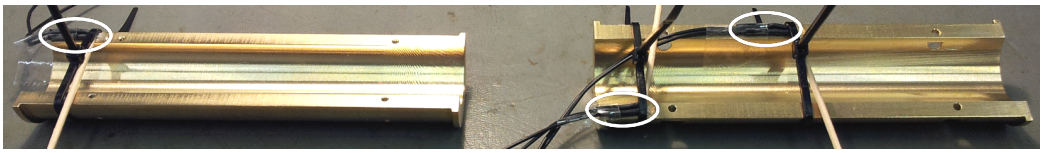

Fig. 3.4: The brass shells which enclose the cavity are shown. The positions of the three PT1000 temperature sensors are highlighted. The PT1000 sensors are glued to the brass with a very thin layer of fast setting superglue.

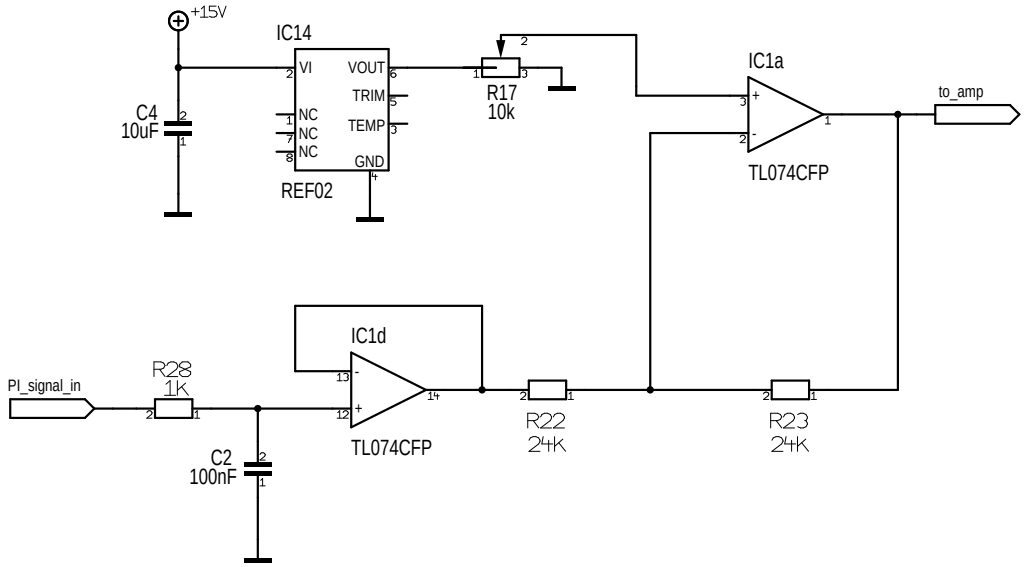

Fig. 3.5: Input circuit of the CTC. The error signal is low pass filtered with R28 and C2, IC1d works as a buffer amplifier. Ref02 is a 5 V precision source which generates an adjustable offset voltage at the non-inverting input of the inverting amplifier IC1a by varying the potentiometer R17. The output of IC1a is connected to the power amplifier stage.

3.2.3 CTC electronics

The input circuit shown in figure 3.5 was subsequently connected to the power amplifier which is shown in figure 3.6. An Arduino micro controller was used to monitor the transistor output, it is also able to interrupt the supply voltage of the power amplifier. The interrupt is software controlled and triggered if the cavity temperature exceeds a predefined threshold temperature (35°C).

The micro controller was mainly used to monitor the cavity temperature with three PT1000 sensors and to output the measured temperatures on a 16x4 character LCD. The circuit shown in figure 3.7 was used to convert the resistance of a PT1000 sensor into a voltage signal for the micro controller's analog input. The analog inputs feature a 10 bit analog-digital converter (ADC), which divides the input voltage of 0 - 5 V into 1024 steps à 4.88 mV.

The temperature region of interest is about 20 - 40°C. We can convert these temperatures to resistances using the PT1000 datasheet [23]. The Ref200 100 μA precision source then induces a voltage drop through these resistances according to Ohm's law.

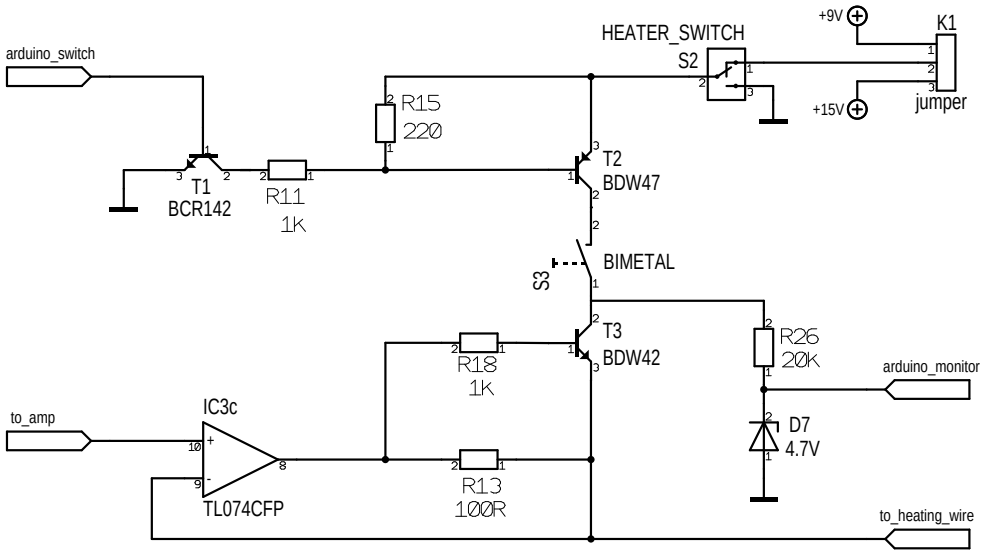

Fig. 3.6: Power amplifier circuit of the CTC. IC3c works as a pre-amplifier and non-inverting regulator for the power transistor T3. The amplifier can be powered by +9V or +15V depending on the jumper position. Furthermore there is a heater-ON/OFF switch S2, a micro controller controlled interlock which is realized by the pre-amplifier T1 and the transistor T2, which works as a switch. The bi metal is an overheat protection for T3 and interrupts the power if the temperature of T3 exceeds 100°C. Arduino_monitor is a monitor output to monitor if the amplifier is on or off.

$$\left.\begin{array}{lcccl} 20°\mathrm{C} & \rightarrow & 1078\ \Omega & \rightarrow & 107.8\ \mathrm{mV} \\ 40°\mathrm{C} & \rightarrow & 1155\ \Omega & \rightarrow & 115.5\ \mathrm{mV} \end{array}\right\} \Delta V = 7.7\ \mathrm{mV}$$

The voltage difference $\Delta V = 7.7$ mV is amplified by the INA118 instrumental amplifier. To protect the TTL inputs of the micro controller, we need to limit the output voltage to -0.5 - 5.5 V. This is done by adding a voltage divider to the instrumental amplifier output ($V_{\mathrm{to\_arduino}} = 1/3\ V_{\mathrm{INA118}}$) and a Schottky diode, which has a low threshold voltage of 0.4 V, see figure 3.7. The INA118 amplifies the differential voltage linearly up to 13 V, with 14 V being the highest output voltage. These limits set the voltage gain G (3.13), the according resistor to set the gain of the INA118 can be calculated from (3.14).

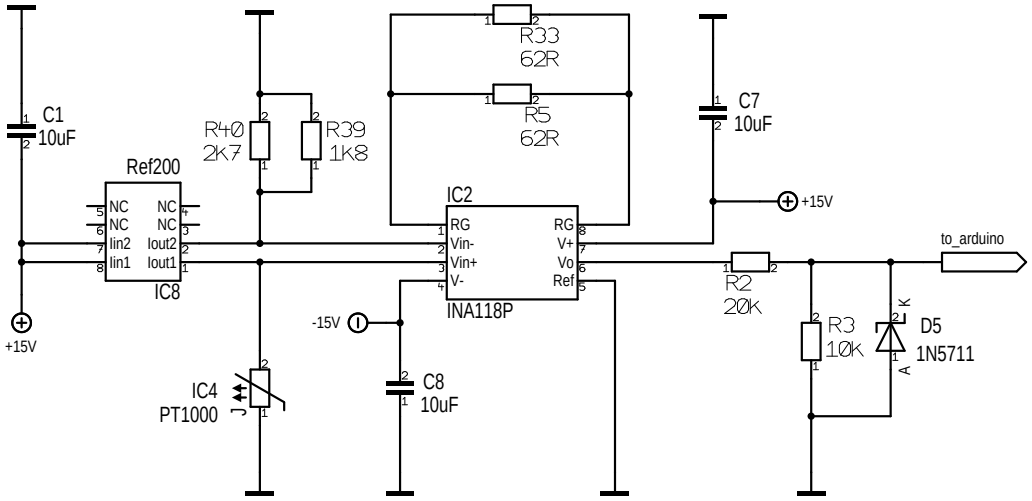

Fig. 3.7: PT1000 sensor circuit of the CTC. The precision current source Ref200 outputs a current of 100 μA, which yields a small differential voltage between R39/R40 and the temperature sensor PT1000. The instrumental amplifier INA118P amplifies this differential voltage depending on the gain set by R5/R33. R2, R3 and D5 limit the output voltage to -0.5 - 4.7 V to protect the TTL inputs of the micro controller.

$$G = \frac{V_{max}}{\Delta V} \tag{3.13}$$

The equation for the gain resistor is given in the datasheet of the instrumental amplifier INA118 [24]

$$G = 1 + \frac{50\ \text{k}\Omega}{R_G} \qquad \Rightarrow \qquad R_G = \frac{50\ \text{k}\Omega}{G - 1} \tag{3.14}$$

Due to the finite stepping of resistances available, the final performance of the circuit is slightly altered to the theoretical one. For the lower temperature measurement bound we arranged a 1.8 kΩ and a 2.7 kΩ resistor in parallel to get a resistance of $R_{low} = 1080\ \Omega$ which corresponds to the resistance of the PT1000 at $T_{low} = 20.5°C$. Keeping ΔV = 7.7 mV, the upper temperature measurement bound shifts to 40.5°C. From (3.13) we get G = 1688 using V_{max} = 13 V and from (3.14) we get $R_G = 29.6\ \Omega$. For R_G two 62 Ω resistors in parallel were chosen (see figure 3.7) which yields a total resistance of $R_G = 31\ \Omega$ and a gain of G = 1614, see (3.14). The theoretical results and the parameters used are summarized in table 3.1.

	theoretical value	value used
R_{low}	1078 Ω	1080 Ω
T_{low}	20°C	20.5°C
V_{low}	107.8 mV	108.0 mV
R_{high}	1155 Ω	1157 Ω
T_{high}	40°C	40.5°C
V_{high}	115.5 mV	115.5 mV
ΔV	7.7 mV	7.7 mV
G	1688	1614
R_G	29.6 Ω	31 Ω
$V_{\text{to\_arduino}}(T_{low} - T_{high})$	0 - 4.33 V	0 - 4.14 V
ADC	0 - 887	0 - 848
ADC/°C	44.37	42.42

Tab. 3.1: Overview on the parameters and properties used in the cavity temperature controller (CTC).

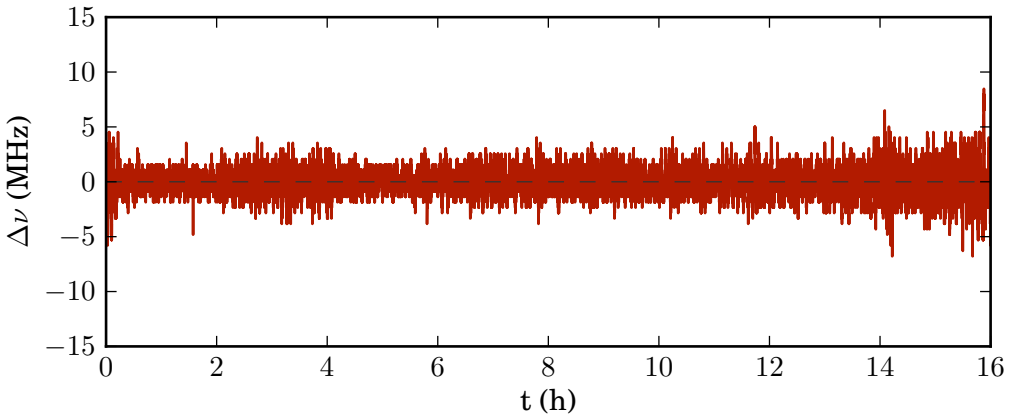

Fig. 3.8: Frequency deviations around the set point of 384.1950000 THz are shown. The mean is 8 kHz below the set frequency, while the standard deviation from the mean is 1.8 MHz. The laser stayed locked throughout the measurement.

3.2.4 Long term frequency stability

The main goal of this work was to develop a PDH lock which stays "in lock" on a timescale of 12 h+. The resonance of the previous generation transfer cavity was tuned with a piezo tube which had a limited tuning range. In the course of several hours, the piezo would reach the maximal elongation and no more tuning would be possible - accordingly the laser fell out of lock. The new transfer cavity built is tuned by thermal expansion by which we obtained a much higher tuning range. During several weeks of operation, no "un-locking" of the laser was observed. A 16 h long term frequency measurement recorded with a HighFinesse WS/7 wavemeter is shown in figure 3.8. The laser frequency stayed within ± 10 MHz of the set frequency at $\nu = 384.1950000$ THz, with a standard deviation of 1.8 MHz, while the mean of the recorded signal was 8 kHz below the set frequency. The frequency stability reached fits the desired needs.

Note: The wavemeter has a specified accuracy of 60 MHz [19] assuming recent calibration. We observe drifts on the order or ± 20 MHz per day from measurements of the frequency comb resonance.

3.2.5 Discussion

One of the main reasons to exchange the second generation transfer cavity was the limited frequency tuning range of the piezo electric tube. As a result, repeated re-locking of the laser during a measurement was needed. The new third generation transfer cavity is actively temperature controlled and lifts the limitations of the piezo electric tube. We did not observe an un-locking of the laser during several weeks of operations. A 16 h measurement showed a standard deviation of the laser frequency from the set point of 1.8 Mhz which has a negligible effect on our experiments, where the laser is detuned by terahertz from atomic resonance. The stable lock increases the stability of the experiment and reduces the time needed to prepare measurements significantly.

The cavity temperature controller opens up the option of always re-locking the laser to the same cavity resonance, as we can set a certain temperature offset to hold the temperature of the cavity at approximately the same level, even if the error signal from the wavemeter is switched off. This implies that temperature changes in the lab are low enough. We measure a cavity resonance frequency drift of about one FSR per 1.6 K, reliable re-locking to the same resonance therefore implies lab temperature changes below this

level.

The compact physical dimensions of the CTC and the temperature control on a software level largely simplified and compactified the electronics needed to control our transfer cavity setup. The CTC replaces the high voltage driver for the second generation transfer cavity piezo electric tube and the lock box used to control the piezo.

The CTC measures the temperature of the cavity at three positions. We see a mostly uniform temperature distribution, where the temperature at the center of the cavity is about $0.1 - 0.2$ K above the temperature at the sides, which was expected.

3.3 Pound-Drever-Hall lock

In this section we want to introduce the Pound-Drever-Hall (PDH) locking technique [8] which generates an error signal proportional to the frequency offset of a laser from an optical cavity resonance. The error signal is fed back to the laser to counteract the frequency offset. The cavity resonance in general shows a much better frequency stability than the laser, therefore the PDH frequency stabilization can be used to improve the frequency stability of an existing laser system. A closer look at the theory is given in appendix C, while we only want to present the results and implications on our measurements here.

The PDH error signal is given by (C.13)

$$V_e \propto \mathrm{Im}\left\{F(\nu)F^*(\nu+\nu') - F^*(\nu)F(\nu-\nu')\right\} \tag{3.15}$$

where $F(\nu)$ is the reflection coefficient of the cavity given by (A.18)

$$F(\nu) = \frac{g_{rt}(\nu) - R}{\sqrt{R}(1 - g_{rt}(\nu))} \tag{3.16}$$

The calculated PDH error signal is shown in figure C.3. The slope of the PDH error signal close to the cavity resonance frequency depends on the Finesse of the cavity and scales as $\propto F^{-2}$. As long as the quality of the PDH frequency stabilization is given by the signal to noise ratio of the electronics, which is in general the case, we can improve the lock quality by improving the Finesse.

The slope of the PDH error signal close to the cavity resonance frequency is difficult to measure, as a frequency scan over the cavity resonance yields

a noisy signal due to frequency fluctuations of the laser, which quickly scan the laser back and forth over the resonance. A measured PDH signal at resonance is shown in figure 3.9.

To circumvent the noise caused by laser fluctuations, we calculate the PDH slope at resonance from (3.15), using the measured mirror intensity reflection coefficient (2.13) and the measured FSR (2.6). We then only need to measure the peak-peak voltage V_e^{p-p} of the PDH error signal, which is nearly unaffected by the laser noise, to obtain the slope at resonance. We obtain a slope of

$$\begin{aligned} C_1 :\ s &= \frac{212}{V_e^{p-p}} \left(\frac{\text{kHz}}{\text{V}}\right) \\ C_2 :\ s &= \frac{230}{V_e^{p-p}} \left(\frac{\text{kHz}}{\text{V}}\right) \\ C_3 :\ s &= \frac{230}{V_e^{p-p}} \left(\frac{\text{kHz}}{\text{V}}\right) \end{aligned} \tag{3.17}$$

We measure $V_e^{p-p} = 92$ mV for all three generations of transfer cavities. We will later use the slope to estimate the laser linewidth, see section 3.5.

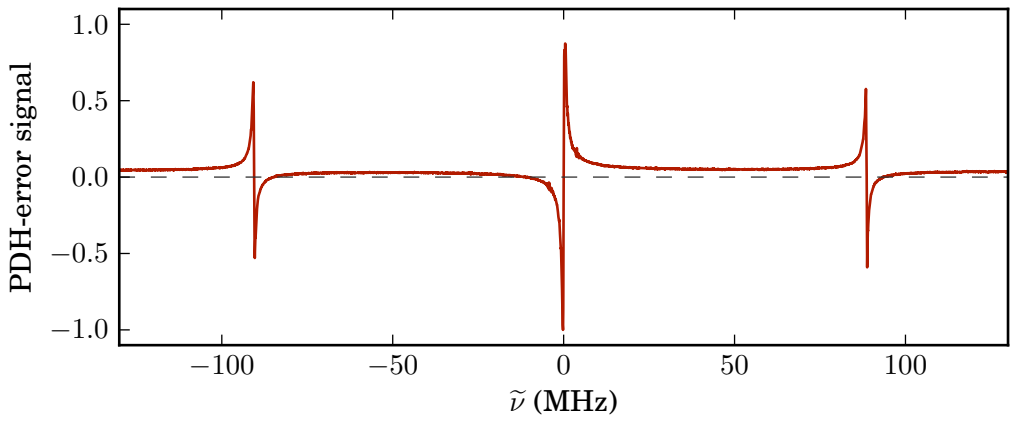

(a) The PDH error signal with the carrier and the sidebands at $\nu' = \pm 89.60$ MHz is shown. Residual DC components offset the signal slightly from zero.

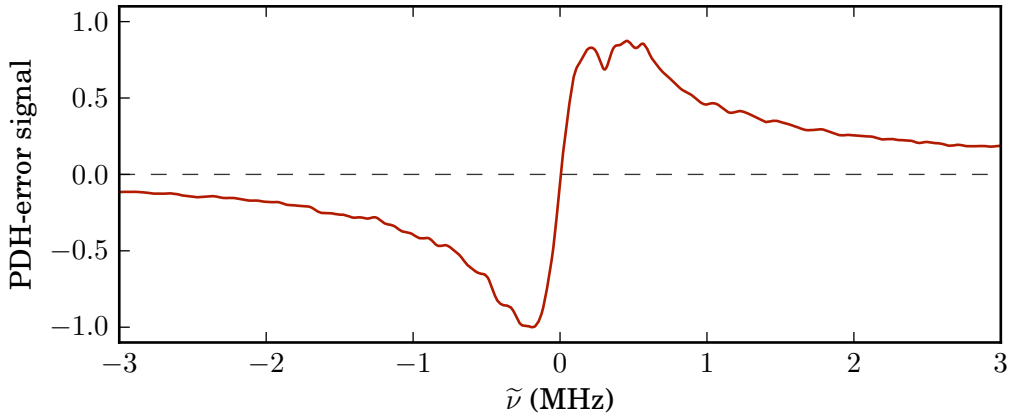

(b) This edge of the PDH error signal at the cavity resonance was used for the laser frequency feedback regulation. The noise on the signal resulting from laser frequency fluctuations is clearly visible.

Fig. 3.9: The measured PDH error signal of the first generation transfer cavity is exemplary shown, the amplitude was normalized to the maximum amplitude.

3.4 Measurement setup

To test and characterize the cavity and the electronics built, a measurement setup was assembled. This section will explain the setup in detail and serves as a guide to enable reproducibility of the measurements. The optics were placed on an optical table with active vibration isolation. The whole setup is shown in figure 3.10. We will discuss the optical and the electronic setup separately. We include details on the realization of a laser beam with a Gaussian mode profile and a stable amplitude and polarization. The electrical components used will also be explained in detail.

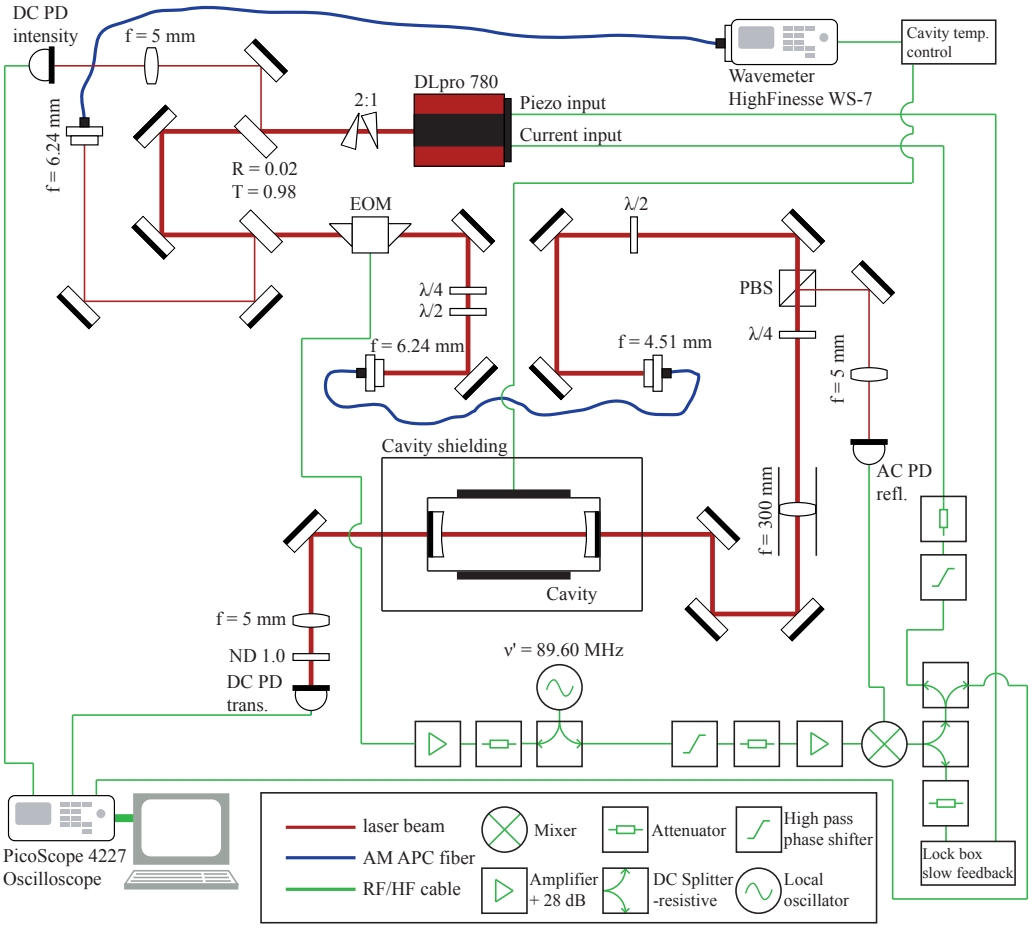

Fig. 3.10: The optical and electrical measurement setup is shown. The specified frequency range of the DC photo diodes (DC PD) is DC - 10 MHz and 0.5 - 500 MHz for the AC photo diode (AC PD)

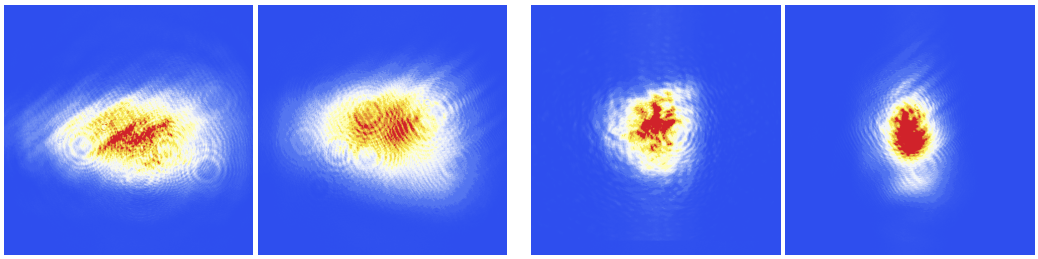

(a) Uncollimated beam at 10 cm (left) and 2 m (right) from the laser, the ellipticities are 1.79 and 1.46, respectively.

(b) Beam collimated with a 2:1 anamorphic prism pair at 10 cm (left) and 2 m (right) from the laser, the ellipticities are 0.96 and 0.70, respectively.

Fig. 3.11: Beam profile of the initially elliptical and the quasi-Gaussian laser beam close to the source and far away. Red color corresponds to regions of high intensity while blue color corresponds to regions of low intensity. The fringes and image distortions result from dust and dirt on the neutral density filter which was placed in the camera focus.

3.4.1 Optical setup

The laser source used was a Toptica DL pro 780 which was operated at a temperature T = 20.1°C and a diode current I = 48 mA with an output power of P = 6.6 mW. The laser beam profile was an elliptically distorted TEM_{00} mode, see figure 3.11a. We used an anamorphic prism pair with an aspect ratio of 2:1 to correct for the distortion and obtained a quasi-Gaussian field distribution, see figure 3.11b.

A beam splitter with a reflectivity of 2 % was used to direct some of the laser light to a DC-photo diode to monitor the laser intensity. Another identical beam splitter was used to direct light to a HighFinesse WS/7 wavemeter to monitor the wavelength of the laser. The wavemeter has a nominal frequency accuracy of 60 MHz [19], while the frequency precision is much higher and in the sub-MHz region.

The light was then directed through an EOM operated at $\nu' = 89.60$ MHz to create the sidebands needed for the PDH frequency stabilization. In the following, a polarization maintaining single mode fiber was used to obtain a purely Gaussian beam profile and to simulate the setup in the experiment. The EOM in front of the fiber turned the polarization of the laser beam to a partially circularly polarization which resulted in power oscillation from about $(50 - 100)$ % behind a polarization selective element after the fiber.

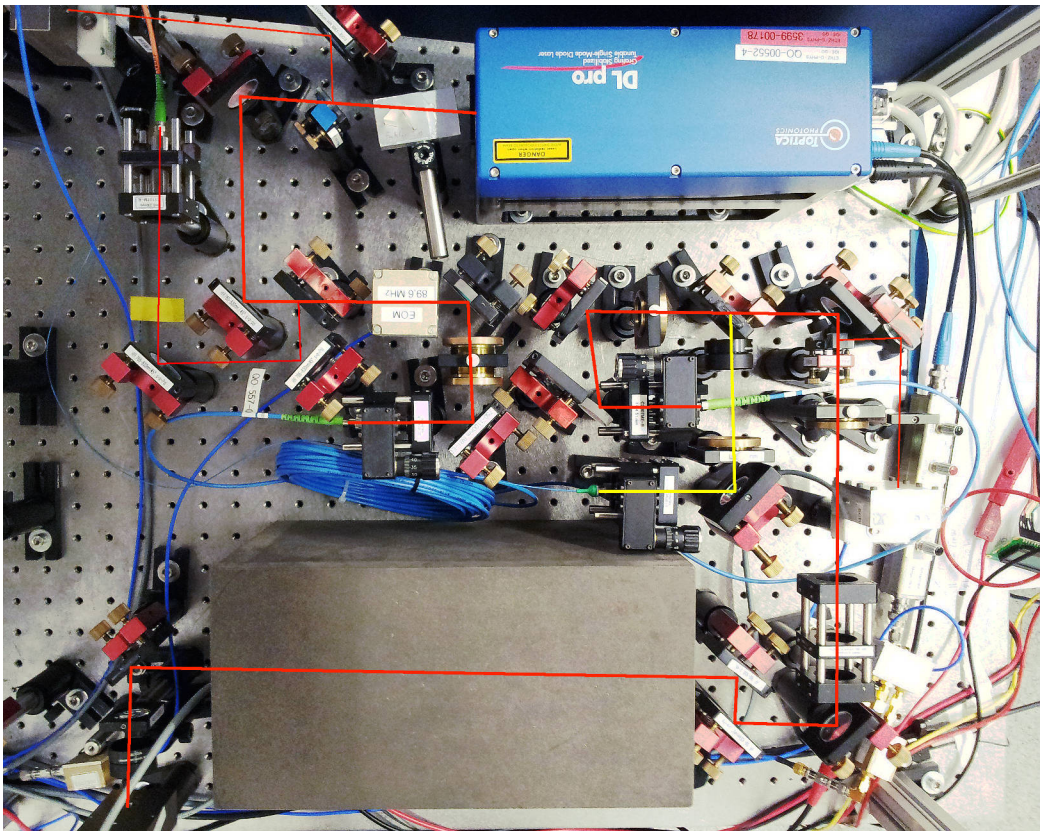

Fig. 3.12: The optical measurement setup is shown. The laser beam is shown in red. A 50:50 beam splitter directs parts of the beam into a fiber to another measurement, shown in yellow. This beam was not used in this setup and hence it is not shown in figure 3.10. The gray-brown box is the wooden cavity shielding and contains the optical cavity.

The period of the oscillation was about 20 min, strongly depending on the thermal and vibrational stability of the polarization maintaining fiber. To obtain a highly linearly polarized beam in front of the fiber, a $\lambda/4$ waveplate was used to suppress the circular polarization component and a $\lambda/2$ wave plate was used to turn the polarization axis to the polarization maintaining axis of the fiber. The optimization was done using a Schaefter + Kirchhoff SK010PA polarization analyzer and a circular polarization suppression of 99.5% was achieved.

Behind the fiber, another $\lambda/2$ waveplate was used to maximize transmission through the polarizing beam splitter (PBS). The $\lambda/4$ waveplate behind the PBS turns the polarization of the beam reflected back from the cavity by

2x45°, which reflects the cavity reflected beam to the AC-photo diode used to monitor the reflected power and to generate the PDH error signal.

The combination of a $f = 4.51$ mm fiber outcoupling lens and a $f = 300$ mm convex lens on a translation stage was used to optimally couple the beam into the cavity. The coupling was optimized by slightly varying the position of the collimation lens of the outcoupler at different positions of the convex lens to minimize higher order transverse modes in the cavity transmission spectrum of the cavity built. Due to the different mirror curvatures of the mirrors used in the previous transfer cavities ($R = 250$ mm) compared to the new transfer cavity ($R = 500$ mm), it was not possible to optimally couple into the first and second generation transfer cavities with this setup, which lead to more power in higher order transverse modes. This can be seen in figure 2.5. This effect was irrelevant to the measurements performed on these cavities for comparison to the new transfer cavity.

After coupling through the optical cavity, the transmitted beam was measured with a DC photo diode. A neutral density filter (ND) was used to keep the beam power within the measurement range of the photo diode of $(0 - 2)$ mW when experimenting at higher laser powers. The optical cavity was enclosed by a wooden box made from 20 mm MDF board lined with acoustic foam. The heavy MDF-box is used for thermal isolation as well as acoustic isolation. The acoustic foam added additional acoustic isolation. The wooden box is shown in figure 3.12.

3.4.2 Electronic setup

The cavity temperature controller (CTC) is described in detail in section 3.2. In this section, we want to focus on the electronics used in the PDH lock and the electronics used to characterize the cavity built. The RF frequency of $\nu' = 89.60$ MHz used in the PDH lock was generated with a home built local oscillator (LO). This signal was split with a resistive splitter. The branch directed to the left in figure 3.10 was amplified to 9 dBm at which the EOM is specified to create sidebands with an optical power of 4 % of the carrier power each. Throughout the setup, additional attenuators in front of the amplifiers, which have a fixed amplification of +28 dBm, were used to achieve the desired electrical power levels.

The branch directed to the right was directed to the PDH signal mixer. To optimize the mixer output signal, the LO signal was also amplified and an adjustable home built phase shifter was implemented to vary the relative

phase between the measured cavity reflection signal and the original LO signal.

The mixer output was split into three branches. One was directed to the home built *lock box* which generated the slow laser feedback (< 1 kHz) directed to the laser piezo. The second branch, the fast laser feedback (< 1 MHz), was phase shifted and attenuated and then directed directly to the current input of the laser. The cut-off frequencies of the slow and the fast feedback are visible in the error signal spectrum, see figure 3.16. A third branch was implemented to measure the unfiltered full-spectrum PDH error signal. This branch was needed as the PDH error signal output of the lock box is low-pass filtered with a cut-off frequency of about 10 kHz.

The photo diode signals and the PDH error signal were measured with a PicoScope 4227 oscilloscope which features up to 250 MSamples/s and a frequency range of DC -100 MHz [25]. The oscilloscope was connected to a computer via USB 2.0.

3.5 Laser lock characterization and laser linewidth

The linewidth of a laser is important from several perspectives. In spectroscopy it determines the resolution with which one can resolve resonances like e.g. hyper-fine energy levels of an atom. When exciting an atomic transition, we want the laser linewidth to be on the order of the atomic transition linewidth or smaller, as all off-resonant light will not take part in the transition.

To achieve a narrow linewidth laser one often locks the laser system to a frequency reference. A common locking-technique is the Pound-Drever-Hall lock which is described in section 3.3. The PDH technique is built on locking the laser to an optical cavity. To characterize the quality of the lock one can calculate the laser linewidth from an in-situ measurement of the cavity transmission or from the lock error signal, both signals are shown in figure 3.13. While the method of calculating the laser linewidth from the cavity transmission signal is only applicable for a cavity based lock, the method of determining the laser linewidth from the lock error signal is in principle applicable to any lock.
The methods described in this section represent a tool to measure the relative stability of the laser with respect to the cavity, while they are only partially sensitive to frequency fluctuations of the cavity. The only method

which can evaluate the absolute frequency stability of the complete system reliably would be a beat note measurement [26], preferable from beating the unknown laser with a spectrally very narrow reference laser, as noise correlations are intrinsically very low in this measurement. When such a reference laser system is not available, it is in general not possible to achieve a (reliable) final number for the laser linewidth. The required additional hardware for a beat note measurement was not available, but the in-situ measurement of the cavity transmission and the PDH error signal is quite convenient to implement and provides an estimate for the quality of the lock and a tool to compare different locks with respect to each other. It fit our needs very well.

The issue of measuring a laser linewidth turns out to be quite complex, as typical laser frequencies are in the hundreds of Terahertz, while state of the art electronics is able to measure tens of Gigahertz. The laser frequency is therefore not directly accessible, but there are several methods which measure the linewidth in an indirect way. The most common ones will be explained in more detail in the following sections. The underlying source of the line broadening of lasers is noise from various sources. A measurement of a laser linewidth is in that sense always also a noise measurement. The complexity of measuring linewidths therefore comes from the understanding and interpretation of the statistics of the measured noise. We therefore need as much information on the nature of the noise as possible and we have to account for noise correlations. In general, the noise will be correlated in some frequency regions, while it is uncorrelated in others. We have to be very precise in the interpretation of what we measure when we evaluate a certain noise signal.

In our PDH stabilized laser system, there are two main sources which contribute to the laser noise, the laser itself and the cavity the laser is locked to. Even if we had a laser with a perfectly delta peaked frequency spectrum which follows the resonance of the cavity, any noise in the cavity frequency spectrum will be transferred onto the laser frequency. Hence it is important to distinguish between the precision and accuracy of the laser, where the precision describes how narrow the frequency noise is spread around a certain frequency, while accuracy describes by how much this frequency changes in time. Accordingly, we have to quote the timescale on which we measure a linewidth. With the methods used in this chapter, we can only measure relative laser linewidths, while little information on the stability of the absolute laser frequency is obtained. An exception is the case where the cavity resonance is very stable. Then the measured relative laser linewidth will be approximately equal to the absolute laser linewidth.

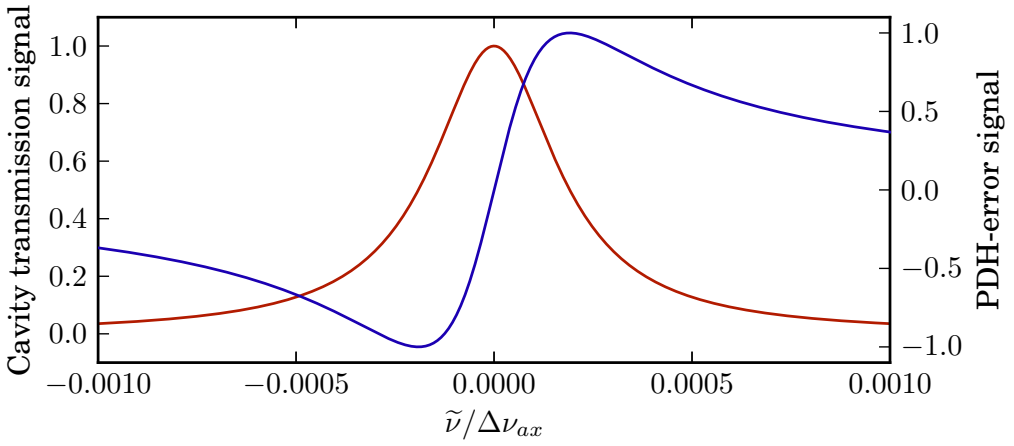

Fig. 3.13: The laser power transmitted through the cavity (red) and the PDH error signal (blue) are shown. Both signals are normalized to their peak value. The mirror reflectivity is $R = 99.88$ % which corresponds to the mirrors used in all three generations of transfer cavities.

From all these limitations, we see that we will not be able to quote a unique, final number for the laser linewidth, but we can compare the different transfer cavity systems with respect to each other and set certain limits on the laser linewidths. We now want to determine the laser linewidth of the laser locked to the transfer cavity. We will first use a direct method where we on the one hand calculate the frequency distribution of the laser from the PDH error signal, see figure 3.14, and on the other hand from the cavity transmission signal, see figure 3.15. Then we will use an indirect method where we calculate the spectral density S_ν of the laser from both these signals and then deduce an upper limit of the spectral density which corresponds to an upper limit of the laser linewidth, see figure 3.17 and 3.16. A discussion on the results follows after.

3.5.1 PDH error signal

We first take a look at the cavity reflection signal, more specifically at the PDH error signal which is derived from the cavity reflection signal, see section 3.3. Close to the cavity resonance, the PDH error signal is linear and we can linearly map the histogram of the PDH error signal noise to the laser frequency distribution. From a Gaussian fit of the histogram with the probability distributions

$$f(V_e) = C \times exp\left(-\frac{\Delta V_e^2}{2\,\tilde{\sigma}_l^2}\right) \tag{3.18}$$

$$f(\widetilde{\nu}) = C \times exp\left(-\ln(2)\,s^2 \frac{\widetilde{\nu}^2}{(\Gamma_l/2)^2}\right) \tag{3.19}$$

we get the laser linewidth Γ_l and the Gaussian standard deviation of the laser noise σ_l. Here we used that for a Gaussian distribution,

$$\Gamma = 2\sqrt{2\ln(2)}\,\sigma \tag{3.20}$$

The results obtained for the relative laser linewidth are shown in figure 3.14.

3.5.2 Cavity transmission signal

Next we want to determine the relative laser linewidth from the cavity transmission signal. If the laser is locked to the cavity resonance, the transmission through the cavity should be maximal. We know that the cavity transmission signal distribution with respect to the frequency has a Lorentzian profile, see (2.8) and figure 3.13. If we now measure the transmitted beam with a photo diode, frequency deviations of the laser will lead to power fluctuations on the photo diode. The measured voltage signal of the transmission photo diode can be connected to the laser frequency by

$$V_t(\widetilde{\nu}) = \frac{V_0}{1 + \left(\frac{\widetilde{\nu}}{\Gamma_c/2}\right)^2} \tag{3.21}$$

Here V_0 is the maximum photo diode voltage which corresponds to the voltage signal exactly on resonance with $V_t(\widetilde{\nu}) \leq V_0$. In section 3.5.1 we have seen that the PDH stabilized laser has a Gaussian frequency distribution. The laser with a Gaussian frequency distribution can therefore be written as

$$f(\widetilde{\nu}) = C \times exp\left(-\frac{\widetilde{\nu}^2}{2\,\sigma_l^2}\right) \tag{3.22}$$

where $f(\nu)$ is the frequency probability distribution, σ_l is the standard deviation of the laser frequency distribution and C is an arbitrary scaling constant. We can now derive the probability distribution for the measured transmission signal by inverting (3.21) and plugging the result into (3.22)

$$\widetilde{\nu} = \sqrt{\left(\frac{V_0}{V_t(\widetilde{\nu})} - 1\right)} \frac{\Gamma_c}{2} \tag{3.23}$$

$$\begin{aligned} f(V_t) &= C \times exp\left[-\frac{\widetilde{\nu}(V_t)^2}{2\,\sigma_l^2}\right] \\ &= C \times exp\left[-\frac{\Gamma_c^2}{8\,\sigma_l^2}\left(\frac{V_0}{V_t(\widetilde{\nu})} - 1\right)\right] \\ &= C \times exp\left[-\ln 2\,\frac{\Gamma_c^2}{\Gamma_l^2}\left(\frac{V_0}{V_0 + \Delta V_t(\widetilde{\nu})} - 1\right)\right] \end{aligned} \tag{3.24}$$

In the last step we used (3.20) and we introduced the transmission signal voltage deviation

$$\Delta V_t(\widetilde{\nu}) = V_t(\widetilde{\nu}) - V_0 \tag{3.25}$$

which will be the quantity that we actually measure. $\Delta V_t(\widetilde{\nu})$ corresponds to an oscilloscope measurement in AC mode and should only take negative values, since $\Delta V_t(\widetilde{\nu}$ represents the voltage deviations from the maximum voltage of the cavity transmission signal. To determine the width of the cavity resonance Γ_c, we scan the frequency over the cavity resonance and calibrate the frequency axis using the EOM-sidebands which appear at ν' as a reference. From a fit of (3.24) to the histogram of the transmission noise signal measured by the photo diode we obtain the relative laser linewidth Γ_l.

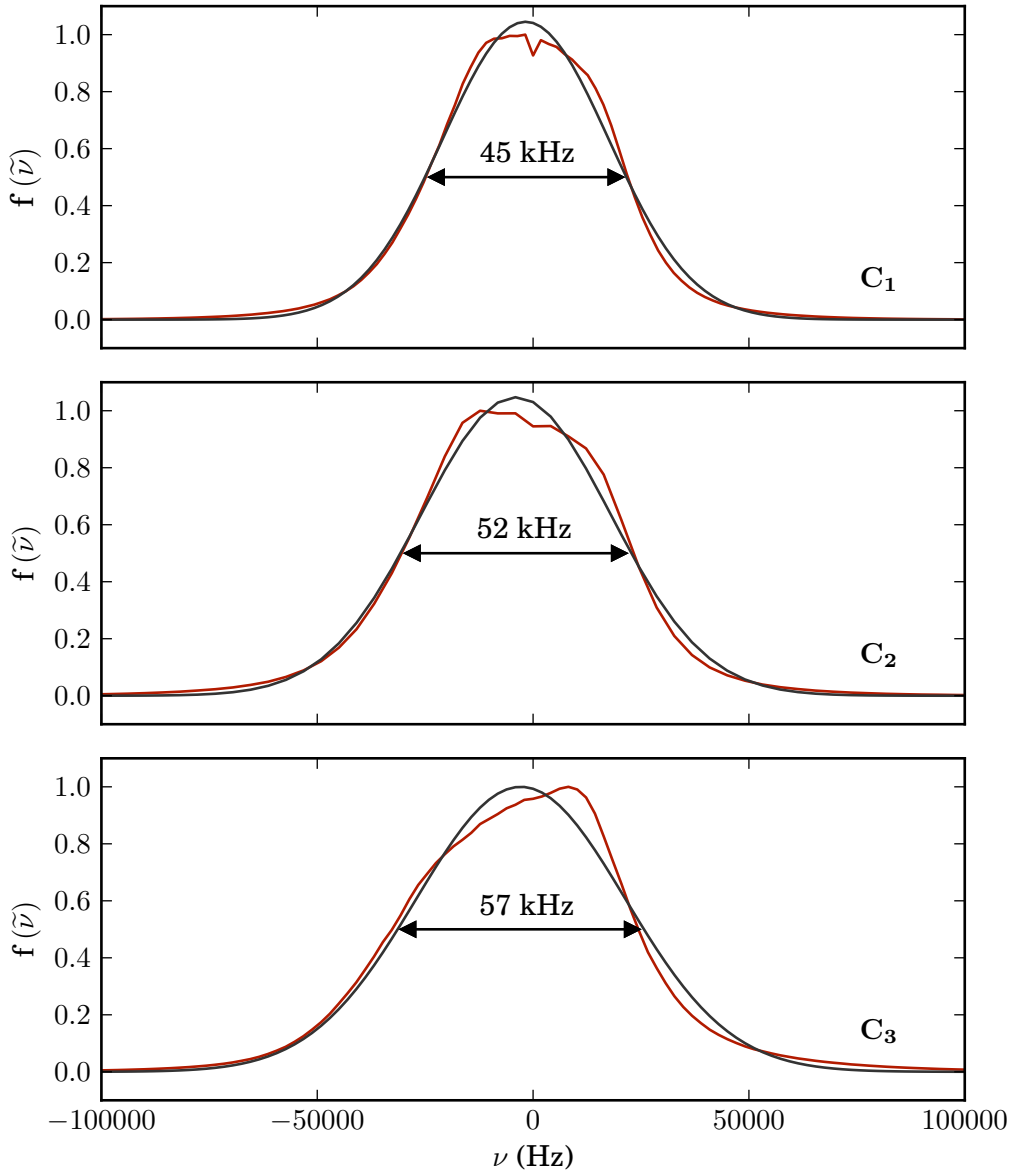

Fig. 3.14: Histogram of the PDH error signal fluctuations (red), an average of ten measurements is shown. The histogram is normalized to the highest value. Voltage deviations have been converted to frequency deviations using the PDH error signal slope. A Gaussian fit (black) yields laser linewidths of $\Gamma_l(C_1) = 45.2(3)$ kHz, $\Gamma_l(C_2) = 51.8(3)$ kHz and $\Gamma_l(C_3) = 57.1(5)$ kHz. The measurement time was 1 s.

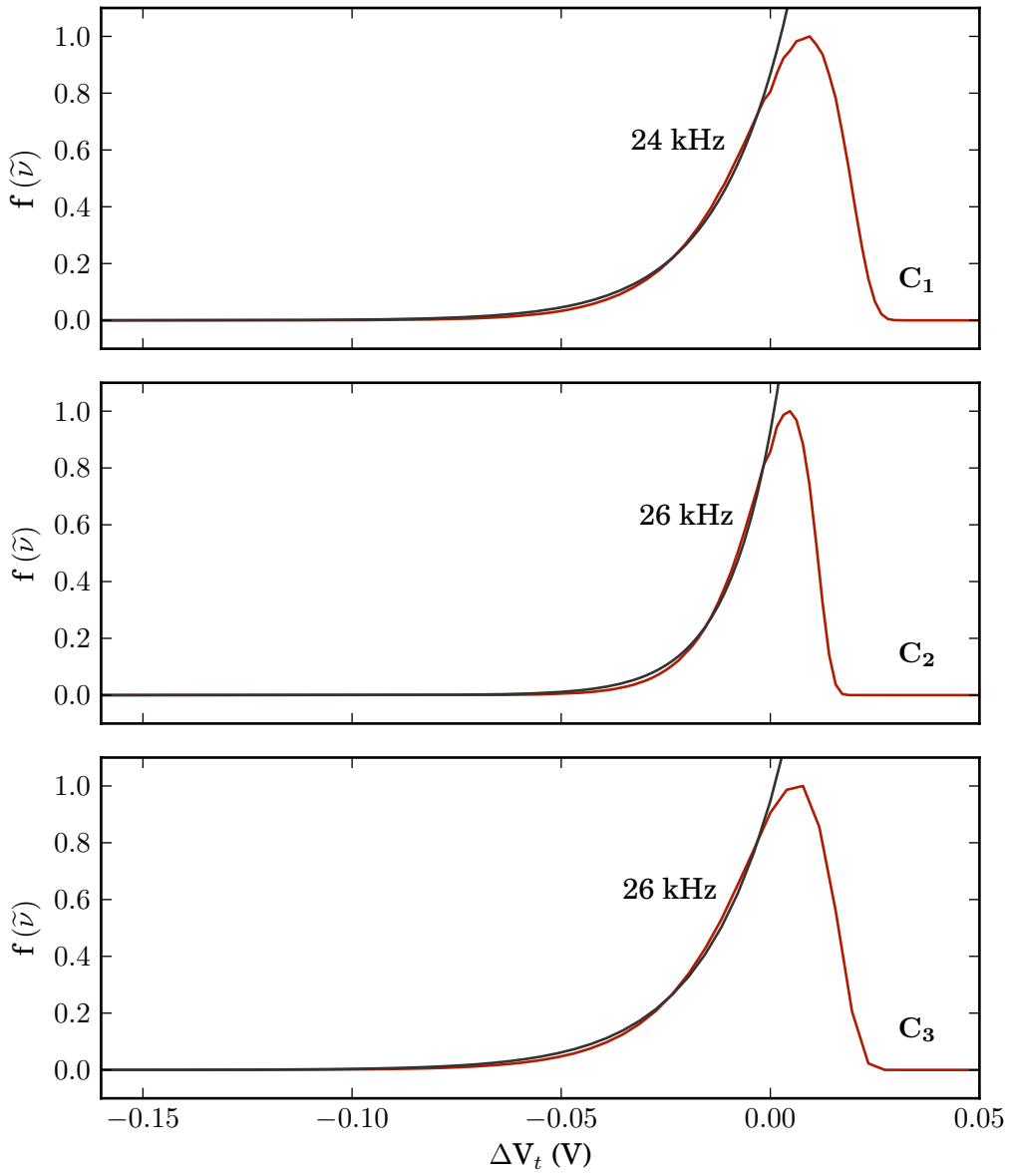

Fig. 3.15: Histogram of the cavity transmission signal fluctuations (red), an average of ten measurements is shown. The histogram is normalized to the highest value. A fit of (3.24) (black) to the voltage distribution for negative voltages ΔV_t yields laser linewidths of $\Gamma_l(C_1) = 24.2(1)$ kHz, $\Gamma_l(C_2) = 26.1(1)$ kHz and $\Gamma_l(C_3) = 25.7(1)$ kHz. Positive voltage values are assumed to come from additional noise of unknown origin. They are ignored as they would correspond to a transmission $V_t > V_t^{max}$. The measurement time was 1 s.

3.5.3 Spectral noise density

Another approach to determine the laser linewidth is based on determining upper limits of the cavity transmission and PDH error signal spectral noise density (SND) $S_{\widetilde{\nu}}(\nu)$. The SND is given by the square root of the one-sided power spectral density (PSD) as $S_{\widetilde{\nu}}(\nu) = \sqrt{S_{\widetilde{\nu}\widetilde{\nu}}(\nu)}$. From these limits on the SND we can calculate an upper bound for the laser linewidth [21]. Knowledge on the SND is in so far favorable as we can identify the frequency regions which show the highest noise levels. This knowledge was used to improve the stability of the system.

In the case of the PDH error signal voltage noise can be converted to frequency noise with (3.17). We get

$$\widetilde{\nu}(t) = s\Delta V_e(t) \tag{3.26}$$

To evaluate the cavity transmission signal, we first need to convert the measured voltage noise to frequency noise through the cavity transmission function, compare (3.23)

$$\widetilde{\nu}(t) = \sqrt{\left(\frac{V_0}{V_0 + \Delta V_t(t)} - 1\right)} \frac{\Gamma_c}{2} \tag{3.27}$$

where $\Delta V_t(t)$ is again given by the AC voltage deviations of the measured voltage signal, compare (3.25). Performing a discrete fast-Fourier transform (DFFT) on the data obtained from (3.26) and (3.27) yields the SND. To be able to derive limits on the laser linewidth from the SND we need not only qualitative but quantitative results of the SND. To this reason, we want to take a closer look at the normalization of the DFFT.

DFFT: From the amplitude signal in time space one can calculate the spectrum in frequency space using a DFFT. The maximum frequency is given by the sampling rate of the measurement in time space, i.e. $f_{max} = 1/dt$. The total measurement time determines the frequency resolution which is given by $df = 1/T$, the frequency range is therefore $1/T$ - $1/dt$.

Due to technical reasons, the sampling rate should always be at least 2.5x the frequency to measure. If higher frequencies are present, these need to be cut by a low pass before digitization to prevent aliasing effects. Aliasing happens if the frequency to measure is higher than 2x the maximum measurement frequency, the measured frequency will then be mirrored at the

maximum frequency. For e.g. 1000 Hz sampling rate, the maximum measured frequency is 500 Hz. If we now try to measure 730 Hz, this frequency would appear as 270 Hz after digitization.

The Fourier transform of noise in general diverges, as the noise extends over the whole frequency range. We can think of the noise as a random walk process, where the variance $\langle \nu^2 \rangle$ scales as the number of steps, which in our case equals the total measurement time T. Accordingly, $\sqrt{\langle \nu^2 \rangle}$ scales as $\sqrt{T}$ and we introduce the "windowed" Fourier transform [27]

$$V_T(\nu) = \frac{1}{\sqrt{T}} \int_{-T/2}^{T/2} dt \, \mathrm{e}^{i2\pi\nu t} V(t) \tag{3.28}$$

which avoids the divergence of the integral. The unit of the windowed Fourier transform of a voltage signal then is $\mathrm{V}/\sqrt{\mathrm{Hz}}$. The two-sided power spectral density (PSD) is given by [27]

$$S^{(2)}_{VV}(\nu) = \lim_{T\to\infty} \left\langle |V_T(\nu)|^2 \right\rangle = \lim_{T\to\infty} \langle V_T(\nu) V_T(-\nu) \rangle \tag{3.29}$$

where we used that $V_T(\nu)$ is symmetric in frequency space, $V_T(\nu) = V_T(-\nu)$. The two-sided PSD is also symmetric in frequency space, $S^{(2)}_{VV}(\nu) = S^{(2)}_{VV}(-\nu)$. Subsequently, we now define the one-sided spectral noise density, where we assume uncorrelated noise, as

$$S^{(1)}_{VV}(\nu) = \lim_{T\to\infty} 2| \langle V_T(\nu) \rangle |^2 \qquad \text{with} \qquad \nu > 0 \tag{3.30}$$

So far we assumed $V_T(t)$ to be continuous. When measuring a noise signal, we can only measure a finite amount of N discrete values of $V_T(t) \to V(t_n)$. We will therefore in the next step change from an integral over t to a sum of discrete values. To get to the spectral noise density, we take the square root of the one-sided power spectral density, $S^{(1)}_V(\nu) = \sqrt{S^{(1)}_{VV}(\nu)}$, which is now given by

$$S^{(1)}_V(\nu) = \sqrt{\frac{2}{T}} \frac{1}{N} \sum_{n=0}^{N-1} \mathrm{e}^{i2\pi t_n \nu/T} |V(t_n)| \tag{3.31}$$

with the total measurement time T and a measurement of N data points. With the appropriate transformations between the measured voltage $V(t)$ and $\widetilde{\nu}(t)$ (3.26) and (3.27) we now obtain the (one-sided) spectral noise density $S_{\widetilde{\nu}}(\nu)$.

Finally, we have to calibrate the SND that we obtained from the PDH error signal to gain the correct result. So far we only took into account the linear region of the PDH error signal at the cavity resonance, see figure 3.13. At noise frequencies above the cavity linewidth Γ_c, a 10-dB/decade roll-off in the SND is expected, which corresponds to a 20-db/decade roll-off in the power spectral density (PSD) [21]. We therefore calibrate the SND with the factor

$$\sqrt{1 + \left(\frac{\widetilde{\nu}}{\Gamma_c}\right)^2} \tag{3.32}$$

No further calibration is needed for the transmission signal as (3.27) already takes into account the full shape of the transmission signal.

To be able to determine an upper bound of the laser linewidth from the SND we need to link the two. This has been done in [22] and [28]. For Gaussian distributed white noise which is low pass filtered with a cut-off frequency $\nu_c >> S_{\widetilde{\nu}}(\nu)$ there exists, after elaborate derivations, the simple solution

$$\Gamma_l = \pi \left[S_{\widetilde{\nu}}(\nu)\right]^2 \tag{3.33}$$

Γ_l is the full width at half maximum laser linewidth, where we took care of the appropriate normalizations and definitions of the SND and the linewidth. The results for the SND of the three generations of transfer cavities are shown in figure 3.16 and 3.17.

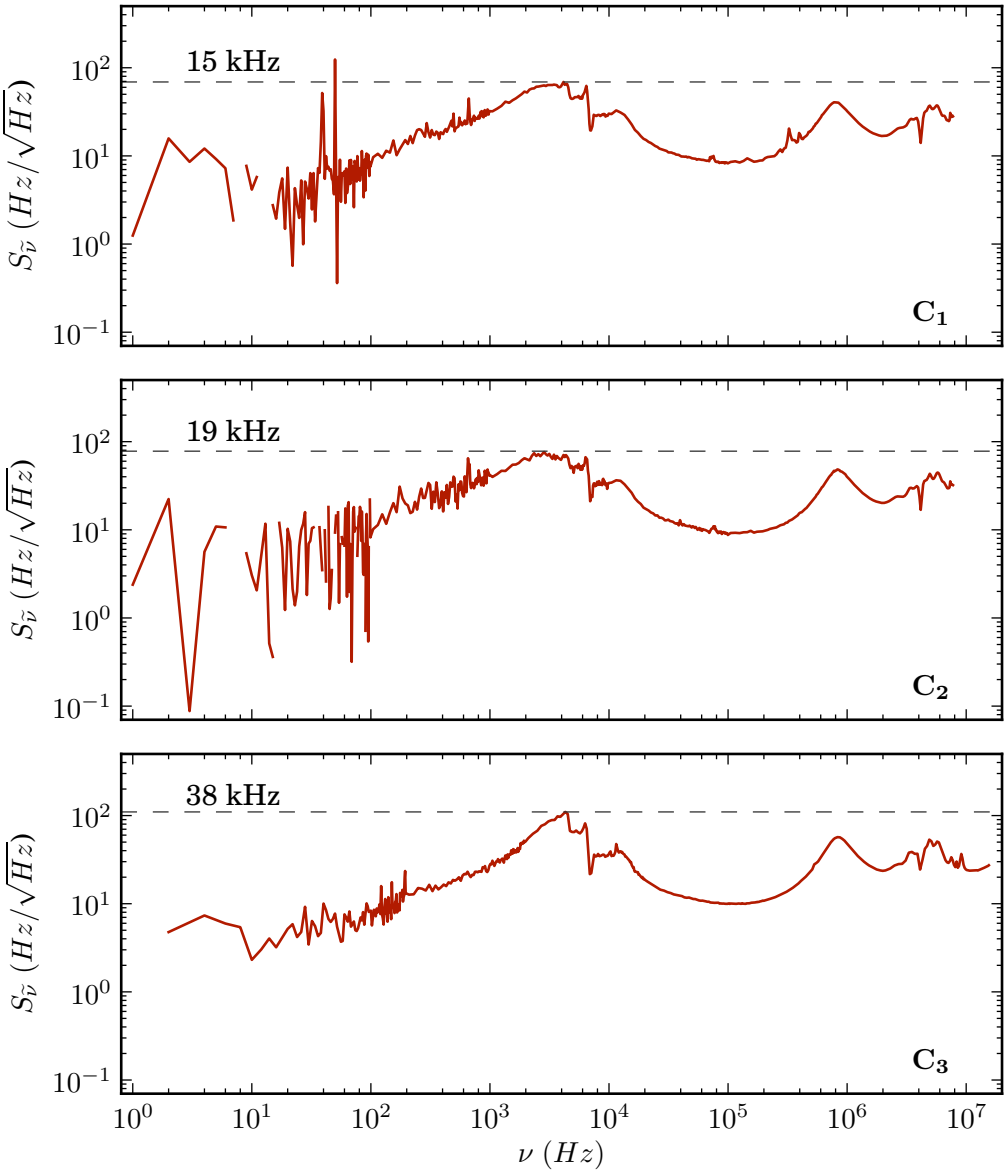

Fig. 3.16: Spectral density of the PDH error signal fluctuations (red), a background measurement with the laser switched off was subtracted. An average of ten measurements is shown. A Gaussian distributed white noise level is shown (gray) which corresponds to an upper bound of the laser linewidth Γ_l. The enhancement at the AC-line frequency of 50 Hz of C_1 is ignored. The measurement time was 1 s.

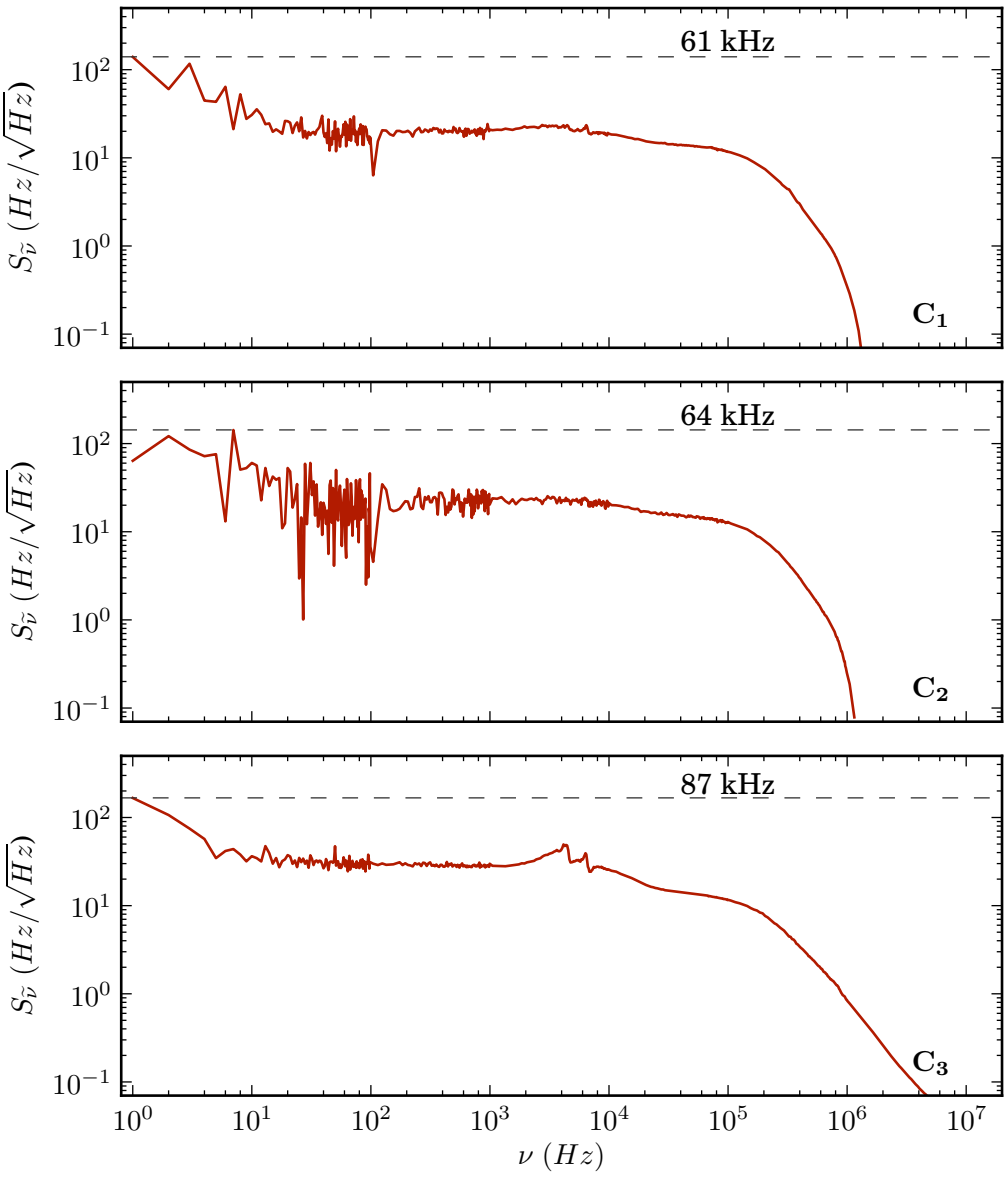

Fig. 3.17: Spectral density of the cavity transmission signal fluctuations (red), a background measurement with the laser switched off was subtracted. An average of ten measurements is shown. A Gaussian distributed white noise level is shown (gray) which corresponds to an upper bound of the laser linewidth Γ_l. The enhancement at low frequencies is ignored as it is a result of vibrations on the laser table due to the measurement procedure. The measurement time was 1 s.

3.5.4 Laser beat note

We now want to take a look at the beat-note laser linewidth measurement as well, because it is the standard method and the best technique known to measure the linewidth of a laser [26]. We *beat* the unknown laser with another laser of approximately the same frequency. Their beams are overlapped and are measured with a photo diode, which measures the squared amplitude of the incoming beams

$$P \propto |E_1(\nu_1) + E_2(\nu_2)|^2 \tag{3.34}$$

The resulting signal will contain terms which are proportional to the sum and the difference of ν_1 and ν_2, see (C.7), (C.8), (C.9), (C.10). All terms oscillating at ν_1, ν_2 or higher frequencies are not accessible to direct measurement and can be filtered by a low-pass filter, but for lasers with approximately the same frequency, $\nu_1 - \nu_2$ is directly measurable. In general $E_1(\nu_1)$ and $E_2(\nu_2)$ will not be delta-peaked at ν_1 and ν_2 but they will both have an unknown resonance linewidth. The beat-note constitutes the convolution of these resonances and the distinct linewidths can not be distinguished.

There are, however, several cases where it is possible to distinguish the resonances and linewidths of the two beams.

- In the limiting case where one of the two beams has a much smaller resonance linewidth than the other one we can describe the narrow resonance by a delta-peak. We can then scan the delta-peaked beam over the resonance of the unknown beam and directly resolve the resonance and linewidth. Although this approach is straight forward in the implementation, we would need a laser at the same frequency with a much narrower linewidth than the one of the unknown laser.

- Another method is to calculate the linewidth of the unknown laser from the resonance width of the convoluted beat-not signal. To be able to deconvolve the beat-note we need a laser at the same frequency as the unknown one with a known resonance linewidth and lineshape.

- One can beat an unknown laser with itself using a *self-heterodyne* technique [29]. In this approach the laser beam is split by a 50:50 beam splitter and one optical path is delayed by sending the light through a long fiber of several kilometers length. Then a beat-note is created by the unknown laser and an earlier version of itself, shifted in time.

A deconvolution of the beat-note is possible as both beams have the same underlying lineshape. This approach can only measure noise that occurs on a timescale shorter than the time delay created by the fiber c/L, where c is the speed of light in the fiber and L is the length of the fiber. Noise occurring on larger timescales will be correlated and can not be measured. Although this approach is quite straight forward in the implementation, one needs a fiber of several kilometers of length, also this method is sensitive to noise created by the fiber.

- An approach that can be used for unknown reference laser systems which have a narrower linewidth than all other systems available is the beating of two identical systems with each other. As with the self-heterodyne technique, a deconvolution of the beat-note is possible as both beams should have the same underlying lineshape. The obvious drawback is the need of two identical systems, in addition noise which is correlated between the two laser systems can not be measured [26].

The lineshape of a laser is usually well described by a convolution of a Gaussian and a Lorentzian frequency distribution, the resulting distribution is called Voigt profile. The Lorentzian frequency distribution is predicted by elementary laser theory [9] while the Gaussian contribution originates mainly from electronic noise. To deconvolve the beat-note created from two identical lasers or by a self-heterodyne technique we need to know if the underlying resonance lineshape is rather Gaussian or rather Lorentzian. For a Gaussian lineshape the width of the beat-note resonance is

$$\Gamma_{beat}^2 = \Gamma_1^2 + \Gamma_2^2 = 2\,\Gamma_l^2 \tag{3.35}$$

and we can calculate the linewidth of the unknown laser to

$$\Gamma_l = \frac{1}{\sqrt{2}}\Gamma_{beat} \tag{3.36}$$

For a Lorentzian lineshape the width of the beat-note resonance is

$$\Gamma_{beat} = \Gamma_1 + \Gamma_2 = 2\Gamma_l \tag{3.37}$$

and we can calculate the linewidth of the unknown laser to

$$\Gamma_l = \frac{1}{2}\Gamma_{beat} \tag{3.38}$$

3.5.5 Discussion

We have shown four different methods to characterize the linewidth of a PDH stabilized laser for the three generations of transfer cavities, using two data sets each. We see that the results obtained by the different methods differ from each other, while the linewidths of the three generations of transfer cavities are roughly consistent within one method of analysis.

The four methods each have their strengths and weaknesses:

- The derivation of the laser linewidth from the PDH error signal is straight forward. Yet, the results do not represent the complete laser linewidth but a relative linewidth. They are a measure for how well the PDH lock stabilizes the laser frequency to the cavity resonance, but fluctuations in the cavity resonance frequency are only partially measured. This method averages the noise over all spectral components and can resolve noise at high frequencies.

- As with the derivation of the linewidth from the PDH error signal, the derivation of linewidth from the cavity transmission signal is relatively straight forward, yet again the results for the laser linewidth are not intrinsically accurate. The measured linewidth again represents a relative linewidth. As the PDH error signal analysis, this method averages the noise over all spectral components, while it can only resolve noise up to the cut-off frequency. It showed the highest level of consistency of all methods during our experiments.

- The spectral noise density from both these measurements highlights the regions where the noise is most prominent. Although this method is also not guaranteed to be accurate in the final results of the laser linewidth and it only yields an upper limit for the relative laser linewidth, it has the advantage of working with frequency resolved data. It can therefore be used as a frequency resolved comparison tool for different measurements and different systems with respect to each other. There, the strengths and weaknesses of different laser stabilization approaches can be analyzed in specific frequency regions, see e.g. figure 2.12.

In this context, we need to explain what the relative linewidth that we measure represents. In a first step, we see that the higher the Finesse, the steeper the slope of the PDH error signal, and thus the higher the gain of the lock. Therefore, the lock can counter-act small frequency deviations more easily. We find that the PDH slope $s \propto F$ and accordingly, the spectral density $S_{\widetilde{\nu}} \propto F^{-1}$. The relative laser linewidth therefore depends on $\Gamma_l \propto F^{-2}$. Laser systems with a very narrow relative linewidth can be achieved by PDH

systems based on very high Finesse cavities, see e.g. [21]. The absolute frequency accuracy then strongly depends on the mechanical stability of the cavity used and has to be measured with a beat note.

A very narrow relative linewidth can be thought of as a delta-peaked resonance fluctuating from the noise added by the cavity. If the Finesse is not too high as in our system, then the laser will not always be able to follow the movement of the cavity and the noise of the cavity will be partially present in the PDH error and the cavity transmission signal. The measured linewidth is then closer to the absolute linewidth of the system.

In this context, it is important to focus on the purpose of the transfer cavity built. We want to achieve a high relative frequency stability between the 780 - 785 nm probe laser and the resonance of the science cavity in the experiment. The frequency noise levels of the second generation transfer cavity were already on an acceptable level for our measurements in the experiment. With the third generation transfer cavity being on a comparable level, we are not limited by the cavity-noise and probe laser noise in our experiment.

We conclude that the short term frequency stability of the three generations of transfer cavities is approximately comparable, with a final relative linewidth in the tens of kilohertz for a measurement time of 1 s. The long term stability of the third generation transfer cavity, on the other hand, is vastly improved due to the elimination of thermal drifts. These results should enable the implementation of a 3D optical lattice potential in our experiment.

4. IMPLEMENTATION OF THE CAVITY IN THE CURRENT EXPERIMENT SETUP

In the experiment, the transfer cavity is used to indirectly lock the $780 - 785$ nm probe laser to the science cavity. In a first step, both the probe laser and a transfer laser at 830 nm are locked via PDH to the transfer cavity. The cavity length is stabilized against slow drifts via the temperature lock using a wavemeter to produce the error signal. In a final step, the science cavity is frequency stabilized via PDH to the the 830 nm laser, which is far detuned from any resonance of the ^{87}Rb atoms used. By implementing this locking chain, both the probe laser and the 830 nm transfer laser can simultaneously be resonant with the science cavity. The locking chain is shown in figure 4.1. The science cavity is piezo tuned, it can therefore follow frequency fluctuations of the probe laser on the kilohertz level and below, while noise of higher frequencies is unaffected.
s In a final step, the second generation transfer cavity was exchanged against the third generation. In the course of this exchange, we also switched the old aluminum cavity mount to a cavity mount with a Teflon post to decrease the mechanical coupling of the cavity to the optical table, see figure 2.4. The required adjustments in the optical setup were taken into account in the design of the third generation transfer cavity from the start. We could therefore mostly keep the current optical setup in the experiment unaltered. To optimize the mode matching of the new cavity, which was built from mirrors of different curvature, we had to exchange the fiber outcoupling lenses from Thorlabs LT110P-B with a focal length of $f = 6.24$ mm to Thorlabs LT230P-B with a focal length of $f = 4.5$ mm.

Throughout the course of several weeks of operation, the third generation transfer cavity showed a stable locking performance and no signs of additional noise in the experiment.

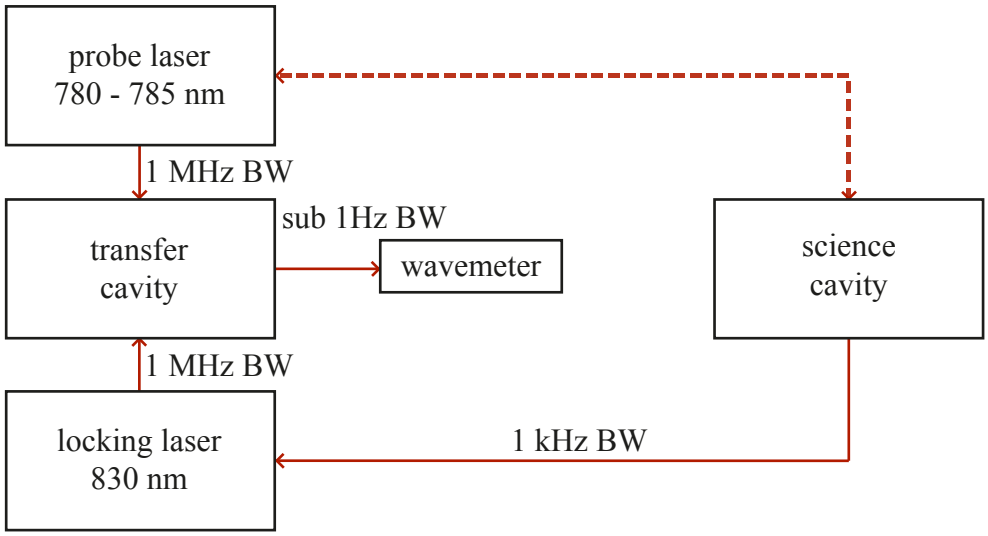

Fig. 4.1: The implementation of the locking chain is shown. The science cavity is indirectly locked to the probe laser via an additional off-resonant laser to be able to achieve locking without perturbing the ^{87}Rb atoms in the science cavity by almost resonant 780 nm light. The transfer cavity is locked to the wavemeter, which generates an error signal based on the frequency deviation of the probe laser transmitted through the cavity from a set frequency.

5. CONCLUSION AND OUTLOOK

We have presented a new design for a temperature-tuned optical transfer cavity. The new transfer cavity was successfully tested and implemented in the ultra-cold atomic ^{87}Rb cloud experiment, where it is used to indirectly lock the $780 - 785$ nm probe laser to the optical high Finesse science cavity. The experimental results are summarized in the following:

- The assembled cavity shows a very low coefficient of thermal expansion of $\alpha_T = 1.7 \times 10^{-6}$ K^{-1}, which is more than an order of magnitude below the coefficient of thermal expansion of aluminum and the glues used. We accordingly conclude that we successfully canceled undesired thermal expansion of the cavity along the optical axis, the remaining thermal expansion is desired and used to tune the resonance of the cavity. We obtained a sensitivity to temperature change of the cavity resonance frequency of 1 GHz per 1.6 K.

- The relative linewidth of the 780 nm laser locked to the cavity was evaluated to several tens of kilohertz. We have seen a performance comparable to the previous generations of the transfer cavity. The mechanical stability of the cavity was improved by exchanging the post which the cavity is placed on from aluminum to Teflon, the net effect is a 25% reduction in the relative laser linewidth.

- A new slow lock electronic for the cavity temperature lock was developed and implemented. The laser stayed locked throughout several weeks of operation. A 16 h frequency measurement with a wavemeter showed a standard deviation of 1.8 MHz from the set frequency, while the laser frequency stayed continuously within 10 MHz to the set frequency. The improved locking stability opens up the opportunity of long, uninterrupted measurements on the experiment.

- We could implement the new transfer cavity into the experiment keeping the optical setup largely unaltered. By only exchanging the fiber outcoupling lenses, the higher order mode suppression relative to the fundamental TEM_{00} mode was improved from 80 to > 250.

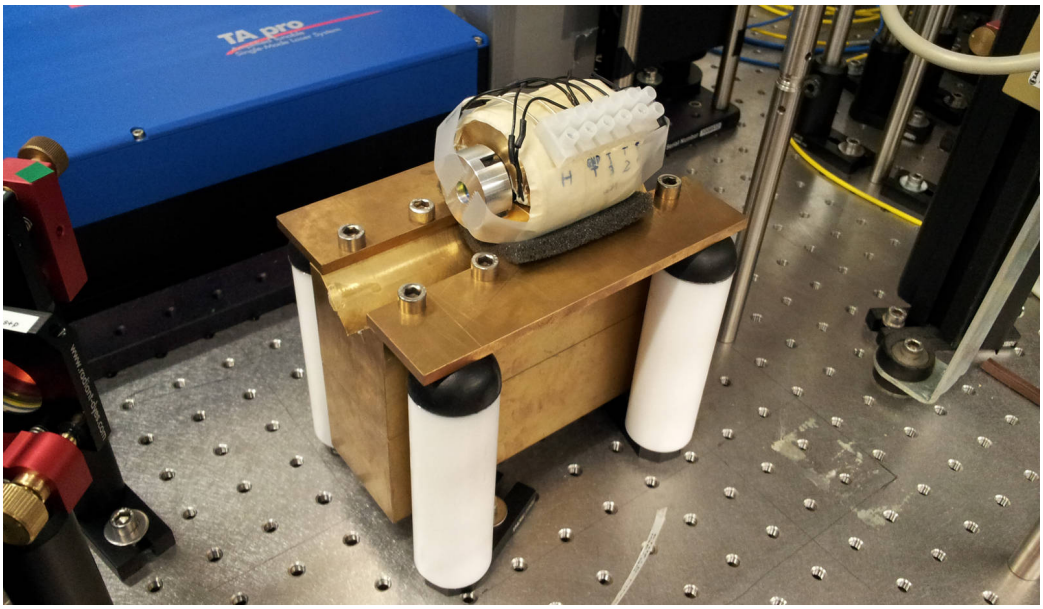

Fig. 5.1: The cavity used to narrow the linewidth of the 670 nm lattice laser is shown. It is of the same design as the third generation transfer cavity, but shorter and with an order of magnitude higher Finesse. Based on the mechanical noise characterization presented in this work, the cavity mount was redesigned for higher vibrational damping. The mount rests on Sorbothane absorbers which are placed on four Teflon posts.

During the process of writing up, an optical lattice potential obtained from a 670 nm laser was implemented in the experiment. This lattice will be used to reduce the dimensionality of our BEC to two-dimensional layers or one-dimensional tubes. For deep lattices, this will also increase the importance of short-range interactions. To lower the heating rate of the atoms in the lattice potential, the lattice laser will be narrowed down by locking it to a cavity. The cavity features the same design as the third generation transfer cavity, see figure 5.1. With the PDH-lock of the lattice laser in place, we are finishing the final step towards introducing an optical lattice in our quantum simulator system.

ACKNOWLEDGMENTS

This thesis would not have been possible without the support of many people:
I want to thank, on an equal footing, Tilman Esslinger from the ETH Zurich for giving me the opportunity to carry out exciting research in his group, and Thorsten Schumm from the TU Vienna for his great support of my work, and both for their inspiring enthusiasm for the world of physics. I also want to thank Renate Landig and Tobias Donner for proof-reading this thesis, as well as the rest of the group. They shared their vast experience in theory and experiment with me, which came in handy more than once.

Most important of all, I want to thank my family, and in particular my parents Eva Maria and Richard for enabling me to attend university, and for their support in all sorts of ways throughout the time of my studies. None of this work would have been possible without them.

I would also like to thank my fellow students and friends for the many elaborate discussions, wonderful teamwork and a great time. Specifically I want to thank (in no particular order) Tobias, Bernhard, Ali, Martin, Michael, Lukas, Andreas and Daniel.

Finally I want to thank my great love Thekla for being there for me and for her kindness and appreciation. To all that I might have mistakenly omitted: thank you!

"Now this is not the end. It is not even the beginning of the end.
But it is, perhaps, the end of the beginning." - Winston Churchill

Appendices

Appendix A

GENERAL THEORY ON OPTICAL CAVITIES

There exists a huge amount of literature that deals with optical cavities, see e.g. [9, 10, 11]. Unfortunately, the literature is often not very consistent in the nomenclature and description of the effects involved. Furthermore, most authors present the theory in an either very compact form focusing on the end results, or in a very general and exhaustive form that can overwhelm the uneducated reader. We therefore decided to include a review of the general theory on many of the most important properties needed to describe and understand the working principle of a cavity. We try to present the theory in a (mostly) closed form with consistent nomenclature, where a special focus lies on the description of simple two-mirror linear cavities. For more exotic types and further theory on cavities see e.g. [9]. We hope to offer readers who are new to this field of physics a convenient and informative introduction. The equations derived in this chapter were used throughout this work and are referenced where appropriate.

A.1 The light field in the cavity

If and only if the wavelength of an incident beam is an integer multiple of twice the optical length of a cavity, constructive interference will occur, for all other cases the beam will be damped by destructive interference. This can be shown in purely classical model. In the following derivation we follow [10, 9]. The process is shown in figure A.1, the parameters and properties used are defined in table A.1.

For the description of many effects involved in the description of the cavity or light field it is important to take the phase of the laser field into account, we therefore work with the complex electric field amplitude $E(x, y, z)$ of the field.

To describe macroscopic effects like the absorption by a medium, it is

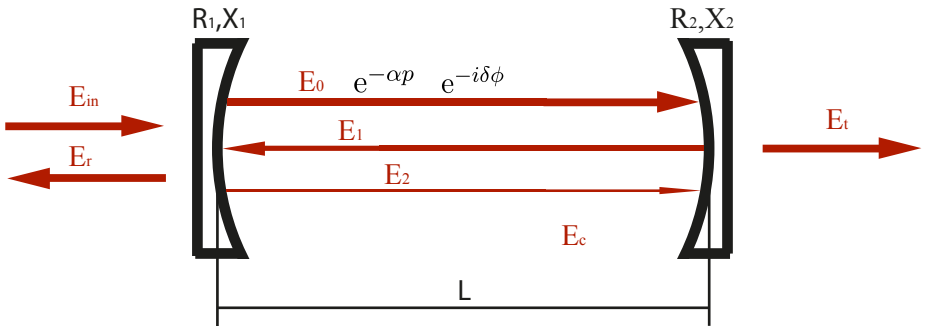

Fig. A.1: The electric field in the cavity is shown. For a definition of the quantities shown, see table A.1. $e^{-i\delta\phi}$ is the phase shift of the beam per round trip and $e^{-\alpha p}$ accounts for internal absorption and scattering losses.

ν	laser frequency
p	round trip length, p is two times the length for a linear cavity
α	loss coefficient of the cavity, taking into account internal absorption and scattering
n	refractive index, for a gaseous medium it depends on various external properties like temperature, pressure or humidity
c	speed of light in a medium, which is given by $\frac{c_0}{n}$ where c_0 is the speed of light in vacuum
E_{in}	the electric field of the incoming beam
E_t	the electric field of the transmitted beam
E_r	the electric field of the reflected beam
E_c	the total electric field inside the cavity
E_j	complex field amplitude of the j-th round trip
I	field intensity
P	field power
g_{rt}	loss parameter of round trip gain
T, R, X	mirror intensity transmission, reflection and absorption coefficient respectively, which are connected to the amplitude coefficients by $T = t^2$, $R = r^2$ and $X = x^2$
F	Finesse, measures "the quality of a cavity" [10] or "the resolving power" [9]

Tab. A.1: Overview on the parameters and properties used to describe a linear cavity.

often convenient to work with the intensity $I(x, y, z)$ of the beam. For a monochromatic propagating wave like a plane wave or Gaussian beam, $I(x, y, z)$ is given by

$$I(x, y, z) = \frac{c_0 \epsilon_0 n}{2} |E|^2 \tag{A.1}$$

where ϵ_0 is the vacuum permeability. We will switch between these two quantities depending on the effects discussed.

Another important quantity used in the description of light fields is the beam power P which can be calculated by integrating the beam intensity I over the beam surface area

$$P = \int_A I(x, y, z) dA \tag{A.2}$$

We assume that we work in the linear regime where we lose intensity linearly during each round trip due to continuous absorption losses. The intensity of the incoming beam then decreases as

$$\frac{dI}{dp} = -\alpha I \Rightarrow I(p) = I_0 \mathrm{e}^{-\alpha p} \tag{A.3}$$

Mirror losses due to absorption and transmission are collected in

$$R = 1 - T - X \tag{A.4}$$

In this section we do not take the spatial x, y, z dependance of the light field into account, we therefore suppress these indices for convenience. The parameters used in the following can be found in table A.1 if not explicitly written. The amplitude of the incoming beam E_{in} will be partially transmitted through the first mirror and become

$$E_0 = \sqrt{T_1} E_{in} \tag{A.5}$$

The beam will circulate back and forth inside the cavity. During each round trip, the amplitude will be reduced by a factor of

$$g_{rt} = \sqrt{R_1 R_2 \mathrm{e}^{-\alpha p}} \tag{A.6}$$

which is called the round trip gain or loss parameter, and the wave picks up a phase shift of

$$\delta\phi = \phi_c - \phi_{in} = 2\pi\tilde{\nu}\frac{p}{c} \tag{A.7}$$

with respect to the incoming beam, where

$$\widetilde{\nu} = \nu - \nu_c \tag{A.8}$$

is the frequency detuning of the beam, relative to a cavity resonance at ν_c. We will write most equations and plots in this work with respect to $\widetilde{\nu}$. The electric field of the wave then changes by

$$E_{j+1} = g_{rt}\mathrm{e}^{-i\delta\phi}E_j = g_{rt}(\widetilde{\nu})E_j \tag{A.9}$$

from one round tip to the next. The cumulative field amplitude circulating in the cavity is then given by the sum over the amplitudes of all circulating waves

$$E_c = \sum_{j=0}^{\infty} E_j \tag{A.10}$$

Inserting (A.9) into (A.10) yields an equation for the overall amplitude of the field inside of the cavity

$$E_c = \sum_{j=0}^{\infty} g_{rt}(\widetilde{\nu})^j E_0 = \frac{E_0}{1 - g_{rt}(\widetilde{\nu})} \tag{A.11}$$

Thus, the power of the field inside the cavity builds up as

$$\begin{aligned} P_c \propto |E_c|^2 &= \frac{|E_0|^2}{|1 - g_{rt}(\widetilde{\nu})|^2} \\ &= \frac{|E_0|^2}{|1 - g_{rt}\mathrm{e}^{-i\delta\phi}|^2} \\ &= \frac{|E_0|^2}{(1 - g_{rt}\cos(\delta\phi))^2 + (g_{rt}\sin(\delta\phi))^2} \\ &= \frac{|E_0|^2}{(1 - g_{rt})^2 + 2g_{rt}(1 - \cos(\delta\phi))} \\ &= \frac{|E_0|^2}{(1 - g_{rt})^2 + 4g_{rt}\sin^2(\pi\widetilde{\nu}\frac{p}{c})} \end{aligned} \tag{A.12}$$

where we have used the trigonometric identity

$$2\sin^2(x/2) = 1 - \cos(x) \tag{A.13}$$

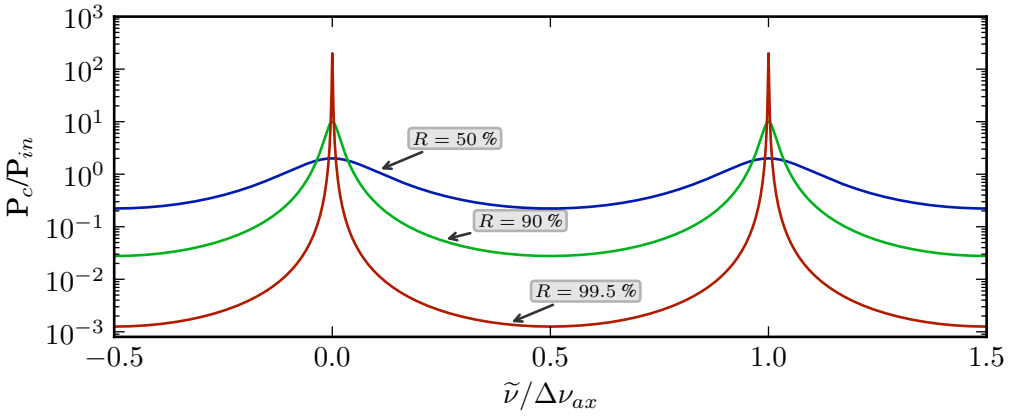

Fig. A.2: The power of the laser field circulating in a cavity with identical mirrors with intensity reflectivities of $R = 50\ \%$, $R = 90\ \%$ and $R = 99.5\ \%$ is shown. The powers shown are with respect to the incoming beam power.

and the multiplicativeness of absolute values

$$|z_1 z_2| = |z_1|\,|z_2| \qquad \Rightarrow \qquad \left|\frac{z_1}{z_2}\right| = \frac{|z_1|}{|z_2|} \tag{A.14}$$

where z_1 and z_2 are arbitrary complex numbers.

A.2 Maximum power and Finesse

We now introduce the maximum power and the Finesse

$$P_{max} = a\left(\frac{E_0}{1-g_{rt}}\right)^2, \qquad F = \frac{\pi\sqrt{g_{rt}}}{(1-g_{rt})} \tag{A.15}$$

where a takes into account all coefficients resulting from (A.1) and (A.2). The power built up in the cavity as a function of the laser field frequency is then given by

$$P_c = P_{max}\frac{1}{1+(2F/\pi)^2\sin^2(\pi\widetilde{\nu}\frac{p}{c})} \tag{A.16}$$

P_c is plotted in figure A.2 for different mirror reflectivities R.

A.3 Transmitted, reflected and cavity light field

We now link the amplitudes of the incoming and outgoing field through boundary conditions, here E_c is the amplitude of the internal field just on

the inside of the incoupling mirror M_1, E_t is the transmitted field behind mirror M_2 and E_r is the reflected field in front of mirror M_1.

$$\begin{aligned} E_t &= \sqrt{T_2}\mathrm{e}^{-\alpha p/2 + i\delta\phi/2} E_c \\ &= \sqrt{\frac{T_1 T_2}{R_1 R_2}} \frac{g_{rt}(\widetilde{\nu})}{1 - g_{rt}(\widetilde{\nu})} E_{in} \end{aligned} \tag{A.17}$$

The transmitted field first travels from mirror M_1 to M_2 and gets attenuated and phase shifted before it couples out of the cavity at mirror M_2 with transmission coefficient $\sqrt{T_2}$.

$$\begin{aligned} E_r &= -\sqrt{R_1} E_{in} + \frac{g_{rt}(\widetilde{\nu})}{\sqrt{R_1}} \sqrt{T_1} E_c \\ &= -\sqrt{R_1} E_{in} + \frac{T_1}{\sqrt{R_1}} \frac{g_{rt}(\widetilde{\nu})}{1 - g_{rt}(\widetilde{\nu})} E_{in} \\ &= \frac{-R_1 + (R_1 + T_1) g_{rt}(\widetilde{\nu})}{\sqrt{R_1}(1 - g_{rt}(\widetilde{\nu}))} E_{in} \\ &= F(\widetilde{\nu}) E_{in} \end{aligned} \tag{A.18}$$

Here we introduced the reflection coefficient $F(\widetilde{\nu})$. The reflected field is a superposition of the incoming beam and the cavity field that left the cavity one round-trip earlier. The incoming beam is reflected at mirror M_1 with reflection coefficient $\sqrt{R_1}$, which also adds a phase shift of π from the reflection on an optical denser medium, hence the minus sign. The cavity field travels one round-trip starting at mirror M_1, excluding the reflection $\sqrt{R_1}$ at M_1, before it is out-coupled through M_1 with $\sqrt{T_1}$.

From equations (A.11), (A.17) and (A.18) it is straight forward to calculate the transmitted and reflected power as well as the power built up in the cavity in relation to the input power. We want to discuss the special case of the loss less linear cavity here, as all cavities used in this work are well described by this model. Therefore, the loss coefficient $\alpha = 0$ and

$R_1 + T_1 = R_2 + T_2 = 1$. We then arrive at

$$\begin{aligned}\frac{P_t}{P_{in}} &= \frac{T_1 T_2}{R_1 R_2} \frac{|g_{rt}(\widetilde{\nu})|^2}{|1 - g_{rt}(\widetilde{\nu})|^2} \\ &= \frac{T_1 T_2}{(1 - g_{rt})^2} \frac{1}{\left(1 + (2F/\pi)^2 \sin^2(\pi \widetilde{\nu} \frac{p}{c})\right)}\end{aligned} \tag{A.19}$$

$$\begin{aligned}\frac{P_r}{P_{in}} &= \frac{1}{R_1} \frac{|R_1 - g_{rt}(\widetilde{\nu})|^2}{|1 - g_{rt}(\widetilde{\nu})|^2} \\ &= \frac{\frac{1}{R_1}\left(\frac{R_1 - g_{rt}}{1 - g_{rt}}\right)^2 + (2F/\pi)^2 \sin^2(\pi \widetilde{\nu} \frac{p}{c})}{1 + (2F/\pi)^2 \sin^2(\pi \widetilde{\nu} \frac{p}{c})}\end{aligned} \tag{A.20}$$

$$\begin{aligned}\frac{P_c}{P_{in}} &= \frac{T_1}{|1 - g_{rt}(\widetilde{\nu})|^2} \\ &= \frac{T_1}{(1 - g_{rt})^2} \frac{1}{\left(1 + (2F/\pi)^2 \sin^2(\pi \widetilde{\nu} \frac{p}{c})\right)}\end{aligned} \tag{A.21}$$

One can also extract the relative phase relations between the transmitted/reflected/cavity field and the input field from the equations (A.11), (A.17) and (A.18). Using the identity $\arg(x) - \arg(y) = \arg(\frac{x}{y})$ yields the following relations for the relative phases

$$\begin{aligned}\delta\phi_t &= \arg(E_{trans}) - \arg(E_{in}) \\ &= \arg\left(\sqrt{T_1 T_2} \frac{\mathrm{e}^{-i\delta\phi}}{1 - g_{rt}(\widetilde{\nu})}\right)\end{aligned} \tag{A.22}$$

$$\begin{aligned}\delta\phi_r &= \arg(E_{refl}) - \arg(E_{in}) \\ &= \arg\left(\frac{-R_1 + g_{rt}(\widetilde{\nu})}{\sqrt{R_1}(1 - g_{rt}(\widetilde{\nu}))}\right)\end{aligned} \tag{A.23}$$

$$\begin{aligned}\delta\phi_c &= \arg(E_{cav}) - \arg(E_{in}) \\ &= \arg\left(\frac{\sqrt{T_1}}{1 - g_{rt}(\widetilde{\nu})}\right)\end{aligned} \tag{A.24}$$

The calculated transmitted, reflected and cavity powers and phase responses of the cavity are shown in figure A.3.

A.4 Axial cavity mode frequencies

In this section we will examine the axial-mode spacing and the resonance linewidth of an optical cavity. From (A.16) we can derive the resonance condition for the light field with respect to the cavity

$$\nu\frac{p}{c} = N \tag{A.25}$$

From (A.25) we see that the cavity resonances show a periodic behavior. The spacing of these equally spaced resonances $\Delta\nu_{ax}$ is commonly referred to as the free spectral range (FSR) and is given by

$$\Delta\nu_{ax} = \frac{c}{p} = \frac{c}{2L} \tag{A.26}$$

With (A.26) we can now rewrite (A.16) as

$$P_c = P_{max}\frac{1}{1 + (2F/\pi)^2 \sin^2(\pi\widetilde{\nu}/\Delta\nu_{ax})} \tag{A.27}$$

The width of a single resonance of the optical cavity is given by the full width at half maximum Γ_c, where $P_c = \frac{1}{2}P_{max}$. Using (A.27) we get

$$1 + (2F/\pi)^2 \sin^2\left(\frac{\pi\Gamma_c/2}{\Delta\nu_{ax}}\right) = 2$$

$$\Gamma_c = \frac{2}{\pi}\sin^{-1}\left(\frac{\pi}{2F}\right)\Delta\nu_{ax} \tag{A.28}$$

In general, the attenuation of the field during one round trip is small, therefore g_{rt} is close to 1 and from (A.15) we see that $F >> 1$. Therefore we can expand $\sin^{-1}\left(\frac{\pi}{2F}\right) \approx \frac{\pi}{2F}$ in (A.28) and arrive at the defining equation for the width of the resonance

$$\Gamma_c \approx \frac{\Delta\nu_{ax}}{F} \tag{A.29}$$

From (A.26) we see that the axial-mode spacing mainly depends on the length of the cavity, while the width of the resonance depends on the axial-mode spacing and the Finesse of the cavity. Therefore the width of the resonance mainly depends on the length of the cavity and the reflectance of the mirrors.

A.5 Cavity ring-down time

An optical cavity stores energy by capturing a light field by multiple reflection. This behavior very much resembles the working principle of an electric capacitor. In analogy to a capacitor, we want to look at the temporal behavior of the cavity field. We assume that we abruptly switch on the laser field at $t = 0$, then we can model the time evolution of the intensity built up in the cavity as

$$\frac{dI_{cav}(t)}{dt} = T_1 I_{in} - I_{cav}(t)\,(T_1 + T_2 + X_1 + X_2 + 2\,\alpha\,L)\,\frac{c}{2L} \tag{A.30}$$

$$= T_1 I_{in} - I_{cav}(t)\,(2 - R_1 - R_2)\,\Delta\nu_{ax} \tag{A.31}$$

where $I_{cav}(t)$ is the intensity inside the cavity, I_{in} is the intensity of the incoming beam and $\Delta\nu_{ax} = \frac{c}{2L}$ is the inverse of the round-trip time, which equals the FSR. This is a simple inhomogeneous first order differential equation which can be solved with an exponential Ansatz $I_h(t) = C_1 \mathrm{e}^{-t/\tau_c}$ for the ordinary part and a constant Ansatz $I_p = C_2$ for the partial part. From (A.31) and the boundary condition $I_{cav}(0) = 0$, i.e. not light in the cavity at $t = 0$, we obtain

$$I_{cav}(t) = (1 - T_1)\,\tau_c\,I_{in}(1 - \mathrm{e}^{-t/\tau_c}) \tag{A.32}$$

with the cavity-ring-down time given by

$$\tau_c = \frac{1}{(2 - R_1 - R_2)\,\Delta\nu_{ax}} = \frac{1}{2\pi\Gamma_c} \tag{A.33}$$

When switching off the laser, the intensity of light in the cavity will decay as

$$\frac{dI_{cav}(t)}{dt} = -I_{cav}(t)\,(2 - R_1 - R_2)\,\Delta\nu_{ax} \tag{A.34}$$

This time, only a homogeneous part is present. With $I_h(t) = C_3 \mathrm{e}^{-t/\tau_c}$ and $I_{cav}(0) = (1 - T_1)\,\tau_c\,I_{in}$, i.e. the cavity light field is saturated, we obtain

$$I_{cav}(t) = (1 - T_1)\,\tau_c\,I_{in}\mathrm{e}^{-t/\tau_c} \tag{A.35}$$

where the cavity-ring-down time is again given by (A.33).

We have seen that the intensity of light inside the cavity follows an exponential build up and decay process, as does the the stored energy, accordingly.

If we send light into the cavity which changes its amplitude quickly, the out-coupled light

$$I_{trans}(t) \propto T_2\, I_{cav}(t) = T_2\,(1 - T_1)\,\tau_c\, I_{in} \mathrm{e}^{-t/\tau_c} \tag{A.36}$$

will only follow these changes if they occur on a larger timescale than τ_c. The cavity therefore behaves like a low pass with a cut-off frequency of

$$\nu_c = \frac{1}{\tau_c} \tag{A.37}$$

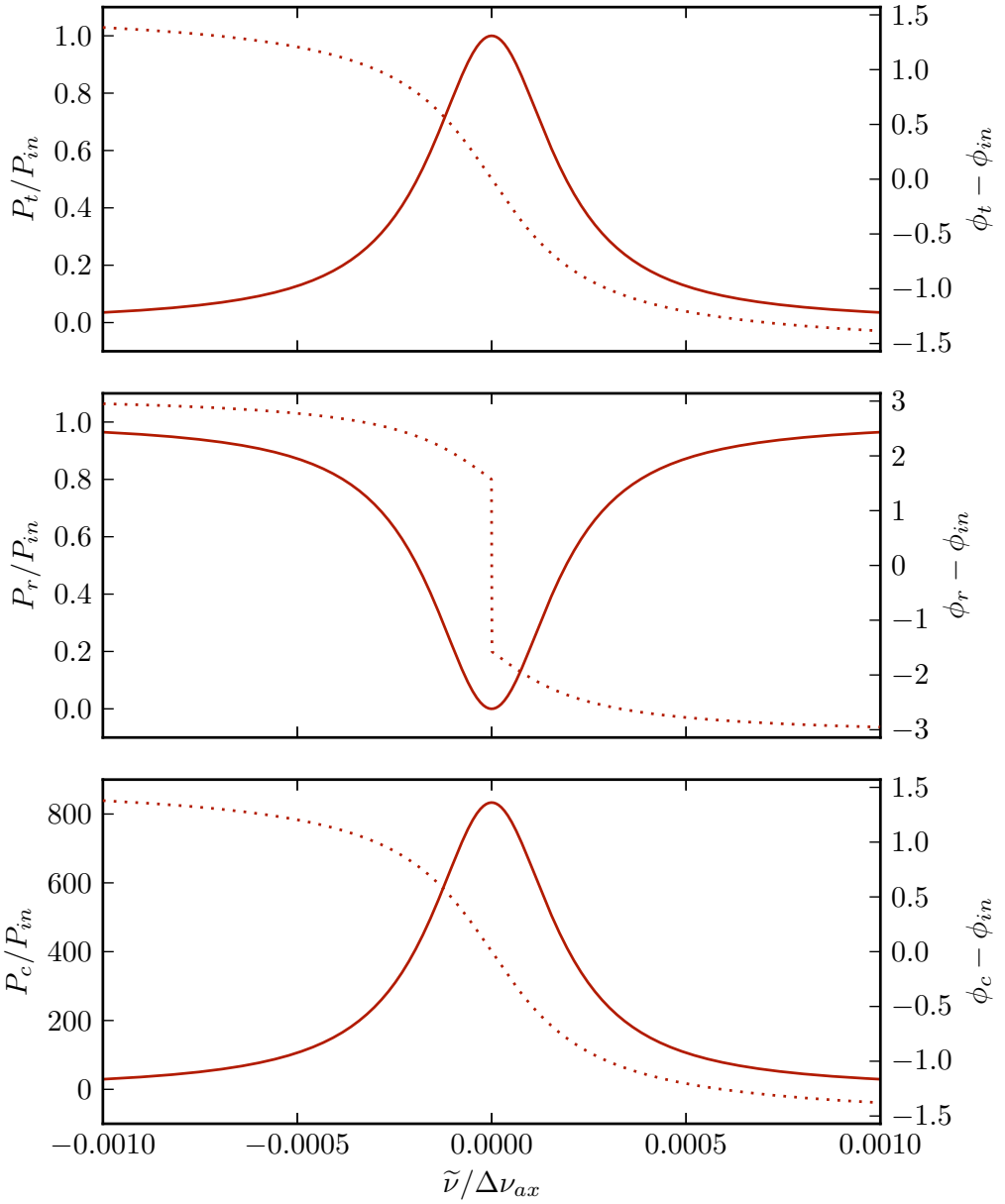

Fig. A.3: The transmitted (top), reflected (middle) and cavity (bottom) powers (solid) and phase responses (dotted) of the cavity are shown. The power inside the cavity shows a large amplifications at resonance. The phase response of the cavity field and the transmitted field change continuously from $-\pi/2$ to $\pi/2$, while the phase response of the reflected signal ranges from $-\pi$ to π and shows a discontinuity of height π at resonance.

Appendix B

WAVE ANALYSIS OF BEAMS AND CAVITIES

The properties of Gaussian beams is not restricted to the application on optical cavities. As with the theory on cavities, this topic is covered well in the literature, see e.g. [11]. Nevertheless it seems useful to review the parts which are of interest here and include some basic derivations and motivations which are of specific interest for the treatment of optical cavities. We try to be consistent in the nomenclature with chapter A.

In this chapter, we want to look at the transverse field properties and modes of cavities and lasers. As the transverse mode properties of the laser field described here emerge from the fact that the active laser medium is trapped in an optical cavity, we will from here on only talk about the transverse modes of cavities, while all results are naturally also true for laser fields. We will follow [11, 9, 10] in the description of the transverse field modes.

The field distribution of the fundamental cavity mode is very well described by a Gaussian beam. Depending on the underlying geometry of the cavity, the transverse field distribution of the higher order modes will show an additional structure. Box-shaped cavities (rectangular mirrors) generate a Hermite - Gaussian, cylindrical cavities (circular mirrors) a Laguerre - Gaussian field distribution.

B.1 Gaussian beams

In many applications one is interested in beams with a Gaussian transverse field distribution or mode. Due to it's importance it is often called the "fundamental mode" [11]. The fundamental mode has the smallest spacial extension of all transverse modes. In this work we always work with the fundamental mode and try to suppress higher transverse modes, yet they are introduced for completeness.

Coherent cavity fields with a field amplitude $E(x, y, z)$ satisfy the scalar wave equation

$$\nabla^2 E(x, y, z) + k^2 E(x, y, z) = 0 \tag{B.1}$$

where the propagation constant in a medium is given by $k = 2\pi/\lambda$. In analogy to a plane wave, one can write

$$E(x, y, z) = \psi(x, y, z)\mathrm{e}^{-ikz} \tag{B.2}$$

where $\psi(x, y, z)$ describes the slowly varying non-uniform field distribution that distinguishes u from a plane wave. Inserting (B.2) into (B.1) yields

$$\frac{\partial^2\psi}{\partial x^2} + \frac{\partial^2\psi}{\partial y^2} - 2ik\frac{\partial\psi}{\partial z} = 0 \tag{B.3}$$

Here we have assumed that ψ varies only slowly in the direction of propagation z and we can therefore neglect the second derivative $\frac{\partial^2\psi}{\partial z^2}$. One solution of (B.3) is

$$\psi(r, z) = \tilde{E}_0 \exp\left[-i\left(P(z) + \frac{k}{2q(z)}r^2\right)\right] \tag{B.4}$$

where $\tilde{E}_0$ is the field amplitude, $P(z)$ represents a complex phase shift associated to the propagation of the beam and $q(z)$ is a complex beam parameter which describes the variation of the intensity and phase with the distance r from the optical axis

$$r^2 = x^2 + y^2 \tag{B.5}$$

Inserting (B.4) into (B.3) one obtains

$$\begin{aligned}
\left(\frac{\partial^2}{\partial x^2} + \frac{\partial^2}{\partial y^2}\right)\mathrm{e}^{-i\left(P(z)+\frac{k}{2q(z)}r^2\right)} - 2ik\frac{\partial}{\partial z}\mathrm{e}^{-i\left(P(z)+\frac{k}{2q(z)}r^2\right)} &= 0 \\
\left(-2i\frac{k}{q} - \frac{k^2}{q^2}r^2\right) - \left(2k\frac{\partial P}{\partial z} - \frac{k^2}{q^2}\frac{\partial q}{\partial z}r^2\right) &= 0 \\
-2k\left(\frac{\partial P}{\partial z} + \frac{i}{q}\right) + \frac{k^2}{q^2}r^2\left(\frac{\partial q}{\partial z} - 1\right) &= 0
\end{aligned} \tag{B.6}$$

By collecting terms of the same power in r we get

$$\frac{\partial P}{\partial z} = -\frac{i}{q} \tag{B.7}$$

and

$$\frac{\partial q}{\partial z} = 1 \tag{B.8}$$

and from integration of (B.8)

$$q_2 = q_1 + z \tag{B.9}$$

which relates the beam parameter of the output plane z_2 to the beam parameter of the input plane z_1, separated by a distance z. To assign a physical meaning to the beam parameter q we introduce two real parameters, the *radius of curvature* of the wavefront $R(z)$ and the *beam radius* or *spot size* $w(z)$, where $2w(z)$ is the beam diameter, see (B.10). $w(z)$ measures the decrease in field amplitude with the distance from the optical axis. The nomenclature and meaning of $R(z)$ and $w(z)$ become clear when we insert (B.10) into (B.4), we then obtain obtain

$$\frac{1}{q} = \frac{1}{R} - i\frac{\lambda}{\pi w^2} \tag{B.10}$$

$$\psi(r,z) = \tilde{E}_0 \exp\left[-i\left(P(z) + \frac{k}{2R}r^2\right) - \frac{r^2}{w^2}\right] \tag{B.11}$$

We see that $R(z)$ and $w(z)$ depend on the position along the optical axis. At one point, the spatial extent of the Gaussian beam will be minimal with $w(z) = w_0$ and the phase front will be plane $\frac{1}{R} \to 0$. w_0 is called the *beam waist* of the Gaussian beam. It is convenient to measure distances z from this point, and the beam parameter at $z = 0$ becomes purely imaginary

$$q_0 = i\frac{\pi w_0^2}{\lambda} \tag{B.12}$$

If we insert (B.12) into (B.9) we obtain the beam parameter at position z

$$q(z) = q_0 + z = i\frac{\pi w_0^2}{\lambda} + z \tag{B.13}$$

By inserting (B.13) into (B.10) and equating the real and imaginary parts

$$\left(\frac{z}{R} + \frac{w_0^2}{w^2} - 1\right) + i\left(\frac{\pi w_0^2}{R\lambda} - \frac{\lambda z}{\pi w^2}\right) = 0 \tag{B.14}$$

we obtain expressions for $R(z)$ and $w(z)$

$$w(z) = w_0\sqrt{1+\left(\frac{\lambda z}{\pi w_0^2}\right)^2} = w_0\sqrt{1+\left(\frac{z}{z_0}\right)^2} \tag{B.15}$$

$$R(z) = z\left[1+\left(\frac{\pi w_0^2}{\lambda z}\right)^2\right] = z\left[1+\left(\frac{z_0}{z}\right)^2\right] \tag{B.16}$$

where we have introduced the *Rayleigh length*

$$z_0 = \frac{\pi w_0^2}{\lambda} \tag{B.17}$$

The expansion of a Gaussian beam shows an asymptotic behavior far away from the beam waist. The Rayleigh length is often thought of as the limit between the non-linear Gaussian expansion and the linear expansion in the asymptotic limit. For $z >> z_0$, $w(z)$ becomes

$$w(z) = w_0\sqrt{1+\left(\frac{z}{z_0}\right)^2} \approx \frac{w_0 z}{z_0} = \frac{\lambda z}{\pi w_0} \tag{B.18}$$

and the far field divergence angle can be defined as

$$\theta = \tan^{-1}\left(\frac{w(z)}{z}\right) \approx \frac{\lambda}{\pi w_0} \tag{B.19}$$

To get a full theoretical description of a Gaussian beam we need to calculate the complex phase shift $P(z)$. We therefore insert (B.13) into (B.7) and integrate the result to obtain

$$\frac{\partial P}{\partial z} = -\frac{i}{q} = -\frac{i}{i\pi w_0^2/\lambda + z} \tag{B.20}$$

$$\begin{aligned} iP(z) &= \ln\left[1 - i\left(\frac{\lambda z}{\pi w_0^2}\right)\right] \\ &= \ln\sqrt{1+\left(\frac{\lambda z}{\pi w_0^2}\right)^2} - i\tan^{-1}\left(\frac{\lambda z}{\pi w_0^2}\right) \\ &= \ln\left(\frac{w(z)}{w_0}\right) - i\tan^{-1}\left(\frac{z}{z_0}\right) \end{aligned} \tag{B.21}$$

The real part of $P(z)$ corresponds to a phase shift

$$\Phi(z) = \tan^{-1}\left(\frac{\lambda z}{\pi w_0^2}\right) \tag{B.22}$$

between the Gaussian wave and a plane wave, the imaginary part resembles the damping of the intensity of the beam on the optical axis due to an expansion of the beam. We obtain the full theoretical description of a Gaussian beam in accordance to (B.2), where $E(x, y, z) = E(r, z)$ satisfies the wave equation (B.1).

$$\begin{aligned} E(r,z) &= \psi(r,z)\mathrm{e}^{-ikz} \\ &= \tilde{E}_0 \exp\left[-i\left(P(z) + \frac{k}{2q(z)}r^2 + kz\right)\right] \\ &= \tilde{E}_0 \frac{w_0}{w(z)} \exp\left[-i\left(kz - \Phi(z)\right) - r^2\left(\frac{1}{w(z)^2} + \frac{ik}{2R(z)}\right)\right] \end{aligned} \tag{B.23}$$

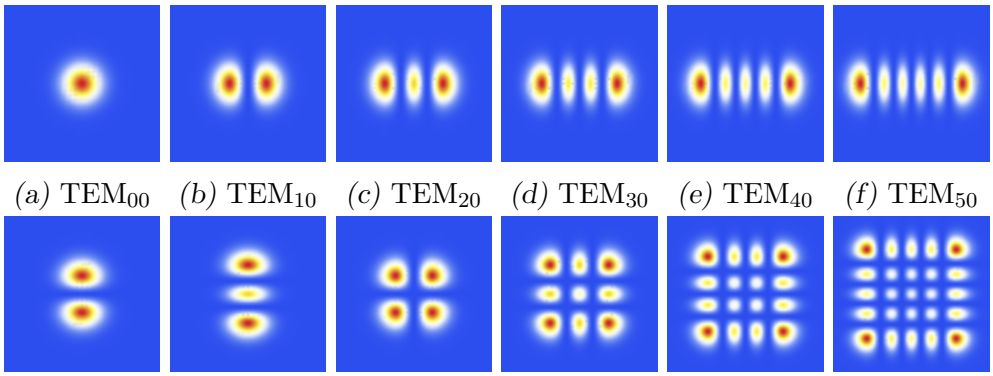

(a) TEM_{00} (b) TEM_{10} (c) TEM_{20} (d) TEM_{30} (e) TEM_{40} (f) TEM_{50}

(g) TEM_{01} (h) TEM_{02} (i) TEM_{11} (j) TEM_{22} (k) TEM_{33} (l) TEM_{44}

Fig. B.1: Transverse electric field modes (TEM_{nm}) for a rectangular cavity geometry. TEM_{00} is the fundamental mode.

B.2 Hermite - Gaussian beams

Box-shaped cavities with rectangular mirrors are best described in a Cartesian coordinate system. The transverse mode profile can be described by a combination of Hermite polynomials and a Gaussian beam [11].

$$E(r,z) = H_m\left(\sqrt{2}\frac{x}{w}\right) H_n\left(\sqrt{2}\frac{y}{w}\right) \mathrm{e}^{-\frac{r^2}{w^2}} \times \tilde{E}_0 \frac{w_0}{w(z)} \exp\left[-i\left(kz - \Phi(z)\right) - r^2\frac{ik}{2R(z)}\right] \tag{B.24}$$

The different modes are indexed by the mode numbers m and n, corresponding to the m-th and n-th Hermite polynomial. A sample of the lowest order Laguerre - Gaussian transverse field modes is shown in figure B.1. The radius of curvature of the phase front $R(z)$ is the same for all modes, but the phase shift Φ depends on the mode number [11].

$$\Phi(m,n;z) = (m+n+1)\tan^{-1}\left(\frac{\lambda z}{\pi w_0^2}\right) \tag{B.25}$$

The resonance condition of an optical cavity is phase sensitive, therefore (B.25) leads to different resonance frequencies for the different transverse field modes.

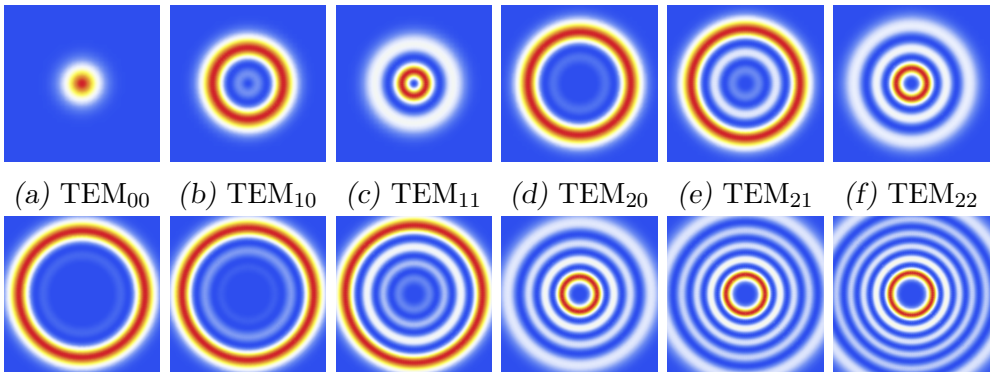

(a) TEM_{00} *(b)* TEM_{10} *(c)* TEM_{11} *(d)* TEM_{20} *(e)* TEM_{21} *(f)* TEM_{22}

(g) TEM_{30} *(h)* TEM_{31} *(i)* TEM_{32} *(j)* TEM_{33} *(k)* TEM_{44} *(l)* TEM_{55}

Fig. B.2: Transverse electric field modes ($\mathrm{TEM}_{\mathrm{nm}}$) for a cylindrical cavity geometry. TEM_{00} is the fundamental mode.

B.3 Laguerre - Gaussian beams

Cylindrical cavities with circular mirrors are best described in a cylindrical coordinate system. The conceptual treatment is quite similar to box-shaped cavities. The transverse mode profile can be described by a combination of Laguerre polynomials and a Gaussian beam [11].

$$E(r,z) = \left(\sqrt{2}\frac{r}{w}\right)^{l} L_p^l\left(2\frac{r^2}{w^2}\right) \mathrm{e}^{-\frac{r^2}{w^2}} \times \tilde{E}_0 \frac{w_0}{w(z)} \exp\left[-i\left(kz - \Phi(z)\right) - r^2\frac{ik}{2R(z)}\right] \tag{B.26}$$

The different modes are indexed by the mode numbers p and l, corresponding to the L_p^l-th Laguerre polynomial. A sample of the lowest order Laguerre - Gaussian transverse field modes is shown in figure B.2. Again, the radius of curvature of the phase front $R(z)$ is the same for all modes, but the phase shift Φ depends on the mode number [11].

$$\Phi(p,l;z) = (2p + l + 1)\tan^{-1}\left(\frac{\lambda z}{\pi w_0^2}\right) \tag{B.27}$$

As stated before, the resonance condition of an optical cavity is phase sensitive, and (B.27) therefore also leads to different resonance frequencies for the different transverse field modes.

Appendix C

POUND-DREVER-HALL LASER LOCK

The PDH lock [8] is very important for the evaluation of the laser linewidth in this work. We therefore want to take a closer look at the theory behind the PDH lock. We try to be consistent with our notation with appendices A and B. This chapter will follow the introduction to the PDH frequency stabilization given in [30]. In analogy to section A we do not explicitly write the spatial dependance of $E(x, y, z)$ while we also neglect the spatial distribution introduced in section B for convenience.

The basic idea: We tune a laser close to a resonance of an optical cavity and send the laser beam through the cavity. The power of the transmitted beam is given by (A.19) and is measured by a photo diode. In the region of a cavity resonance we can expand the transmission signal to

$$\begin{aligned}\frac{P_t}{P_{in}} &= \frac{T_1 T_2}{(1-g_{rt})^2}\,\frac{1}{1+(2F/\pi)^2\sin^2(\pi\widetilde{\nu}\frac{p}{c})} \\ &\approx \frac{T_1 T_2}{(1-g_{rt})^2}\,\frac{1}{1+\left(2\frac{\nu_{ax}}{\pi\Gamma_c}\right)^2\left(\frac{\pi\widetilde{\nu}}{\nu_{ax}}\right)^2} \\ &= \frac{T_1 T_2}{(1-g_{rt})^2}\,\frac{1}{1+\left(\frac{\widetilde{\nu}}{\Gamma_c/2}\right)^2}\end{aligned} \tag{C.1}$$

From (C.1) we see that the cavity transmission signal has a Lorentzian profile, the transmission signal close to a cavity resonance is shown in figure C.1.

We could now try to generate an error signal from the transmission signal, but we run into trouble as the transmission signal is *symmetric* with respect to the resonance. We therefore do not know if we need to increase or decrease the laser frequency if the laser is off-resonant to tune the laser back on to the resonance. One solution used in the past was to slightly detune the laser frequency from the cavity resonance which yields an *asymmetric* signal that

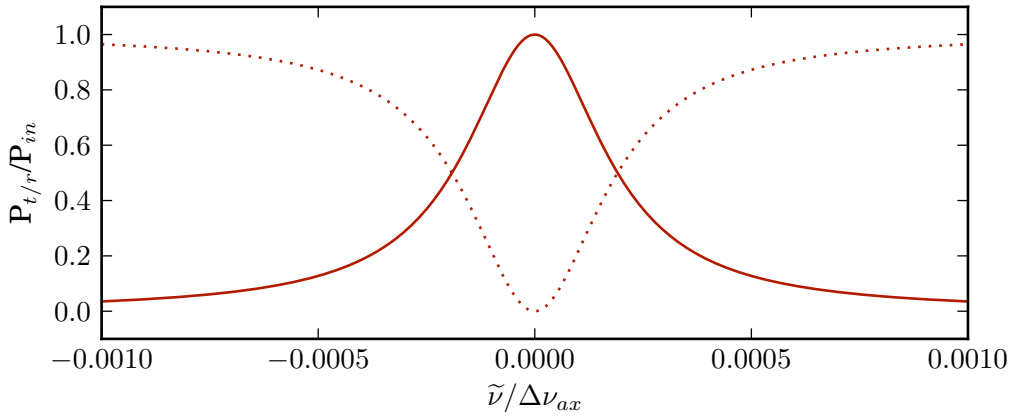

Fig. C.1: The laser power transmitted through the cavity (solid line) and the power reflected from the cavity (dotted line) are shown. Both powers shown are with respect to the incoming beam power. The mirror reflectivity is $R = 99.88$ % which corresponds to the mirrors used in all three generations of transfer cavities.

distinguishes between frequencies above and below the cavity resonance [30]. The downside of this approach comes from the fact that we are now sensitive to intensity fluctuations, the system can not distinguish between intensity deviations resulting from a frequency detuning of the laser with respect to the cavity and intensity fluctuations of the laser.

To decouple frequency and intensity fluctuations we could detect the reflected beam from the cavity with a photo diode and try to keep the reflected power (A.20) close to zero, see figure C.1. The downside of this approach is that the measured signal is still *symmetric* with respect to the resonance. However, the derivative of the reflected power signal is *antisymmetric*, see figure C.2.

To access the derivative of the reflected power signal, we vary the laser or carrier frequency ν of the incoming beam

$$E_{in} = \tilde{E}_0 \mathrm{e}^{i2\pi\nu t} \tag{C.2}$$

by a small amount. This is done by modulating the phase of the carrier with an electro-optic modulator (EOM)

$$E_{in} = \tilde{E}_0 \mathrm{e}^{i[2\pi\nu t + \beta \sin(2\pi\nu' t)]} \tag{C.3}$$

where ν' is the EOM frequency and β is the EOM modulation depth. We

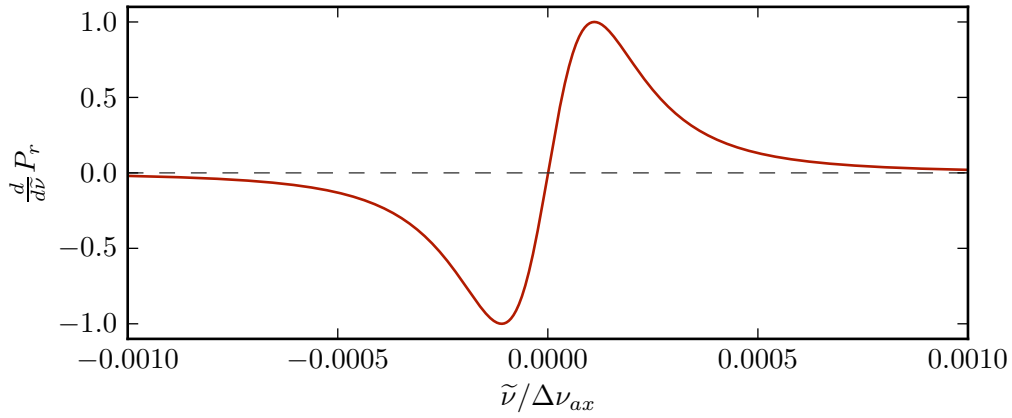

Fig. C.2: The derivative of the power reflected from the cavity is shown, the amplitude was normalized to the maximum amplitude. The mirror reflectivity is $R = 99.88$ % which corresponds to the mirrors used in all three generations of transfer cavities.

can expand (C.3) using the Bessel functions to

$$\begin{aligned} E_{in} &\approx \tilde{E}_0 \left[J_0(\beta) + 2iJ_1(\beta)\sin(2\pi\nu' t)\right] \mathrm{e}^{i2\pi\nu t} \\ &= \tilde{E}_0 \left[J_0(\beta)\mathrm{e}^{i2\pi\nu t} + J_1(\beta)\mathrm{e}^{i2\pi(\nu+\nu')t} - J_1(\beta)\mathrm{e}^{i2\pi(\nu-\nu')t}\right] \end{aligned} \tag{C.4}$$

From (C.4) we see that in addition to the carrier with frequency ν and power $P_{ca} = J_0^2(\beta)P_0$ the EOM generates two sidebands at $\nu \pm \nu'$ with a power of $P_{sb} = J_1^2(\beta)P_0$ each. Here we assumed a sufficiently low modulation depth β so that $J_n(\beta) \approx 0$ for $n \geq 2$, where n corresponds to the n-th order sideband. In this case we can neglect higher order sidebands which is true for our system. In addition we do not have to take these higher order sidebands into account for our derivation of the PDH error signal as they will be filtered out by a low pass.

With (C.4) and (A.18) we can calculate the reflected complex beam amplitude E_r by multiplying each of the three beams created by the EOM (see (C.4)) with the appropriate reflection coefficient $F(\widetilde{\nu})$

$$\begin{aligned} E_{refl} =& \tilde{E}_0[F(\nu)J_0(\beta)\mathrm{e}^{i2\pi\nu t} + F(\nu+\nu')J_1(\beta)\mathrm{e}^{i2\pi(\nu+\nu')t} \\ &- F(\nu-\nu')J_1(\beta)\mathrm{e}^{i2\pi(\nu-\nu')t}] \end{aligned} \tag{C.5}$$

From (C.5) and some algebra we can calculate the reflected beam power

$P_r \propto |E_r|^2$, we get

$$\begin{aligned} P_r =& P_{ca} |F(\nu)|^2 + P_{sb} |F(\nu+\nu')|^2 + P_{sb} |F(\nu-\nu')|^2 \\ &+ 2\sqrt{P_{ca}P_{sb}}\mathrm{Re}\left\{F(\nu)F^*(\nu+\nu') - F^*(\nu)F(\nu-\nu')\right\}\cos(2\pi\nu' t) \\ &+ 2\sqrt{P_{ca}P_{sb}}\mathrm{Im}\left\{F(\nu)F^*(\nu+\nu') - F^*(\nu)F(\nu-\nu')\right\}\sin(2\pi\nu' t) \\ &+ \mathcal{O}(2\nu') \end{aligned} \tag{C.6}$$

We are interested in the terms oscillating with ν' because these terms are phase dependent. The phase is contained in $F(\nu)$. These terms can be extracted using a mixer and mixing the reflected power signal with the original EOM signal. By introducing a time delay to the EOM signal input of the mixer we have control over the phase of the EOM signal with respect to the measured reflected power signal phase. The mixed forms the product of the two signals. To interpret the results, we need the following relations

$$\sin(2\pi\nu t)\sin(2\pi\nu' t) = \frac{1}{2}\left\{\cos\left[2\pi(\nu-\nu')t\right] - \cos\left[2\pi(\nu+\nu')t\right]\right\} \tag{C.7}$$

$$\cos(2\pi\nu t)\sin(2\pi\nu' t) = \frac{1}{2}\left\{\sin\left[2\pi(\nu+\nu')t\right] - \sin\left[2\pi(\nu-\nu')t\right]\right\} \tag{C.8}$$

$$\sin(2\pi\nu t)\cos(2\pi\nu' t) = \frac{1}{2}\left\{\sin\left[2\pi(\nu+\nu')t\right] + \sin\left[2\pi(\nu-\nu')t\right]\right\} \tag{C.9}$$

$$\cos(2\pi\nu t)\cos(2\pi\nu' t) = \frac{1}{2}\left\{\cos\left[2\pi(\nu-\nu')t\right] + \cos\left[2\pi(\nu+\nu')t\right]\right\} \tag{C.10}$$

We can adjust the relative phase between ν and ν', where ν is the frequency of the reflected beam power signal and ν' is the EOM frequency, so that we only have terms proportional to $\sin(2\pi\nu' t)$, namely (C.7) and (C.8). Then we can neglect terms proportional to $\cos(2\pi\nu' t)$, namely (C.9) and (C.10). The mixer therefore multiplies (C.6) by $\sin(2\pi\nu' t)$ and the mixer output is proportional to

$$P_r^{mixer} = \sqrt{P_{ca}P_{sb}}\,\mathrm{Im}\left\{F(\nu)F^*(\nu+\nu') - F^*(\nu)F(\nu-\nu')\right\} + \mathcal{O}(\nu') \tag{C.11}$$

We can also adjust the phase shift between ν and ν' so that we only have terms proportional to $\cos(2\pi\nu' t)$, namely (C.9) and (C.10). The mixer then multiplies (C.6) by $\cos(2\pi\nu' t)$ and the mixer output is proportional to

$$P_r^{mixer} = \sqrt{P_{ca}P_{sb}}\,\mathrm{Re}\left\{F(\nu)F^*(\nu+\nu') - F^*(\nu)F(\nu-\nu')\right\} + \mathcal{O}(\nu') \tag{C.12}$$

For high modulation frequencies ν' compared to the cavity resonance width the imaginary part in (C.6) will be much bigger than the real part, which will be close to zero, while for low modulation frequencies the opposite is true [30]. All modulation frequencies used in this work are high compared to the cavity resonance width and we will work only with the imaginary part. (C.11) contains a DC term and terms oscillating at ν' or higher. The phase information is contained in this DC term, we therefore low pass filter the mixer output and we receive the PDH error signal

$$V_e^{\mathrm{Im}} \propto \sqrt{P_{ca}P_{sb}}\mathrm{Im}\left\{F(\nu)F^*(\nu+\nu') - F^*(\nu)F(\nu-\nu')\right\} \tag{C.13}$$

where V_e is the voltage signal from the mixer output. The error signal is shown in figure C.3.

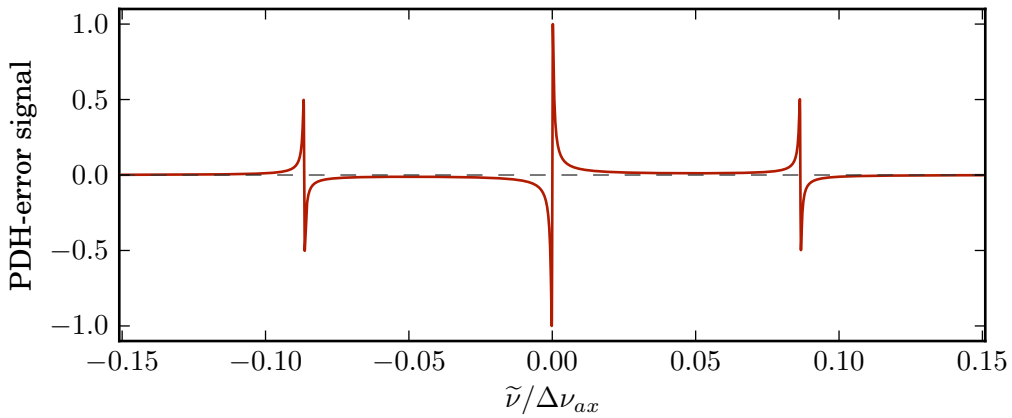

(a) The PDH error signal with the carrier and the sidebands at $\nu' = \pm 89.60$ MHz is shown.

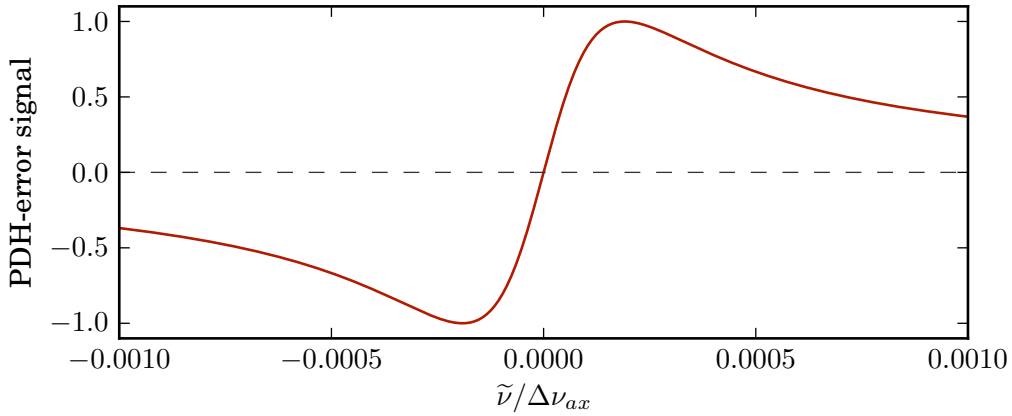

(b) This edge of the PDH error signal at the cavity resonance was used for the laser frequency feedback regulation.

Fig. C.3: The calculated error signal generated by the PDH lock is shown, the amplitude was normalized to the maximum amplitude. The mirror reflectivity is $R = 99.88$ % which corresponds to the mirrors used in all three generations of transfer cavities.

BIBLIOGRAPHY

[1] M. H. Anderson, J. R. Ensher, M. R. Matthews, C. E. Wieman, and E. A. Cornell. Observation of Bose-Einstein Condensation in a Dilute Atomic Vapor. *Science*, 269(5221):198–201, 1995.

[2] K. B. Davis, M.-O. Mewes, M. R. Andrews, N. J. van Druten, D. S. Durfee, D. M. Kurn, and W. Ketterle. Bose-Einstein Condensation in a Gas of Sodium Atoms. *Phys. Rev. Lett.*, 75(22):3969–3973, November 1995.

[3] Helmut Ritsch, Peter Domokos, Ferdinand Brennecke, and Tilman Esslinger. Cold atoms in cavity-generated dynamical optical potentials. *Reviews of Modern Physics*, 85(2):553–601, 2013.

[4] Kristian Baumann, Christine Guerlin, Ferdinand Brennecke, and Tilman Esslinger. Dicke quantum phase transition with a superfluid gas in an optical cavity. *Nature*, 464(7293):1301–6, April 2010.

[5] R. Mottl, F. Brennecke, K. Baumann, R. Landig, T. Donner, and T. Esslinger. Roton-type mode softening in a quantum gas with cavity-mediated long-range interactions. *Science*, 336(6088):1570–3, June 2012.

[6] K. Hepp and E. H. Lieb. On the superradiant phase transition for molecules in a quantized radiation field: the Dicke maser model. *Annals of Physics*, 76(2):360–404, 1973.

[7] Y. K. Wang and F. T. Hioe. Phase transition in the Dicke model of superradiance. *Phys. Rev. A*, 7(3):831–836, 1973.

[8] R. W. P. Drever, J. L. Hall, F. V. Kowalski, J. Hough, G. M. Ford, a. J. Munley, and H. Ward. Laser phase and frequency stabilization using an optical resonator. *Applied Physics B Photophysics and Laser Chemistry*, 31(2):97–105, June 1983.

[9] Anthony E. Siegman. *Lasers*. University Sciencs Books, 1986.

[10] Hans-A. Bachor and Timothy C. Ralph. *A Guide to Experiments in Quantum Optics*. Wiley-VCH Verlag GmbH, second edition, 2004.

[11] H. Kogelnik and T. Li. Laser beams and resonators. *Applied optics*, 5(10):1550–1567, 1966.

[12] J. J. Olivero and R. L. Longbothum. Empirical fits to the Voigt line width: A brief review. *Journal of Quantitative Spectroscopy and Radiative Transfer*, 17(2):233–236, 1977.

[13] Toptica. Tunable Diode Lasers, DLpro 780 datasheet, 2012.

[14] C. Pradere and C. Sauder. Transverse and longitudinal coefficient of thermal expansion of carbon fibers at high temperatures (300–2500K). *Carbon*, 46(14):1874–1884, November 2008.

[15] Carbon Team Germany GmbH. Technische Daten Carbon-Rohr PrePreg, 2010.

[16] MasterBond. Master Bond Polymer System EP21TCHT-1 datasheet, 2002.

[17] A. L. Schawlow and C. H. Townes. Infrared and optical masers. *Physical Review*, 112(6):1940–1949, 1958.

[18] M. Lax. Classical Noise. V. Noise in Self-Sustained Oscillators. *Physical Review*, 160(2), 1967.

[19] HighFinesse Laser and Electronic Systems. HighFinesse WS-7 wavemeter datasheet, 2013.

[20] Gianni Di Domenico, Stéphane Schilt, and Pierre Thomann. Simple approach to the relation between laser frequency noise and laser line shape. *Applied optics*, 49(25):4801–7, September 2010.

[21] A. Schoof, J. Grünert, S. Ritter, and A. Hemmerich. Reducing the linewidth of a diode laser below 30 Hz by stabilization to a reference cavity with a finesse above 10ˆ5. *Optics letters*, 26(20):1562–4, October 2001.

[22] C. Audoin. Metrology and Fundamental Constants. In *International School of Physics "Enrico Fermi" Varenna, Course LXVIII*, pages 169–220, North–Holland, Amsterdam, 1980.

[23] Innovative Sensor Technology. Platinum -Temperature Sensors, PT1000 datasheet, 2013.

[24] Burr-Brown. Precision, Low Power Instrumentation Amplifier INA118 datasheet, 1998.

[25] Pico LTd. Technology. PicoScope 4226 and 4227, High–Resolution Oscilloscopes with Arbitrary Waveform Generator datasheet, 2010.

[26] Richard W. Fox, Chris W. Oates, and Leo W. Hollberg. *Experimental Methods in the Physical Sciences*, volume 40. Elsevier Science, 2003.

[27] A. A. Clerk, M. H. Devoret, S. M. Girvin, Florian Marquardt, and R. J. Schoelkopf. Introduction to quantum noise, measurement, and amplification. *Reviews of Modern Physics*, 82(2):1155–1208, April 2010.

[28] D. S. Elliott, Rajarshi Roy, and S. J. Smith. Extracavity laser bandshape. *Physical Review A*, 26(1):12–18, 1982.

[29] T. Okoshi, K. Kikuchi, and A. Nakayama. Novel method for high resolution measurement of laser output spectrum. *Electronics Letters*, 16(16):630–631, 1980.

[30] Eric D. Black. An introduction to Pound–Drever–Hall laser frequency stabilization. *American Journal of Physics*, 69(1):79, 2001.